

CHATTER STABILITY OF TURNING AND MILLING WITH PROCESS DAMPING

by

MAHDI EYNIAN

B.A. Sc. Sharif University of Technology, 2001

M.A. Sc., Sharif University of Technology, 2003

A THESIS SUBMITTED IN PARTIAL FULFILLMENT OF
THE REQUIREMENTS FOR THE DEGREE OF

DOCTOR OF PHILOSOPHY

in

THE FACULTY OF GRADUATE STUDIES

(Mechanical Engineering)

THE UNIVERSITY OF BRITISH COLUMBIA

(Vancouver)

January 2010

© Mahdi Eynian, 2010

Abstract

The prediction of chatter instability in machining steel and thermal-resistant alloys at low cutting speeds has been difficult due to unknown process damping contributed by the contact mechanism between tool flank and wavy surface finish. This thesis presents modeling and measurement of process damping coefficients, and the prediction of chatter stability limits for turning and milling operations at low cutting speeds.

The dynamic cutting forces are separated into regenerative and process damping components. The process damping force is expressed as a product of dynamic cutting force coefficient and the ratio of vibration and cutting velocities. It is demonstrated that the dynamic cutting coefficient itself is strongly affected by flank wear land. In measurement of dynamic cutting forces, the regenerative force is eliminated by keeping the inner and outer waves parallel to each other while the tool is oscillated using a piezo actuator during cutting.

Classical chatter stability laws cannot be used in stability prediction for general turning with tools cutting along non-straight cutting edges; where the direction and magnitude of the dynamic forces become dependent on the depth of cut and feed-rate. A new dynamic cutting force model of regeneration of chip area and process damping, which considers tool nose radius, feed-rate, depth of cut, cutting speed and flank wear is presented. The chatter stability is predicted in the frequency domain using Nyquist stability criterion.

The process damping is considered in a new dynamic milling model for tools having rotating but asymmetric dynamics. The flexibility of the workpiece is studied in a fixed coordinate system but the flexibility of the tool is studied in a rotating coordinate system.

The periodic directional coefficients are averaged, and the stability of the dynamic milling system is determined in the frequency domain using Nyquist stability criterion.

The experimentally proven, proposed stability models are able to predict the critical depth of cut at both low and high cutting speeds.

Table of Contents

Abstract.....	ii
Table of Contents.....	iv
List of Tables.....	vii
List of Figures.....	viii
List of Symbols.....	xiii
Acknowledgment.....	xvi
Chapter 1: Introduction.....	1
Chapter 2: Literature Survey.....	4
2.1 Overview.....	4
2.2 Dynamics of Metal Cutting Process.....	4
2.3 Process Damping.....	8
2.4 Stability of Three Dimensional Turning.....	11
2.5 Stability of Milling Operations.....	13
Chapter 3: Orthogonal Cutting with Process Damping.....	15
3.1 Overview.....	15
3.2 Modeling of Process Damping Forces.....	15
3.3 Identification of Process Damping Forces with Oscillation Cutting Tests.....	21
3.4 Tool Wear and Process Damping Mechanism.....	25
3.5 Chatter Stability Diagrams.....	27
3.6 Conclusion.....	28
Chapter 4: Stability of General Turning with Process Damping.....	29

4.1	Introduction.....	29
4.2	Cutting Force Nonlinearity	29
4.2.1	Cutting force prediction based on chip flow direction.....	30
4.2.2	Cutting force prediction based on variable approach angle.....	34
4.3	Time Domain Simulation of Turning Process	36
4.3.1	State vector.....	41
4.3.2	Results of the time domain simulation.....	42
4.4	Analytical Model I: Regenerative Chip Model.....	43
4.5	Analytical Model II: Regenerative Chip Area and Chord Model.....	47
4.5.1	Modeling of dynamic cutting force gains in turning	48
4.5.2	Process damping gains contributed by flank wear.....	54
4.6	Simulations and Experimental Results	57
4.6.1	Sensitivity analysis of stability models.....	58
4.6.2	Chatter tests with varying nose radius and feed rates.....	61
4.6.3	Chatter tests with varying spindle speed.....	63
4.7	Conclusion	66
Chapter 5: Stability of Milling at Process Damping Speeds.....		68
5.1	Introduction.....	68
5.2	Dynamic Cutting Force Model	70
5.3	Structural Dynamic Model.....	78
5.4	Stability of the System	79
5.5	Simulation and Experimental Results.....	81
5.6	Conclusion	88

Chapter 6: Conclusion and the Future Works.....	90
6.1 Conclusions.....	90
6.1.1 Process damping mechanism	90
6.1.2 Stability of three dimensional turning.....	91
6.1.3 Stability of milling with rotating cutter dynamics at process damping speeds	91
6.2 Future Works	92
Bibliography	94
Appendix A: Nyquist Stability Criterion.....	100
A.1 Application of Nyquist Stability Criterion in Chatter Problems.....	100
A.2 Numerical Evaluation of Stability	102
Appendix B: Extraction of Dynamic Cutting Coefficients from Sampled Signals..	104
B.1 Discrete Time Fourier Transform (DTFT)	104
B.2 Extraction of Signal Components at the Main Oscillation Frequency	106
B.3 Example	107
Appendix C: Averaging Dynamic Matrices in Milling.....	109
C.1 Summation of Average Matrices	114
C.1.1 Summation lemma	114
C.1.2 Average matrix for cutters having more than two teeth	116
C.1.3 Average matrix for a tool with two teeth (N=2)	118
C.1.4 Average matrix for a single tooth tool (N=1)	119
C.2 Comparison with Classical Stability Prediction Method.....	121

List of Tables

Table 3-1: process damping coefficient determined with different theories	21
Table 4-1: Differentials of chord angle, length and area with respect to displacements in depth of cut and feed directions.....	54
Table 4-2: Modal Parameters of chatter test setup.....	64
Table 4-3: Cutting coefficients for AISI 1045 steel at different speeds; same tool is used as given in Figure 6.....	66
Table 5-1: Parameters used in slot millin11g of AISI 1045 steel with R390-020A20L-11L tool holder having 2 R390-11 T302E-PM-4240 inserts.	84
Table B-1: Cutting conditions and dynamic cutting coefficients in the sample dynamic cutting test.....	108

List of Figures

Figure 2-1: Cutting forces during chatter.....	5
Figure 2-2: Photomicrograph of workpiece surface: (a) stable cutting, (b) chatter, (c) vibration marks as seen by naked eyes	5
Figure 2-3: Chatter in orthogonal cutting with block diagram	6
Figure 2-4: Inner and outer waves on chips (a), (b) regular camera, (c) under a microscope	7
Figure 2-5: Process-damping mechanism as suggested by Wallace and Andrew [48]	10
Figure 2-6: Photomicrograph of rake face of a turning tool; chip area has a lighter color due to the wear on rake face	11
Figure 2-7: Three-dimensional flexibility in a turning operation	12
Figure 3-1: Regenerative orthogonal cutting process with the effect of vibration velocity	16
Figure 3-2: Work material compression under the cutting edge radius as a source of process damping force as described by Sisson and Kegg [38]	18
Figure 3-3: Photomicrograph of tool wear land.....	18
Figure 3-4: Work material compression under the tool flank, as proposed by Wallace et al [48].....	20
Figure 3-5: Dynamic cutting force test rig.....	22
Figure 3-6: Schematic of oscillation cutting tests.....	23
Figure 3-7: Sample measurements during dynamic plunge turning test. Work material: Stainless Steel SS304, Tool: Sandvik Coromant N123 H13A with 0 degree rake and 7	

degree clearance angle. The width of cut: 0.5 mm, feed: 0.050 mm/rev. spindle speed: 2174 rev/min, tool oscillation frequency: 72.59 Hz (DC components are removed). 23

Figure 3-8: Process gain versus inverse wavelength with zero phase shift between inner and outer oscillations. Material: AISI1045, Cutting force coefficients: $K_z = 2580\text{MPa}$, $K_y = 1384\text{MPa}$, $C_y = 6.9 \times 10^6 / (2\pi) = 1.1 \times 10^6\text{N/m}$ and $C_z = 6.2 \times 10^6 / (2\pi) = 9.9 \times 10^5\text{N/m}$ 25

Figure 3-9: The effect of tool wear on the stability lobes with experimental results. Material: Stainless steel SS304 shaft with 35 mm diameter. Feed rate: 0.050mm/rev. Structural parameters: $m = 1.742\text{Kg}$, $C = 176.8\text{N/m/s}$, $K = 7.92\text{MN/m}$. Cutting force Coefficients: $K_z = 2068\text{MPa}$, $K_y = 2585\text{MPa}$ New tool : $C_y = 1.2\text{MN/m}$ Worn tool with 0.080 mm flank wear $C_y = 4.9\text{MN/m}$ 26

Figure 3-10: The relationship between the process damping coefficient and square of wear length..... 27

Figure 3-11: Stability lobes with and without process damping terms. Measured cutting forces during stable ($n=500\text{ rev/min}$, $a=1\text{ mm}$) and unstable ($n=1500\text{ rev/min}$, $a=1\text{mm}$) cutting tests. Material: AISI1045 with a diameter of 35 mm. $\omega_n = 450.7\text{Hz}$ $K = 6.48 \times 10^6\text{N/m}$, $c = 145\text{N/(m/s)}$, See Figure 3-8 for material properties..... 27

Figure 4-1: Comparison of force measurements and predictions assuming forces proportional to the uncut chip area. See section 4.2 for tool and material properties. 30

Figure 4-2: Three-dimensional cutting with a tool with a round nose..... 31

Figure 4-3: Chip flow direction as suggested by Colwell [12]..... 32

Figure 4-4: Normal force (F_n) and side force (F_r) with respect to approximate edge.... 33

Figure 4-5: Prediction considering chip flow direction as suggested by Colwell [12], see Figure 4-1 for tool and material properties.....	34
Figure 4-6: Variable approach angle method.....	35
Figure 4-7: Comparison of force prediction method based on Colwell's chip flow direction and variable approach angle method	35
Figure 4-8: Schematic of time domain Simulation.....	36
Figure 4-9: Chip area considering dynamic movements of tool in present and previous cuts	37
Figure 4-10: Chip area with dynamic movements, only circular part of the cutting edge is engaged	40
Figure 4-11: Results of time domain simulation ($\zeta_k = 0.05, \omega_{nk} = 600Hz$); The modal stiffness values are given as $k_{xx} = 40$, $k_{yy} = 100$, $k_{zz} = 25$, $k_{xy} = k_{yx} = 70$, $k_{zx} = k_{xz} = 25$, $k_{yz} = k_{zy} = 100$ [N/ μm], and cutting coefficients: $K_{n0} = 39$, $K_{r0} = -146$, $K_{t0} = -3$ [N]; $K_{nl} = 75000$, $K_{rL} = 90000$, $K_{tL} = 73000$ [N/m], $K_{nA} = 1065$, $K_{rA} = 647$, $K_{tA} = 2516$ [MPa]	43
Figure 4-12: Parameters of chip area (a): $a > r_\epsilon (1 - \cos \kappa_r)$ (b) $a \leq r_\epsilon (1 - \cos \kappa_r)$	44
Figure 4-13: Displacement of the cutting edge in the depth of cut direction (a) $a > r_\epsilon (1 - \cos \kappa_r)$, (b) $a \leq r_\epsilon (1 - \cos \kappa_r)$	50
Figure 4-14: Chip area with displacement in depth of cut direction in previous cut.....	51
Figure 4-15: Chip area with displacement in depth of cut direction in previous.....	53
Figure 4-16: Equal displacements in feed direction for in present and previous cut.....	54
Figure 4-17: Tool wear and process damping forces.....	55

Figure 4-18: Variable Approach Angle	56
Figure 4-19: Comparison of three stability prediction methods (a) stability chart for a tool $r_e = 0.8\text{mm}$, $\kappa_r = 60^\circ$ and $c = 0.1\text{mm/rev}$ (b) Effect of approach angle (c) Effect of nose radius; (d) Effect of feed. cutting coefficients: $K_{n0} = 39$, $K_{r0} = -146$, $K_{t0} = -3$ [N]; $K_{nl} = 75000$, $K_{rL} = 90000$, $K_{tL} = 73000$ [N/m], $K_{nA} = 1065$, $K_{rA} = 647$, $K_{tA} = 2516$ [MPa].	59
Figure 4-20: (a) Effect of nose radius and (b) effect of feed on stability limit. Tool: Sandvik CNMA1204 KR 3205 series coated inserts on DLCNL holder with -6° rake, -6° inclination, and $\kappa_r = 95^\circ$ approach angles, respectively.....	62
Figure 4-21: Comparison of predicted and experimentally observed chatter stability results for turning with sample vibration measurements at stable ($a = 2.5\text{ mm}$, $n = 200\text{ rev/min}$) and unstable ($a = 2.5\text{mm}$, $n = 400\text{rev/min}$) cutting conditions. Feed rate $c = 0.1\text{mm/rev}$ and nose radius $r_e = 0.8\text{mm}$. See Table 4-2 and Table 4-3 for the modal parameters and cutting coefficients respectively.	65
Figure 5-1: Milling of a flexible workpiece with a rotating and vibrating cutter.	71
Figure 5-2: Calculation of relationship between forces and vibrations	78
Figure 5-3: Setup for milling stability test.....	83
Figure 5-4: Predicted and measured milling forces in slot milling of AISI1045 steel. Cutting conditions: Spindle speed: 4297 rev/min, depth of cut: 0.25 mm, feed-rate= 0.1 mm/flute, number of inserts=2. Cutting coefficients are given in Table 5-1.....	83
Figure 5-5: Predicted and measured chatter stability results in slot milling of AISI 1045 steel with a two teeth cutter. Cutting conditions and parameters are given in Table 5-1 .	84

Figure 5-6: Time domain verification of analytical stability for slot milling with two inserts. (Cutting coefficients: $K_{rc} = 1978 \text{ MPa}$, $K_{tc} = 3242 \text{ MPa}$, $C_r = 0.61 \text{ N}/\mu\text{m}$, $C_t = 0.18 \text{ N}/\mu\text{m}$; modal parameters: $k_u = 15.7 \text{ N}/\mu\text{m}$, $\omega_{nu} = 1152 \text{ Hz}$, $\zeta_u = 0.023$; $k_v = 5.22 \text{ N}/\mu\text{m}$, $\omega_{nv} = 665 \text{ Hz}$, $\zeta_v = 0.023$).....	86
Figure 5-7: Sensitivity of stability charts to structural dynamic parameters of the system. Simulation conditions are same as Figure 5-6 except the following modal parameters are used: $k = 5.22 \text{ N}/\mu\text{m}$, $\omega = 2\pi \times 655 \text{ Hz}$, $\zeta = 0.023$	88
Figure A-1: Nyquist Contour	101
Figure A-2: Nyquist plot in stable and unstable cutting conditions.....	102
Figure A-3: Approximate Crossing Point.....	103
Figure B-1: Dynamic cutting test, AIS1045, width of cut $a = 0.5 \text{ mm}$, carbide tool, orthogonal cutting, Spindle Speed: 300rpm, oscillation frequency: 120Hz. The phase between inner and outer wave is zero.	108
Figure C-1: $g_j(\phi)$ functions for a five flute cutter with $\phi_c = 0$, $\phi_{st} = 15/180\pi$ and $\phi_{ex} = 80/180\pi$	109

List of Symbols

a, a_{lim}	Depth of cut, critical depth
c	Feed-rate (mm/rev)
d_{pq}	Directional coefficients ($p, q \in \{x, y, z\}$)
$g(\phi_j)$	Engagement pulse function (milling)
h_{cusp}	Cusp height
h, h_0	Height of the approximate chord with and without vibrations
h_c	Chip thickness normal to the chord
h_j	Chip thickness for flute j
\dot{h}	Vibration velocity normal to the cutting edge
$i = \sqrt{-1}$	Imaginary number
j	Tooth index
$k_i, \zeta_i, \omega_{ni}$	Stiffness, damping ratio and natural frequency of the mode i
$k_v, k_u, c_v, c_u, m_v, m_u$	Stiffness, damping, and modal mass in v and u directions
$\vec{n}, \vec{r}, \vec{t}$	Force coordinate system, aligned with the cutting speed and the approximate chord
w	Projection of approximate chord in feed direction
x, y, z	Machine coordinate system (turning)
x, y	Fixed coordinate system (milling), displacements in the fixed coordinate system

u, v	Rotating coordinate system, displacements of the tool in rotating coordinate system
C_y, C_z	Process damping coefficients in feed and cutting speed directions
C_r, C_t	Radial and tangential process damping coefficients
F_{dp}	Differential damping force in p direction $p \in \{x, y, z\}$
F_d, F_{dz}	Process damping and friction forces
F_n, F_r, F_t	Cutting forces in $\vec{n}, \vec{r}, \vec{t}$ frame
$F_{r,j}, F_{t,j}$	Radial and tangential dynamic forces on flute j
F_v, F_u	Dynamic cutting force components in the rotating coordinate system
F_x, F_y	Dynamic cutting force components in the fixed coordinate system
K_{rc}, K_{tc}	Radial and tangential cutting coefficients
K_{tA}, K_{nA}, K_{rA}	Cutting force coefficients for chip area
K_{tL}, K_{nL}, K_{rL}	Cutting force coefficients for chord length
K_{t0}, K_{n0}, K_{r0}	Cutting force coefficient offsets
K_{sp}	Contact force coefficient
L, L_{lim}	Length and critically stable length of the approximate chord
L_w	Flank wear length
L_{κ_r}	Length of straight section of the cutting edge in cut
N	Number of flutes
V_c	Cutting speed

V_m	Volume of compressed work material under the tool
$\mathbf{A}, \mathbf{B}, \mathbf{E}, \mathbf{C}, \mathbf{D}, \mathbf{F}$	2x2 sub-matrices of 4x4 directional matrices in milling
$[\mathbf{C}_{nm}]$	Transformation matrix from machine to the force coordinates
$\{\mathbf{F}_m\}$	Cutting force vector in machine coordinate system
$[\mathbf{J}], [\mathbf{J}_\tau], [\mathbf{J}_v]$	Direct, delayed displacement gain and process damping matrix, respectively
$[\mathbf{K}_c]$	Cutting force coefficient matrix
$\{\mathbf{Q}\}, \{\mathbf{S}\}$	Displacement vectors in machine and force coordinate systems
$\mathbf{P}(t), \mathbf{Q}(t), \mathbf{J}(t)$	Time varying directional matrices of direct, delay and process damping gains
r_ϵ, κ_r	Nose radius and approach angle of the tool
μ_c	Coefficient of friction between the tool flank and the workpiece
θ	Angle of the approximate chord with feed direction
Φ_0	Effective transfer function
ϕ_c	Angle between the first flute and v
ϕ_{st}, ϕ_{ex}	Entry and exit angles of tooth from the cut
ϕ	Rotation angle of the tool (angle between v and x)
$[\Phi]$	Three dimensional transfer function matrix of the structure
$[\Phi]_{vu}, [\Phi]_w$	Transfer function of the rotating tool/spindle and workpiece

Acknowledgment

I would like to thank my supervisor, Professor Yusuf Altintas for accepting me in Manufacturing Automation Lab and for his guidance, help and support during my PhD research.

I learned a lot from our visiting engineer Hideaki Onozuka from Hitachi, Japan. His hard work, smart ideas and approach to experiments were truly inspiring for me.

I would also like to thank staff engineers and technicians of the department of mechanical engineering in UBC; especially Bernhard Nimmervoll and Glenn Jolly for their assistance in preparing experimental setups.

Many thanks to my friends and colleagues in Manufacturing Automation Lab for their stimulating discussions and good suggestions during this project.

Finally, I am thankful of my parents for their help, support and patience during my stay in Canada.

Chapter 1: Introduction

Machine tool vibrations are the fundamental obstacle for ensuring accuracy and productivity in machining industry. Unless avoided, they damage the machine tool and scrap the workpiece.

The structural vibrations of a machine tool form a closed loop system with the cutting forces; Cutting forces create displacements between the tool and the workpiece during machining and in return, movements between the tool and the workpiece affect the cutting forces. Vibration marks left on the machined surface affect the cutting forces in the successive pass and would lead to increased vibrations of the system if the process is not intrinsically stable against the vibrations due to a large width of cut, large cutting coefficients, or flexible structure. Cutting forces depend on the tool geometry, material properties, feed rate and cutting speed. In an unstable process the amplitude of vibrations may grow exponentially until they become as large as chip thickness. This unstable vibration of the tool with respect to the workpiece is known as chatter, which creates large cutting forces that may damage the machine, cutting tool and the workpiece.

The dynamics of the chatter system is described by delayed differential equations with constant or time varying periodic coefficients depending on the type of the machining operation. The parameters of the system are functions of work material properties, tool geometry, kinematics of machining operation, and structural dynamics of both machine and workpiece.

Significant research effort has been made in modeling and predicting the chatter stability of machining operations. The past methods enabled the industry to predict chatter free cutting conditions at high cutting speeds where the stabilizing effect of the contact between the flank face of the tool and wavy surface finish is negligibly small. Such high-speed cutting operations are mainly applied in milling aircraft parts made from aluminum alloys which are benefited from recent chatter stability theories significantly. The metal removal rates have been increased by several folds by selecting stable depth of cuts and high spindle speeds.

However, the tool's flank face rubbing against the wavy workpiece surface in low-speed machining, creates process induced damping which has not been modeled satisfactorily since it was noticed by Tobias [46] in late 1950s. The process, which mainly occurs in low speed machining, is further complicated when the tool flank wear land is almost as large as the vibration wave length imprinted on the finish surface. There have been numerous attempts in modeling the time-varying contact mechanics between the wavy workpiece surface and flank face of the tool. However, there has not been a successful application of past models due to poor repeatability of experimental results, and complications that arise due to poor shearing of material at low cutting speeds. Furthermore, the low-speed cutting is mainly conducted in single point turning and boring operations where the depth of cut is small compared to the nose radius of the tool. The process force gains become nonlinear functions of operating conditions (i.e. feed, depth of cut) and tool geometry that further complicate the modeling of process dynamics for stability analysis.

This thesis presents measurement and modeling of process damping mechanism in metal cutting at low cutting speeds. The process damping is incorporated into the dynamic models of turning and milling operations, and their chatter stability is predicted in the frequency domain. The process and chatter stability models are experimentally validated in turning and milling tests.

Henceforth, the thesis is organized as follows: The past research on modeling the dynamics of cutting process, process damping, and chatter stability in turning and milling is critically reviewed in Chapter 2. The modeling, measurement and identification of dynamic cutting force coefficients are presented in Chapter 3. Ideal dynamic cutting forces are created by adjusting the regenerative phase between successive spindle periods using a piezo-actuator-driven fast tool servo in orthogonal cutting tests. The process damping coefficients are extracted by transforming measured time domain forces and vibration into the frequency domain. The dynamics of turning with tools having a nose radius are modeled in Chapter 4. The dynamic cutting force model considers the effects of nose radius, approach angle, feed-rate, depth of cut, cutting speed, flank wear and structural dynamics of the system. A new three-dimensional dynamic cutting model which considers the regeneration of chip area and process damping caused by flank contact is proposed. The stability of the system is solved in the frequency domain using Nyquist stability criterion with experimental validation.

A new dynamic milling model is introduced in Chapter 5. The model considers the asymmetric structural dynamics of the rotating tool, stationary dynamics of the workpiece and speed-dependent process damping coefficient. The system's time varying periodic coefficients are averaged in rotating tool coordinates, and the stability of general milling system is solved using Nyquist stability criterion. The proposed stability solution is compared favorably against numerical simulation and milling test results. The thesis is concluded in Chapter 6 by summarizing the contributions to the stability of low speed turning and milling operations. The detailed mathematical derivation steps for some of the dynamic models are given in Appendices.

Chapter 2: Literature Survey

2.1 Overview

The main aim of this thesis is to improve chatter stability prediction methods for turning and milling operations. Chatter stability limits are used to locate the stable metal removal conditions to maximize the productivity of machining operations. The stability prediction requires mathematical modeling of process mechanics and dynamics. The metal cutting is a large field with diverse applications and challenges. However, this thesis focuses on the modeling of three-dimensional mechanics and dynamics of turning and milling operations with process damping effects at low cutting speeds; hence, topics related to the research focus are surveyed in this chapter.

The organization of this chapter is as follows: In section 2.2 the literature on the dynamics of orthogonal cutting and chatter stability is discussed. The previous theories on process damping are presented in section 2.3. In section 2.4, the literature on stability of three-dimensional turning is summarized. Finally, the literature on stability prediction in milling with process damping is discussed in section 2.5.

2.2 Dynamics of Metal Cutting Process

Chatter is the vibration instability of a machining system. It leads to destructive, oscillating cutting forces generating vibration marks on a machined surface, as shown in Figure 2-1 and Figure 2-2. The vibrating forces, which could reach magnitudes several

times larger than that of a stable cutting, decrease the life of the tool and the machine drastically, and may lead to tool breakage and premature wear of spindle bearings.

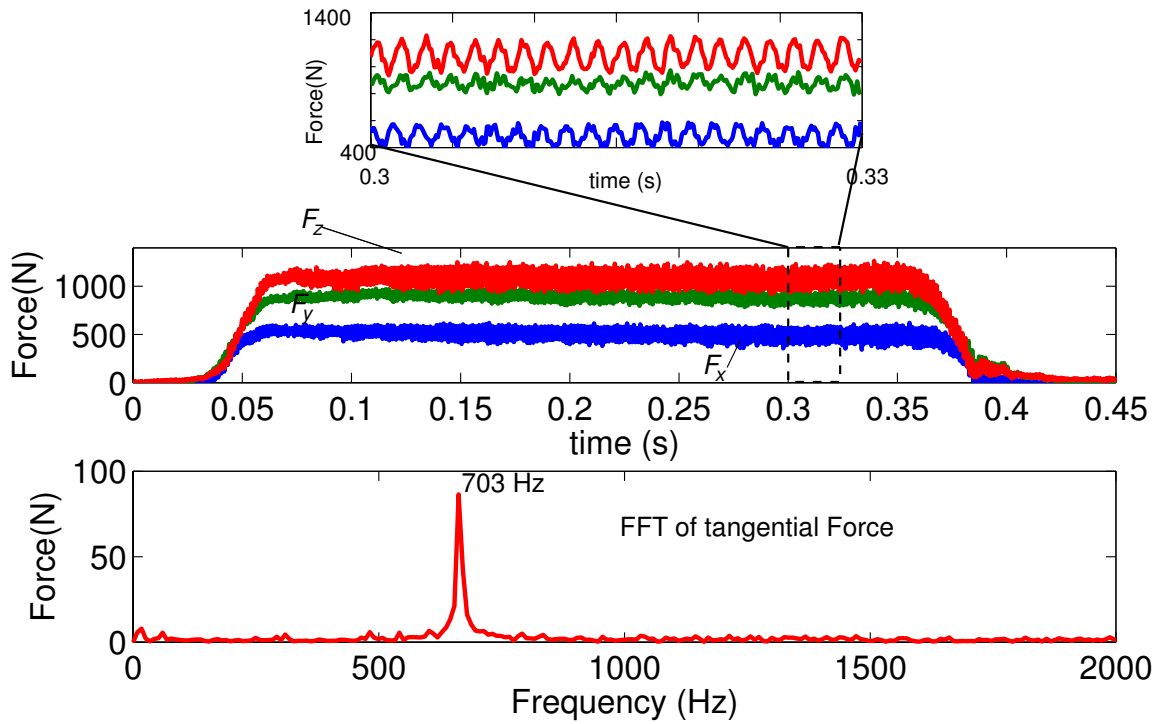


Figure 2-1: Cutting forces during chatter



Figure 2-2: Photomicrograph of workpiece surface: (a) stable cutting, (b) chatter, (c) vibration marks as seen by naked eyes

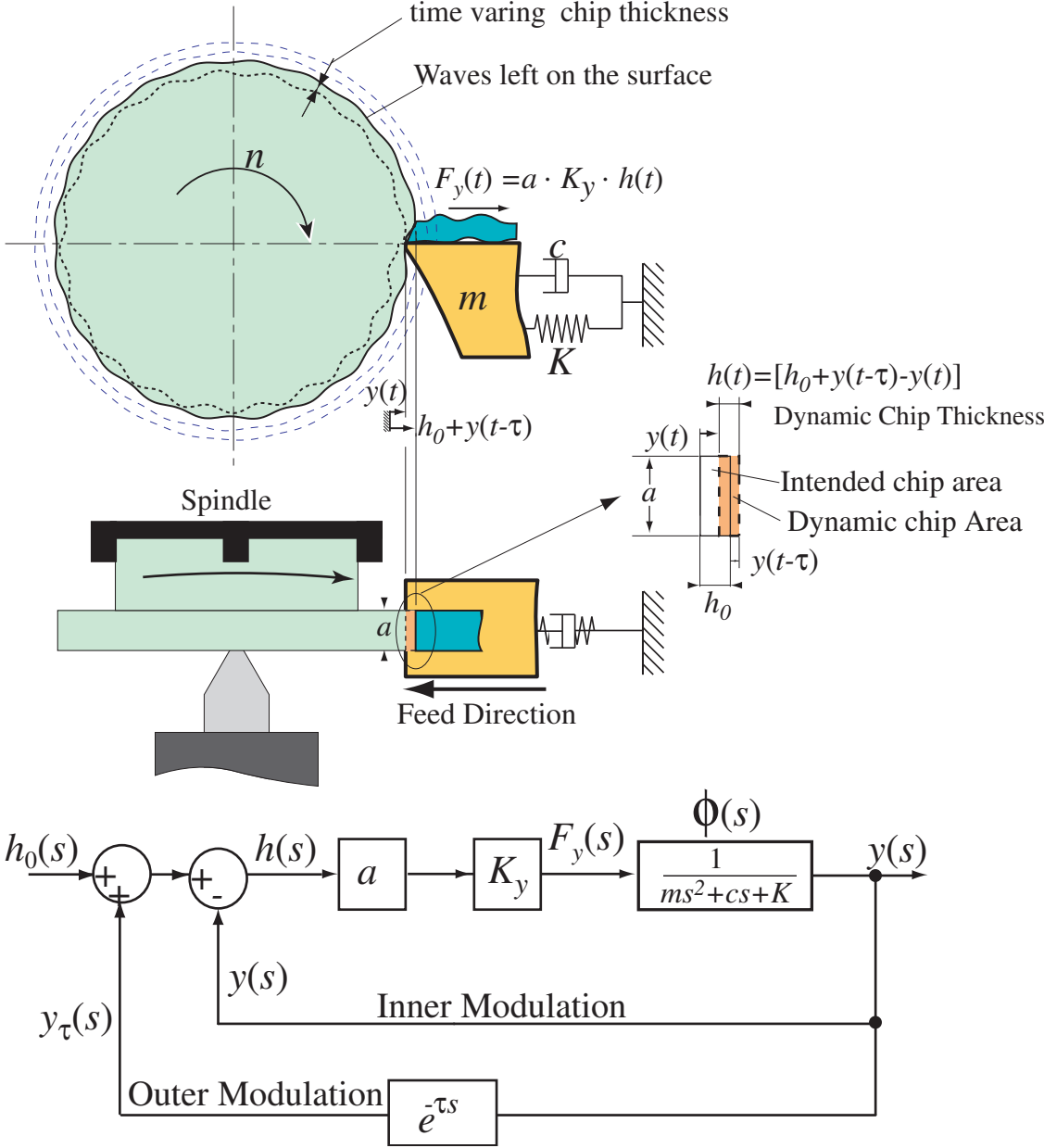


Figure 2-3: Chatter in orthogonal cutting with block diagram

A simple tool with one degree of freedom is presented in Figure 2-3 along with a block diagram describing the system's dynamics in the Laplace domain. τ is the spindle period and the intended chip thickness is h_0 , but vibration in the feed-force direction $y(t)$, known as the inner modulation, decreases the dynamic chip thickness, shown as $h(t)$,

while vibration mark's height left from the previous pass, $y(t - \tau)$ known as the outer modulation, increases the dynamic chip thickness; therefore,

$$h(t) = h_0 + y(t - \tau) - y(t) \quad (2-1)$$

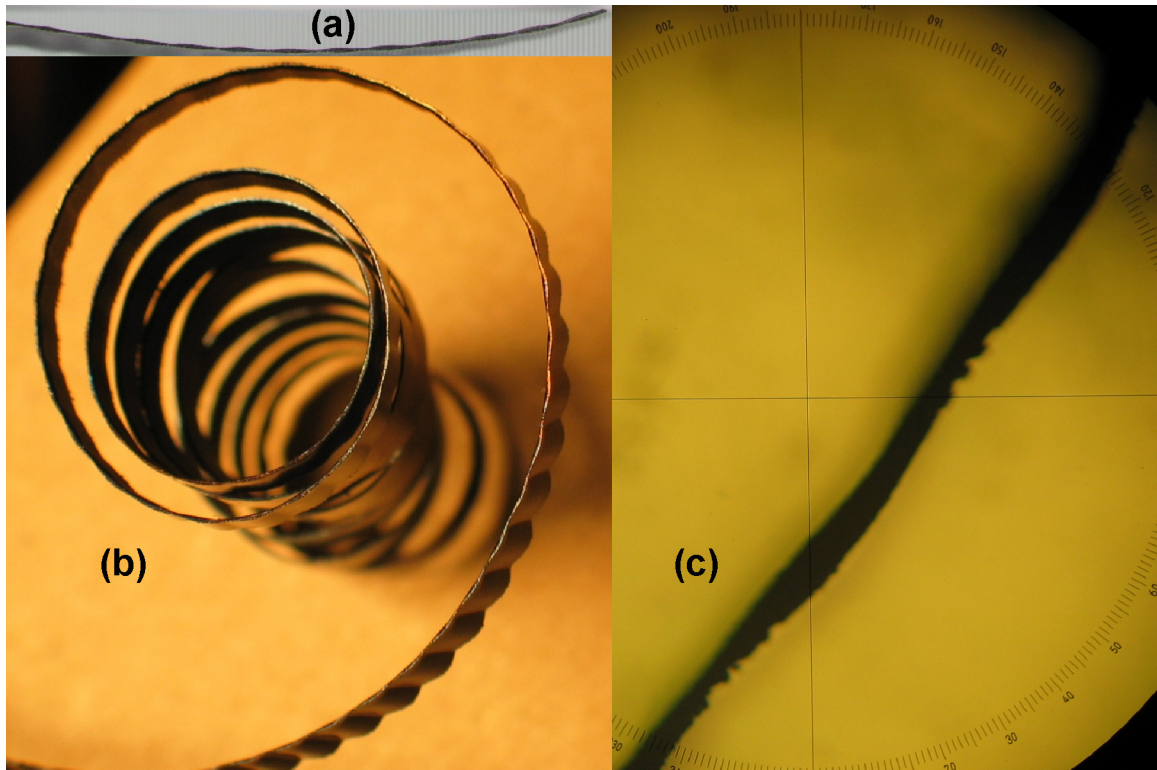


Figure 2-4: Inner and outer waves on chips (a), (b) regular camera, (c) under a microscope

When there is a phase shift between $y(t)$ and $y(t - \tau)$, the dynamic chip thickness varies at the frequency of vibration (see samples in Figure 2-4) and creates a vibrating cutting force $F_y(t)$ which could amplify the vibration of the tool. This phenomenon only happens if the depth of cut (a) and cutting coefficient in feed direction (K_y), which act as gains in the block diagram, are large enough compared to the stiffness (K) and damping ratio ($\zeta = c / 2\sqrt{mK}$) of the structure holding the tool. The oscillation energy in the structure is only dissipated by damping. If the energy diverted from the machining

process by chip thickness variations is larger than the vibration damping capacity of the structure, the amplitude of the vibrations will grow until the vibration amplitude is large enough to make the tool leave the workpiece and create zero chip thickness.

In 1946 Arnold [7] suggested that a decrease in cutting force due to the increase in the cutting speed leads to a negative damping effect and causes instability of a cutting process. Later Hahn [17] demonstrated that such an effect is not strong enough as the sole reason for instability. Regeneration of undulations was first discovered by Doi and Kato; They showed that the regeneration of the chip thickness causes oscillating cutting forces, which in turn excites the vibrations of the structure [14].

Thusty et al. [42] and Tobias et al. [46] suggested the relationships for the prediction of threshold of stability considering regeneration. Later, Merritt [26] presented the same model as a closed loop system as shown in Figure 2-3[26]. The stability of the system solved by Thusty is given by:

$$a_{lim} = -\frac{1}{2K_y \cdot \min(\text{Re}[\phi(j\omega)])} \quad (2-2)$$

where $\phi(j\omega) = (K + cj\omega - m\omega^2)^{-1}$ is the frequency response function of the structure between the tool and the workpiece.

2.3 Process Damping

When the ratio of the vibration frequency over cutting speed is very high, which occurs at low-speed milling and most turning and boring operations, the stable depth of cut increases. The increase of the stable depth of cut has been attributed to either the change in the direction of cutting speed hence the force [13], or the friction between the

clearance face of the tool and wavy workpiece finish surface [5][38][23] which is referred to as process damping mechanism as illustrated in Figure 2-5.

Albrecht [1] modeled the ploughing between the clearance face and rounded cutting edge of the tool, and Sisson et al. [38] showed the round cutting edge's effect on the damping of the cutting process. The mechanics of contact between a wavy surface and a tool's clearance face as well as a cutting edge with a radius has been a challenging tribology problem. Montgomery and Altintas used indentation model of tool clearance face with the wavy surface finish in milling [29] but further investigation with this method was impeded by numerical instability in their numerical simulation. Wallace and Andrew [48] and later Chiou and Liang [10] proposed an improved model of indentation with experimentally calibrated contact forces. They showed that the flank wear increases damping, especially at low cutting speeds. Clancy and Shin considered a turning tool with nose radius and flank wear [11]. They considered the interference between the tool and wavy surface finish using the extended model of Chiou and Liang, and proposed a three-dimensional chatter stability using an eigenvalue solution method [10]. Huang and Wang identified process damping coefficient from the measured cutting forces and vibrations in milling [20]. They showed the presence of process damping forces in milling.

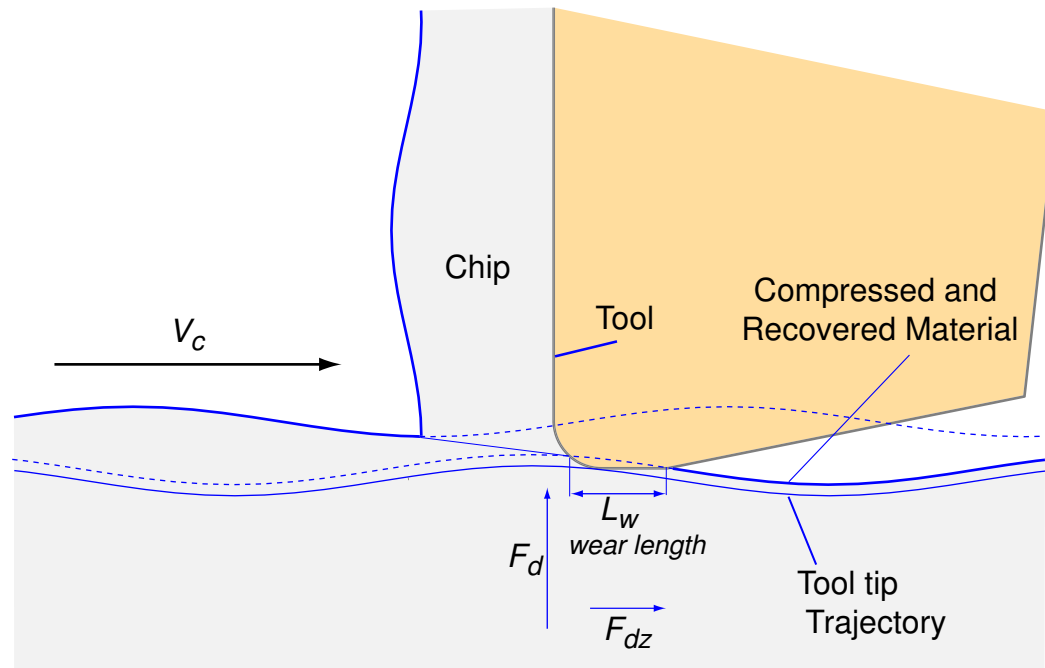


Figure 2-5: Process-damping mechanism as suggested by Wallace and Andrew [48]

The accurate modeling of contact forces as a function of vibration frequency, cutting speed, tool geometry and work material properties remain an academic challenge[5]. Tlustý reported experimental results from several leading research laboratories where a standard experimental set up is used to measure the dynamic cutting force coefficients which contain both the influence of vibration frequency and cutting speed dependent damping, as well as the damping contributed by ploughing of the clearance face of the tool [41]. Although the set up and material were the same, the measured dynamic cutting force coefficient results varied among institutes, which was blamed to the difficulties in the measuring instrumentations available in 1970s [34].

In chapter 3, a new dynamic cutting force measurement system is introduced. The results of dynamic cutting tests are used for direct stability prediction with process damping. Also, dynamic cutting tests with tools with different wear lands indicate the relationship between the tool wear and dynamic cutting forces.

2.4 Stability of Three Dimensional Turning

In the early years of chatter research, studies were concentrated on cutting tools with a single-straight edge as shown in Figure 2-3. In practice, in a turning or boring operation, the chip is generated by a tool which is engaged in the workpiece with a straight cutting edge, a curved cutting edge and a minor straight cutting edge as shown in Figure 2-6. The radius of corner curvature in a turning tool is comparable to the axial depth of cut. A larger nose radius makes the tool stronger against breakage and provides a better surface finish. Modern medium-sized carbide tools usually have a nose radius ranging from 0.8mm to 2.4 mm or more, and the nose radius area makes up a large portion of the chip area. The whole cut is in the nose radius area for small depth of cuts and in cutting operations with round inserts.

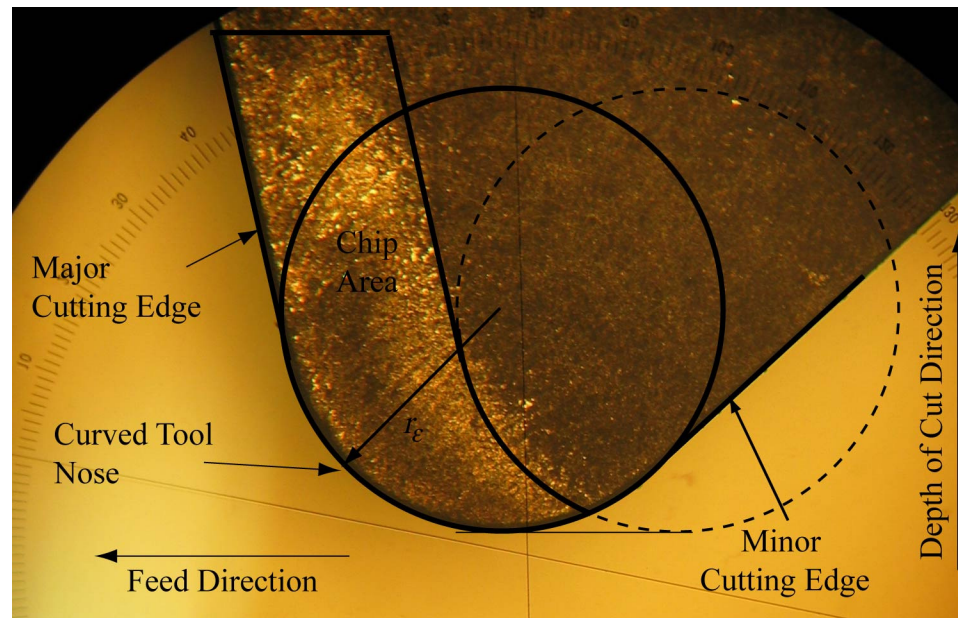


Figure 2-6: Photomicrograph of rake face of a turning tool; chip area has a lighter color due to the wear on rake face

There is a nonlinear relationship between the chip area and the cutting forces in the depth of cut and feed directions due to the nose radius of the tool. The nose radius makes the

coefficients of delayed differential equations dependent on the depth of cut and feed; but these coefficients are considered constant in the past stability prediction methods [32].

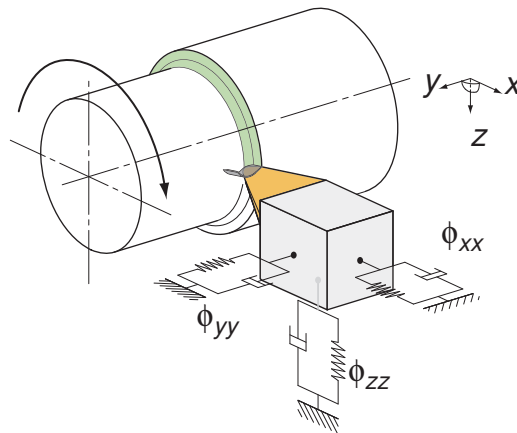


Figure 2-7: Three-dimensional flexibility in a turning operation

Another aspect of the stability prediction in turning is that the vibrations are excited in multiple directions, depending on the tool geometry and flexibilities of the system. A sample turning tool is shown in Figure 2-7 where the cutting forces act in all three directions while the system has dynamic flexibilities. The chip area is dependent on vibrations in both depth of cut (x) and feed (y) directions. Oscillations in feed, depth of cut and cutting speed (z) directions are coupled due to coupling of the structure and cutting mechanism. Opitz developed a one-dimensional analysis by assuming a zero tool nose radius and developed the concept of directional transfer function which is a linear summation of weighted direct and coupled transfer functions due to their orientation with respect to the cutting forces [32]. Rao et. Al developed an parallelogram approximation for chip area[35] while Reddy et. al. approximated the chip area with a triangle and obtained the stability for structural modes in one major flexible direction [36]. Atabey and Lazoglu simulated the process in time domain for a boring tool with nose radius, and studied its stability [8], [24]. Ozlu and Budak [33] improved the modeling of turning

dynamics by dividing the chip into discrete zones or small discrete force elements; however, this method is more accurate in stability prediction in the feed direction rather than the depth of cut direction. In chapter 4 of this thesis, cutting forces for tool with nose radius are predicted based on Colwell's chip flow direction theorem [12], and a new stability prediction method is introduced by modeling the transfer matrix between the displacements and cutting forces. Process damping force is also included, and the stability prediction is analytically performed using Nyquist stability criterion.

2.5 Stability of Milling Operations

Turning, boring and drilling tools create continuous chips while milling tools produce crescent-shaped chips as their flutes engage in and disengage out of the workpiece material during rotation. Discontinuous cutting, combined with the rotation of the cutting edge, makes the study of chatter in milling more challenging. Tlustý et. al presented time domain, numerical simulations and considered process damping and nonlinearities [45]. Sridhar et. al. proposed the concept of state transition matrix, calculated by time domain simulation. In this method, an eigenvalue of the state transition matrix outside of the unit circle indicates machining instability [39]. Minis and Yanushevsky [27] predicted chatter analytically using Nyquist stability criterion along with the concept of parametric transfer functions and Fourier analysis. Altintas and Budak [3], [9] developed single-frequency and multi-frequency matrix eigenvalue methods to calculate stability limits directly.

Both Minis et. al and Altintas et. al considered dynamic variables represented in a fixed coordinate system. While it is convenient and acceptable to use a fixed coordinate system to study the dynamics of any axis-symmetric flexible tool/spindle, the dynamics of a system with tools of unequal orthogonal modes should be studied in a rotating coordinate

system. Rotating coordinate systems are employed in the study of dynamics of asymmetric rotors and the effects of dry friction between the components of a rotor [30].

In an earlier work, Li, Ulsoy and Endres [25] studied the effects of flexible tool rotation on chatter stability for boring and predicted different stability limits for stationary boring bars compared to the rotating boring bars.

The new model developed in chapter 5 of this thesis considers two additional dynamic variables for rotating spindle in addition to dynamic variables of non-rotating structure. Process damping effect, which arises in low cutting speeds, is also considered. The model predictions in different cutting conditions and structural dynamic configurations are compared with experiments and time domain simulations.

Chapter 3: Orthogonal Cutting with Process Damping

3.1 Overview

Heat resistant and high strength alloys are machined at low cutting speeds where the chatter stability is still an unsolved phenomenon. This chapter presents a cutting force model which has dynamic cutting force coefficients related to regenerative chip thickness and vibration velocity respectively. The dynamic cutting force coefficients are identified from controlled orthogonal cutting tests with a fast tool servo oscillated at the desired frequency to create inner or outer modulations. The velocity term contributes to the damping in the process. It is shown that the process damping coefficient increases as the tool is worn, which increases the chatter stability limit in cutting. The chatter stability of the dynamic cutting process is predicted using Nyquist stability criterion, and compared against experimental results. Stability of the cutting process is predicted properly at low cutting speeds, provided that the dynamic cutting force coefficients governed by the contact between the wavy surface finish and tool flank are accurately identified.

3.2 Modeling of Process Damping Forces

Several experiments, such as those described in [13] and [48], show that a part of the force between the tool and workpiece is proportional to the speed of the tool vibration with respect to the workpiece and the slope of the waves left on the surface being cut. These forces add to the damping in the system and are known as process damping forces. Several explanations are proposed in literature for the origin of these forces [41]. Das and

In these equations, $y(t)$ and $y(t - \tau)$ are the inner and outer vibrations, and K_y and K_z are the static cutting force coefficients in feed and cutting speed directions respectively. V_c is the cutting velocity, a is the width of cut, c is the feed per revolution, and τ is the time delay between the inner and outer vibration waves. The velocity term $(-y/V_c)$ introduced by Tobias increases the damping in the system $(C + K_z ac/V_c)$ at low cutting speeds [13]:

$$\begin{aligned}
 m\ddot{y}(t) + C\dot{y}(t) + Ky(t) &= K_y a [h_0 - y(t) + y(t - \tau)] - K_z ac \frac{\dot{y}}{V_c} \\
 \Rightarrow m\ddot{y}(t) + \left(C + \frac{K_z ac}{V_c} \right) \dot{y}(t) + Ky(t) &= K_y a [h_0 - y(t) + y(t - \tau)]
 \end{aligned} \tag{3-4}$$

While Tobias's modified dynamic cutting process model leads to increased stability at low speeds, it fails to properly predict the stability limit and also explain the increased stability of worn tools. Sisson and Kegg [23], [38] proposed a theorem which considers the effect of tool wear on process damping as a worn tool is expected to have a larger cutting edge radius (shown as R in Figure 3-2). Sisson and Kegg suggested that a part of chip thickness, proportional to the cutting edge radius (bR , $b \cong 0.25$), is compressed under the edge radius instead of moving up the rake face and becoming a part of chip. The compressed material exerts a reaction force proportional to the material yield strength σ_y and inversely proportional to the clearance angle γ . During a vibration, the effective clearance angle γ changes proportional to the vibration speed and this creates a dynamic force, proportional to the vibration speed and inversely proportional to the cutting speed.

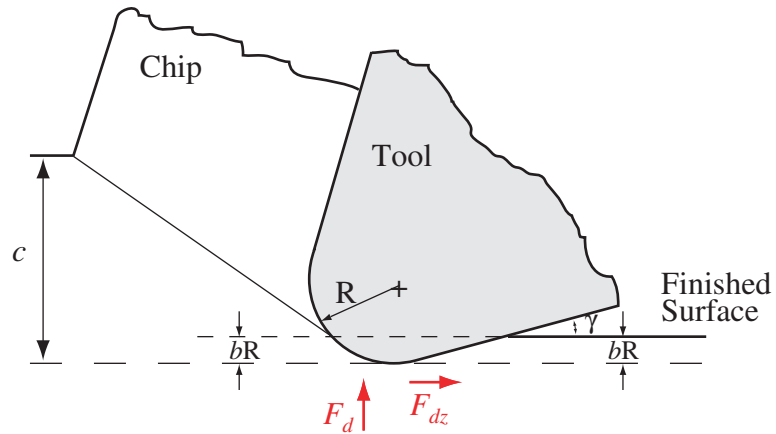


Figure 3-2: Work material compression under the cutting edge radius as a source of process damping force as described by Sisson and Kegg [38]

The process damping force in this model is expressed as:

$$F_d = -a\sigma_y \frac{bR}{\gamma^2} \frac{\dot{y}}{V_c}, \quad F_{dz} = \mu F_d \quad (3-5)$$

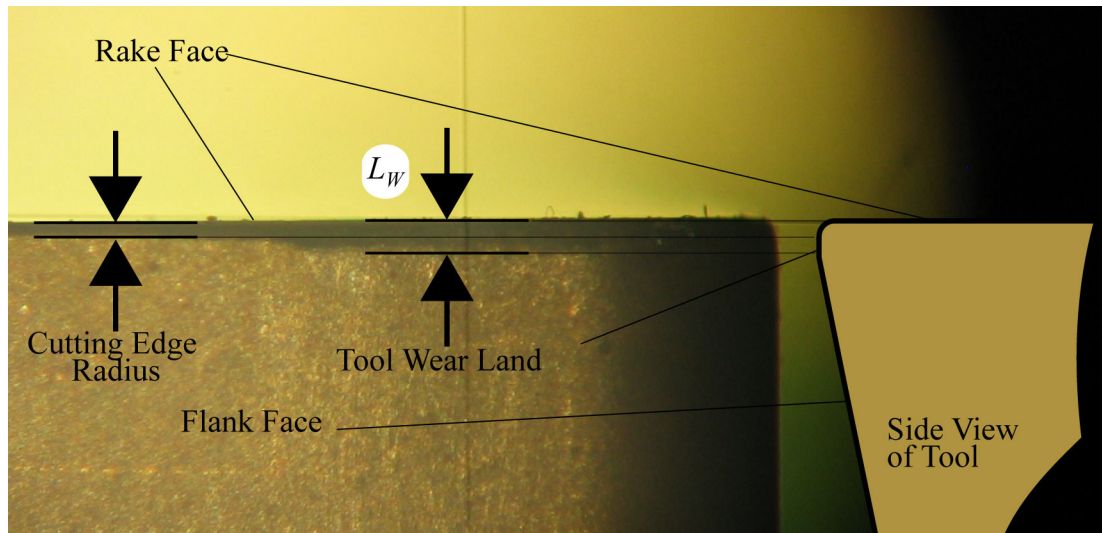


Figure 3-3: Photomicrograph of tool wear land

An alternative explanation was proposed by Wallace and Andrew [48], Wu [49] and Chiou and Liang [10]. This approach was different from Kegg and Sisson's due to its stress on the cutting edge wear length (L_w , see Figure 3-3) instead of cutting edge radius and clearance angle as controlling parameters of the process damping force. They

explained process damping as the force generated when a volume of work material is compressed under the tool wear land as shown in Figure 3-4. From this figure, V_m is calculated as:

$$V_m = V_{m0} - a \cdot \frac{L_w^2}{2} \cdot \frac{\dot{y}}{V_c} \quad (3-6)$$

where V_{m0} is the volume of compressed material without vibration. The flank contact force is proportional to V_m with the material specific “contact force coefficient”, K_{sp} :

$$F_d = K_{sp} V_m, \quad F_{dz} = \mu F_d \quad (3-7)$$

In [10], a tool penetration test is described for measuring K_{sp} of the work material. $\mu = 0.3$ is suggested for steel workpiece in [50].

Dropping the constant V_{m0} part in (3-6), the dynamic process damping force equation (3-7) becomes:

$$F_d = -K_{sp} a \cdot \frac{L_w^2}{2} \cdot \frac{\dot{y}}{V_c}, \quad F_{dz} = -\mu \cdot K_{sp} a \cdot \frac{L_w^2}{2} \cdot \frac{\dot{y}}{V_c} \quad (3-8)$$

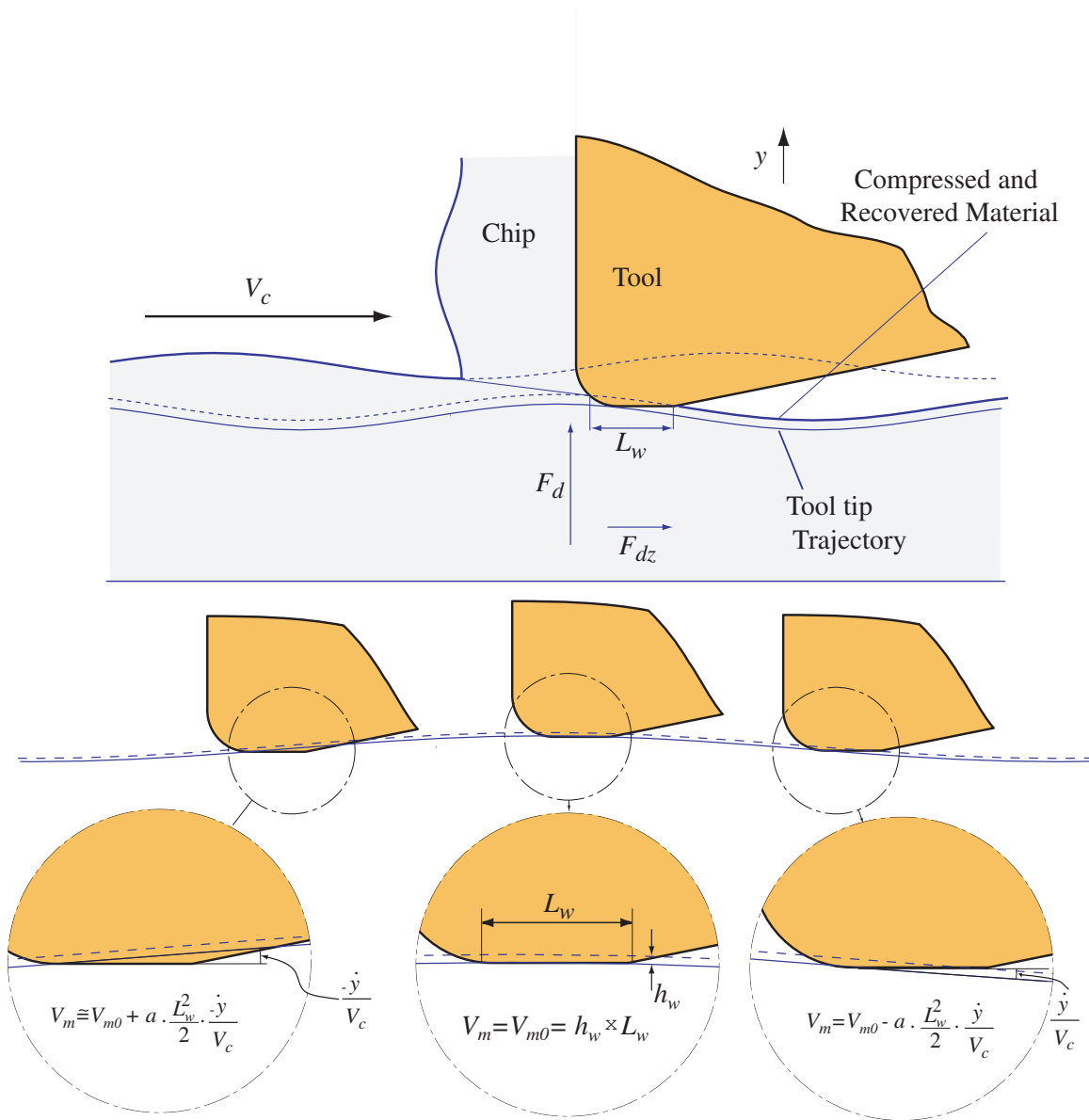


Figure 3-4: Work material compression under the tool flank, as proposed by Wallace et al [48]

The relationship between the process damping force and vibration velocity could be written using the simplifying process damping coefficient C_y and C_z which are defined as:

$$C_y = \frac{-F_d}{a(\dot{y} / V_c)}, \quad C_z = \frac{-F_{dz}}{a(\dot{y} / V_c)} \quad (3-9)$$

In Table 3-1, the process damping coefficients are represented per different process damping theories. Experimental results presented in the next section are in agreement with the process damping model proposed by Chio and Liang [10], and Wallace and Andrew [48].

Table 3-1: process damping coefficient determined with different theories

	Das and Tobias [13]	Sisson and Kegg [38]	Wallace and Andrew [48] / Chio and Liang [10]
C_y	$K_z c$	$\sigma_y \frac{bR}{\gamma^2}$	$K_{sp} \cdot \frac{L_w^2}{2}$
C_z	$-K_y c$	μC_y	μC_y

3.3 Identification of Process Damping Forces with Oscillation Cutting

Tests

While the static cutting force coefficients (K_y, K_z) are identified from vibration-free orthogonal cutting tests by cutting at different feed-rates, the velocity-dependent cutting force coefficients (C_y, C_z) could only be identified from a set of dynamic cutting tests.

When a harmonic motion ($y(t) = Y e^{j\omega t}$) is applied to the cutting tool with a frequency ω and amplitude Y , the dynamic cutting force equation becomes:

$$\begin{aligned}
 F_y(t) &= K_y a c + a Y e^{j\omega t} \left\{ -K_y [1 - e^{-j\omega\tau}] - j \frac{C_y \omega}{V_c} \right\} \\
 F_z(t) &= K_z a c + a Y e^{j\omega t} \left\{ -K_z [1 - e^{-j\omega\tau}] - j \frac{C_z \omega}{V_c} \right\}
 \end{aligned} \tag{3-10}$$

The length of the vibration wave imprinted on the surface is $\lambda = V_c \frac{2\pi}{\omega}$, which leads to

$\omega/V_c = 2\pi/\lambda$. The modified dynamic cutting force expression for y direction

becomes:

$$F_y(t) = K_y a h_0 + a Y e^{j\omega t} \left[K_y (1 - e^{-j\omega\tau}) - j \frac{2\pi}{\lambda} C_y \right] \quad (3-11)$$

which correlates the process damping forces to the vibration wave length (λ) or the ratio of vibration frequency over cutting speed (ω/V_c).

The dynamic cutting force coefficients have been identified from a series of orthogonal plunge turning of cold-rolled AISI 1045 steel, stainless steel SS304 and Aluminum 7075 bars on an instrumented CNC lathe as shown in Figure 3-5. A carbide grooving tool with 2.4 mm edge width, zero degree rake and 7 degree clearance angle has been mounted on a piezo-actuator-driven fast tool servo.

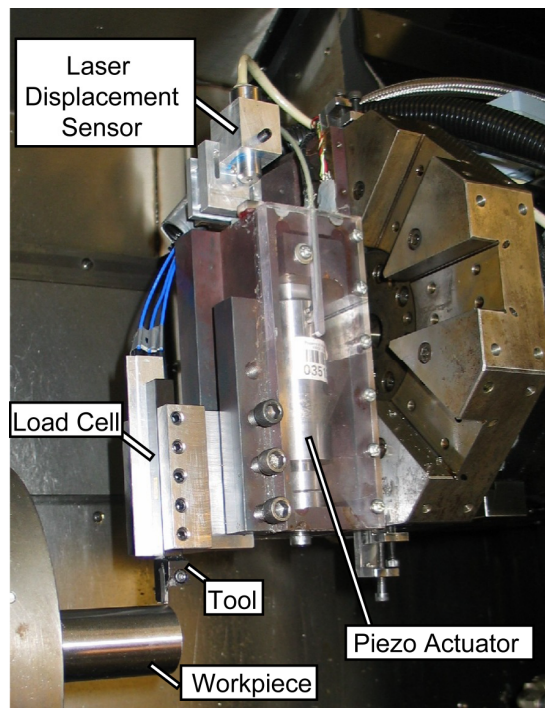


Figure 3-5: Dynamic cutting force test rig

An integrated laser sensor measures the displacement of the tool, and a three-component load cell fitted between the tool and the tool holder measures the dynamic cutting forces. The fast tool servo is mounted on the turret of the machine as rigidly as possible. While the CNC lathe provides the macro positioning and feed motion (c), the fast tool servo is used to generate vibrations at the desired frequency and amplitude.

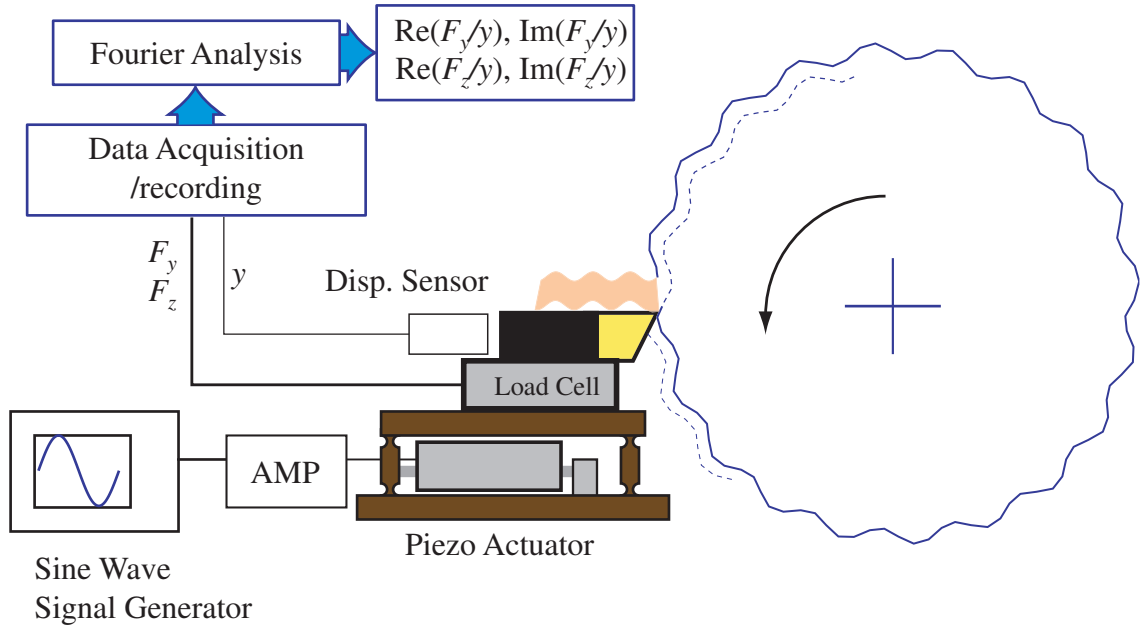


Figure 3-6: Schematic of oscillation cutting tests

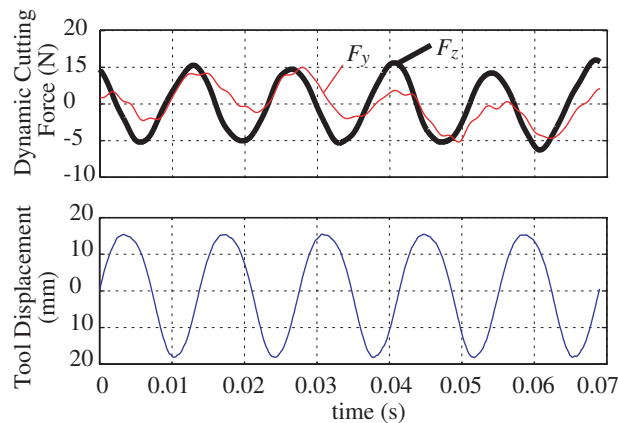


Figure 3-7: Sample measurements during dynamic plunge turning test. Work material: Stainless Steel SS304, Tool: Sandvik Coromant N123 H13A with 0 degree rake and 7 degree clearance angle. The width of cut: 0.5 mm, feed: 0.050 mm/rev. spindle speed: 2174 rev/min, tool oscillation frequency: 72.59 Hz (DC components are removed).

The tool displacement and cutting forces are measured simultaneously during dynamic cutting tests as shown in Figure 3-6. A sample cutting force and displacement measurement is shown in Figure 3-7. The inner and outer waves are synchronized to be in phase ($1 - e^{-j\omega\tau} = 0$) by generating integer number of vibration cycles per spindle revolution during the identification tests, i.e.,

$$\begin{aligned} F_y(t) &= K_y ac + aY e^{j\alpha} (-jC_y \frac{2\pi}{\lambda}) \\ F_z(t) &= K_z ac + aY e^{j\alpha} (-jC_z \frac{2\pi}{\lambda}) \\ y(t) &= Y e^{j\alpha} \end{aligned} \quad (3-12)$$

Therefore, a Fourier analysis at frequency ω results in:

$$\begin{aligned} \text{Im}(F_y / ay) &= -\frac{2\pi C_y}{\lambda} \\ \text{Im}(F_z / ay) &= -\frac{2\pi C_z}{\lambda} \end{aligned} \quad (3-13)$$

The dynamic cutting force coefficient is extracted using the least squares method applied on the frequency domain representation of measured forces as shown in Figure 3-8. The diameter of the workpiece is 35 mm, the spindle speed is varied between 200 and 4000 rev/min, and the piezo actuator delivered sinusoidal displacement between 10 to 120 Hz with $35 \mu m$ amplitude in constructing the results given in Figure 3-8. The imaginary part, or added damping to the process, corresponds to $(-C_y 2\pi / \lambda)$ especially when the wave length is smaller than 10 mm in this particular test case. The positive sign for C_z indicates that changes in the direction of cutting forces, as described by Das and Tobias, could not explain the process damping mechanism completely.

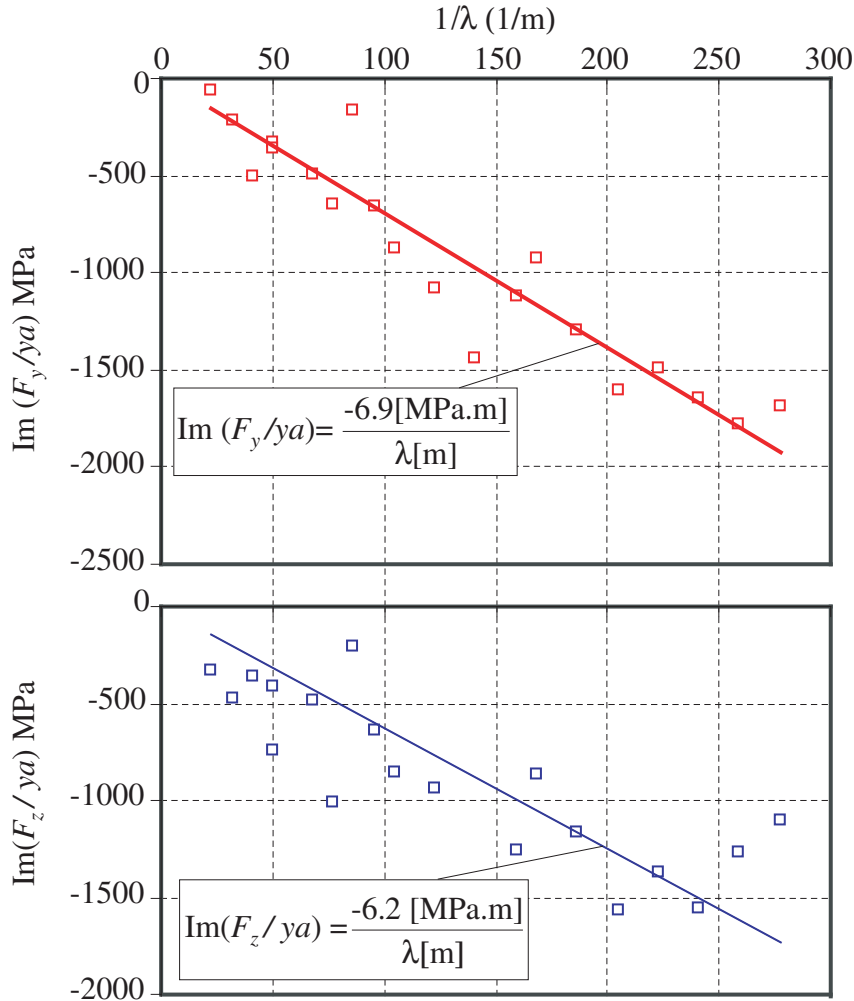


Figure 3-8: Process gain versus inverse wavelength with zero phase shift between inner and outer oscillations. Material: AISI1045, Cutting force coefficients: $K_z = 2580$ MPa, $K_y = 1384$ MPa, $C_y = 6.9 \times 10^6 / (2\pi) = 1.1 \times 10^6$ N/m and $C_z = 6.2 \times 10^6 / (2\pi) = 9.9 \times 10^5$ N/m

3.4 Tool Wear and Process Damping Mechanism

It is well known that the tool wear changes the cutting edge geometry and flank contact with the wavy surface finish [48]. A series of dynamic cutting tests have been conducted on stainless steel by following the same procedure proposed in this chapter. Since stainless steel produces high heat, the tools were worn quickly. The dynamic cutting coefficients were identified using both sharp and worn tools. The corresponding stability limits are shown in Figure 3-9. The flank wear was about $80\mu\text{m}$ measured under a

microscope. The stability with process damping moved from 1000 rev/min to 3000 rev/min, and all the unstable cutting tests with sharp tool were observed to become stable when tested with the worn tool. Chatter occurred only at 3500 rev/min and 1.5 mm depth of cut with the worn tool.

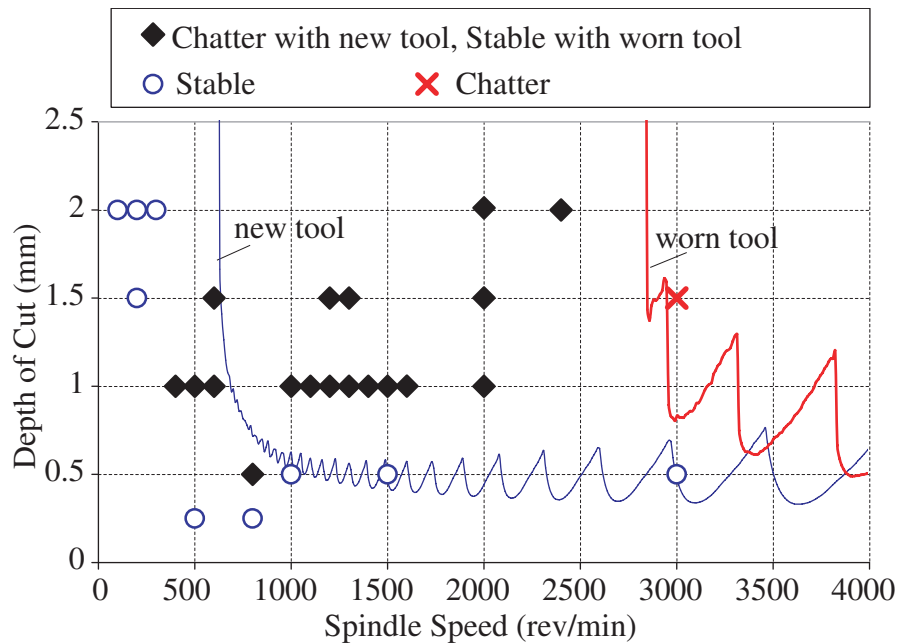


Figure 3-9: The effect of tool wear on the stability lobes with experimental results. Material: Stainless steel SS304 shaft with 35 mm diameter. Feed rate: 0.050mm/rev. Structural parameters: $m = 1.742\text{Kg}$, $C = 176.8\text{N/m/s}$, $K = 7.92\text{MN/m}$. Cutting force Coefficients: $K_z = 2068\text{MPa}$, $K_y = 2585\text{MPa}$ New tool : $C_y = 1.2\text{MN/m}$ Worn tool with 0.080 mm flank wear $C_y = 4.9\text{MN/m}$

The process damping coefficient during cutting stainless steel (SS304) is measured with dynamic cutting tests while tool wear length was measured under instrumented microscope and the results are shown in Figure 3-10. There appears to be a linear relationship between the process damping parameter (C_y) and square of wear land (L_w^2). Such a relationship is in agreement with the theory suggested by Wallace and Andrew [48], Wu [49] and Chio and Liang [10].

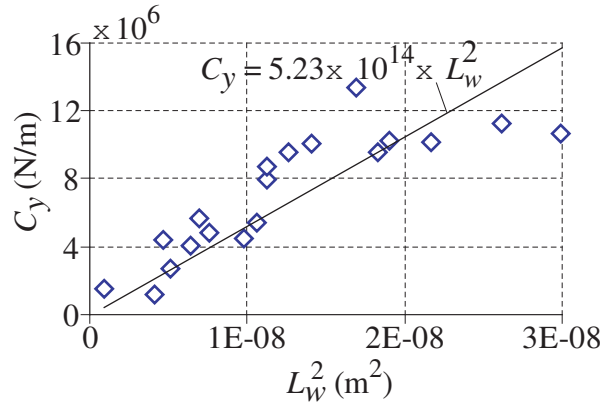


Figure 3-10: The relationship between the process damping coefficient and square of wear length

3.5 Chatter Stability Diagrams

Two chatter stability diagrams generated with only regenerative term and with added velocity term are shown in Figure 3-11. The stability of the characteristic equation is investigated by Nyquist stability criterion ([28],[26],[31]).

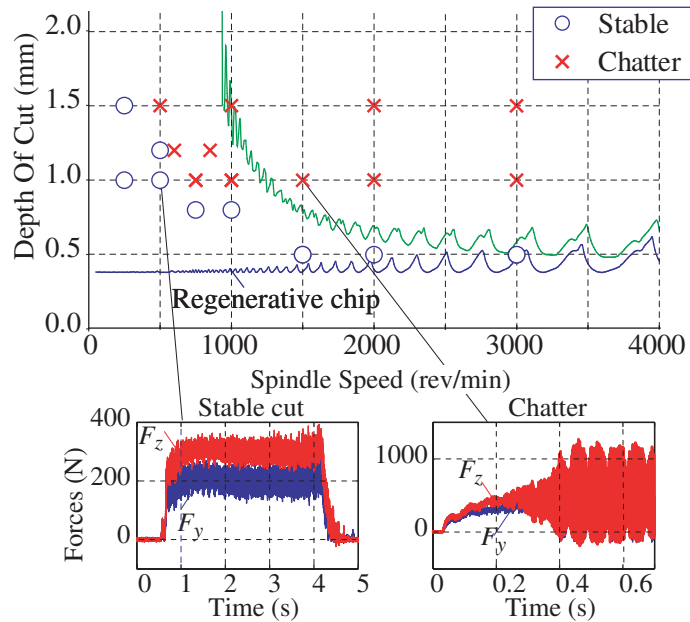


Figure 3-11: Stability lobes with and without process damping terms. Measured cutting forces during stable ($n=500$ rev/min, $a=1$ mm) and unstable ($n=1500$ rev/min, $a=1$ mm) cutting tests. Material: AISI1045 with a diameter of 35 mm. $\omega_n = 450.7$ Hz $K = 6.48 \times 10^6$ N/m, $c = 145$ N/(m/s), See Figure 3-8 for material properties.

The classical chatter stability law with regenerative chip thickness, $[y(t) - y(t - \tau)]$, is not velocity dependent at the low speeds where it gives a constant critical depth of cut of 0.4mm.

When the velocity, i.e. process damping term $(-C_y \dot{y} / V_c)$, is included, the stability starts increasing at speeds under 2000 (rev/min). A number of similar identification and chatter stability tests have been conducted on different materials. The process becomes infinitely stable with process damping term as the speed approaches to zero.

3.6 Conclusion

Accurate prediction of chatter stability at low speeds is dependent on the identification of dynamic cutting force coefficients. The dynamic cutting force coefficients are sensitive to the work material properties, cutting edge preparation, tool wear and cutting speed, contact mechanics between the wavy surface finish and flank face, as well as the time-varying shearing process.

This chapter presented a new dynamic cutting force model whose coefficients are identified from controlled oscillation tests with the aid of a fast tool servo. When the oscillating frequency and spindle speed are synchronized to achieve in-phase inner and outer modulations, the regenerative effect is eliminated and the process damping coefficients can be identified. The phase between inner and outer waves can be introduced with the proposed set up, and the influence of shear plane length and effective rake angle can also be investigated. The proposed method is experimentally illustrated in predicting the influence of wave length and tool wear on the chatter stability of metal cutting operations at low speeds. The proposed method will be extended to 3D turning operations and milling operations in subsequent chapters.

Chapter 4: Stability of General Turning with Process

Damping

4.1 Introduction

In this chapter a new stability prediction method for three-dimensional turning processes is introduced. It starts with an introduction of a cutting force model for three dimensional cutting. This cutting force model is used in a time domain simulation that compares the behaviours of stable and unstable systems. Two Analytical stability prediction methods are presented. First model approximates the 3D cutting process as cutting with a straight cutting edge. Second model starts with calculation of differentials of cutting forces with respect to the displacements in feed and depth of cut directions and it continues with development of a process damping matrix. At the end of the chapter, stability predictions are compared against experiments with different feed rates, tool nose radii and spindle speeds.

4.2 Cutting Force Nonlinearity

Figure 4-1 presents the cutting force measurements in the directions of depth of cut (x), feed (y) and cutting speed (z) as compared to the predictions of a model that assumes such forces to be proportional to the chip area ($F_x = K_x \cdot A$, $F_y = K_y \cdot A, \dots$). The measurements are results of cutting tests at cutting speed of $V_c = 270\text{m/min}$ with tools with different nose radii ($r_e = 0.4 \dots 2.4\text{mm}$) at various feeds ($c = 0.025 \dots 0.200\text{mm/rev}$)

and depth of cuts ($a = 0.5 \dots 2 \text{ mm}$). Sandvik CNMA1204 KR 3205 series coated inserts on DLCNL holder with -6° rake, -6° inclination, and $\kappa_r = 95^\circ$ approach angle are used for this test. The workpiece is AISI 1045 steel with Brinell hardness of 210.

The prediction of forces in x and y directions have considerable errors as seen in Figure 4-1. This demonstrates the need for an improved cutting force prediction method which considers parameters other than chip area.

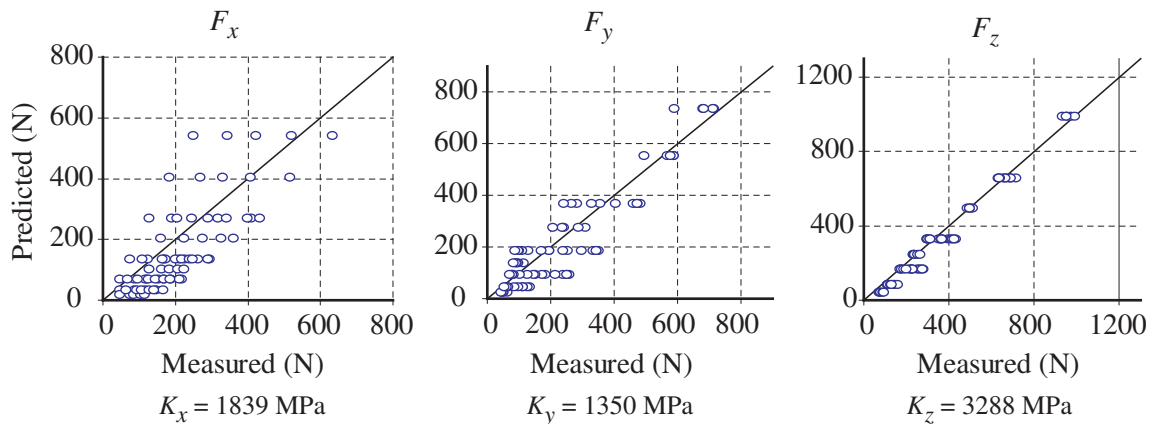


Figure 4-1: Comparison of force measurements and predictions assuming forces proportional to the uncut chip area. See section 4.2 for tool and material properties.

4.2.1 Cutting force prediction based on chip flow direction

Figure 4-2 shows a three-dimensional cutting operation with a tool with a round nose. The friction forces on the rake face are assumed to be in the same direction as chip flow. A better force prediction is expected if the cutting force model includes the effect of chip flow direction.

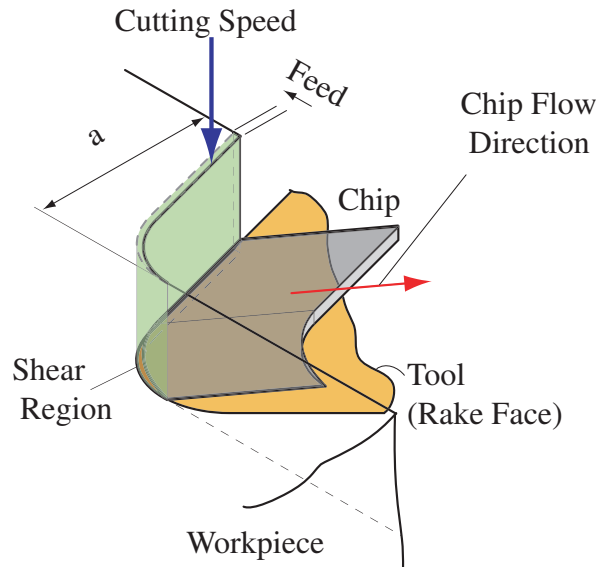


Figure 4-2: Three-dimensional cutting with a tool with a round nose

Notable works in chip-flow direction prediction were conducted by Colwell [12], Usui et. Al, [47], Hu, Matthew and Oxley [19] and a comprehensive review was also presented by Jawahir [22]. Colwell [12] proposed that the chip flow is normal to the chord which connects two ends of the cutting edge engaged with the cut, and makes an angle θ with the feed direction as shown in Figure 4-3.

where elements are independent of chip shape and are identified experimentally. However, these coefficients are dependent on cutting speed for some materials (such as AISI1045 steel).

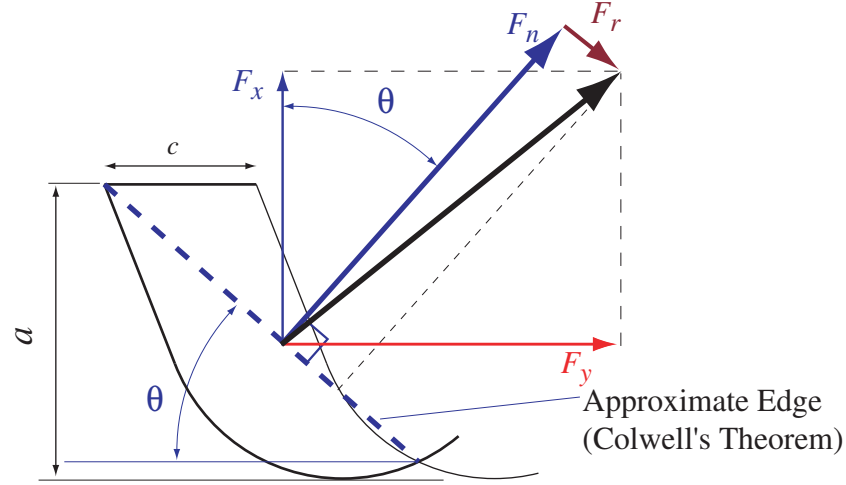


Figure 4-4: Normal force (F_n) and side force (F_r) with respect to approximate edge

The cutting forces in the direction of depth of cut (x), feed (y) and velocity (z) are evaluated from the chord angle (θ) using the rotation matrix $[C_{nm}]$ defined below:

$$\{F_m\} = [C_{nm}]^T \{F_n \ F_r \ F_z\}^T = [C_{nm}]^T [K_c] \{1 \ L \ A\}^T$$

$$[C_{nm}] = \begin{bmatrix} \cos \theta & \sin \theta & 0 \\ -\sin \theta & \cos \theta & 0 \\ 0 & 0 & 1 \end{bmatrix} \quad (4-3)$$

where $\{F_m\} = \{F_x \ F_y \ F_z\}^T$ are the cutting force components expressed in measurement coordinate system. For the cutting tests described in Figure 4-1, the cutting coefficients are obtained from the least squares method:

$$K_{n0} = 3, K_{r0} = -24, K_{t0} = -1[\text{N}], \quad K_{nL} = 83, K_{rL} = 26, K_{zL} = 44[\text{N/mm}] \quad \text{and}$$

$K_{nA} = 1544$, $K_{rA} = -124$, $K_{tA} = 2881$ [MPa]. The predictions of the fitted model are close to the experiment measurements as shown in Figure 4-5.

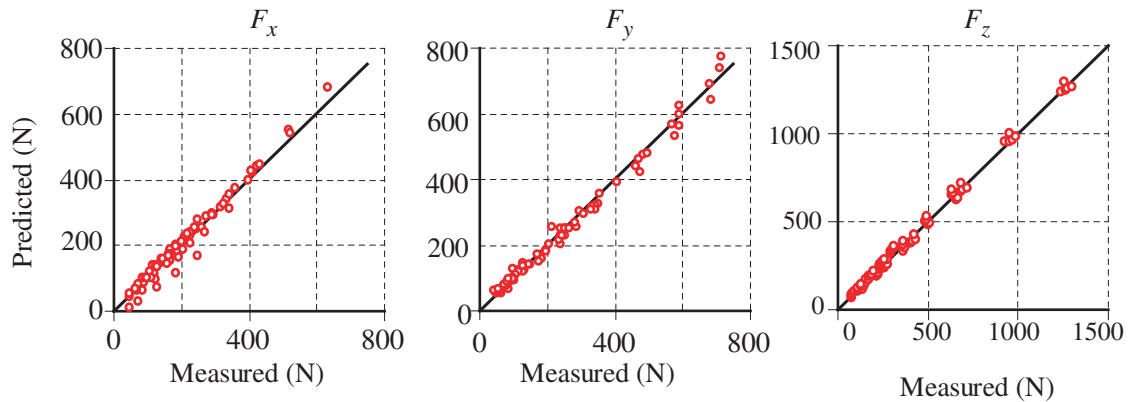


Figure 4-5: Prediction considering chip flow direction as suggested by Colwell [12], see Figure 4-1 for tool and material properties.

4.2.2 Cutting force prediction based on variable approach angle

An alternative force prediction method was employed by Ozlu and Budak [33] in development of their chatter stability prediction algorithm. In that method, the emphasis is given to the approach angle of the cutting edge along the nose radius area, the chip area is divided into infinitesimal sections parallel to the feed direction. The cutting force in each section is assumed to be proportional to the area of that section, and its direction is determined by the approach angle of the cutting edge at that section as seen in Figure 4-6. The total cutting force is obtained through the summation of cutting forces in these sections. The original method presented in Ozlu and Budak's paper requires a numerical integration over the cutting edge curve; however, analytical integration of the forces is also possible when the tool nose is a simple circular curve.

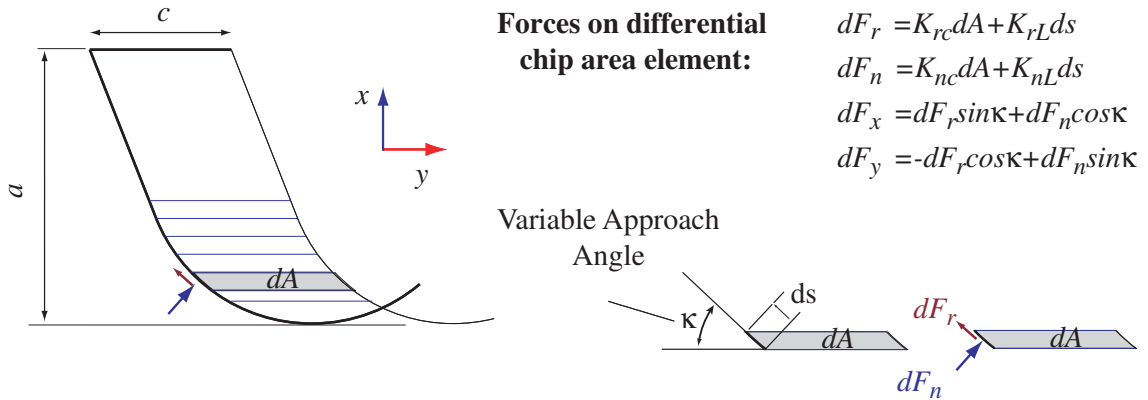


Figure 4-6: Variable approach angle method

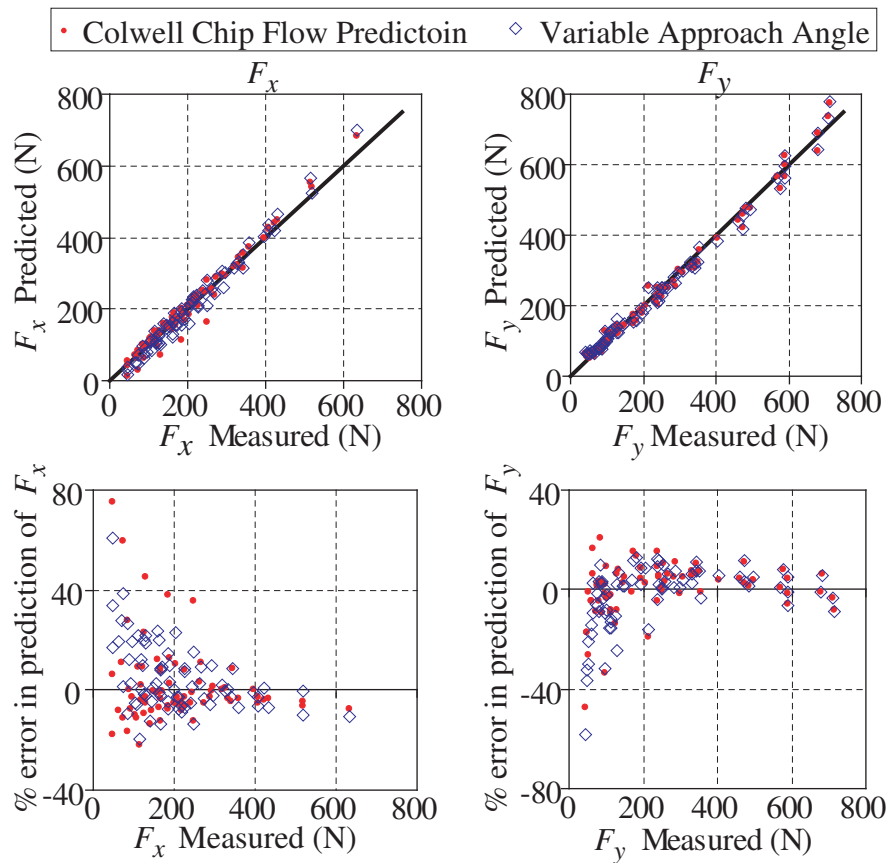


Figure 4-7: Comparison of force prediction method based on Colwell's chip flow direction and variable approach angle method

The force predictions of variable approach method are compared to the force predictions of Colwell's chip flow direction in Figure 4-7. These force predictions have similar

relative error levels. For the rest of the thesis, the force model based on Colwell's chip flow direction is adopted.

4.3 Time Domain Simulation of Turning Process

It is possible to simulate the machining process with a flexible tool/workpiece by using numerical solution of delay differential equations of machining. Time domain simulation method is schematically presented in Figure 4-8. The differentials of the state vector are calculated based on the structural accelerations due to cutting forces. Cutting forces are dependent on the instantaneous geometry of the chip cross section. If the force prediction method based on chip flow direction as presented in Section 4.2.1 is used, it will be necessary to calculate chip area A , approximate edge length L and its angle θ to calculate cutting forces.

Chip area parameters (A , L and θ) are calculated analytically for arbitrary state vector in time domain method.

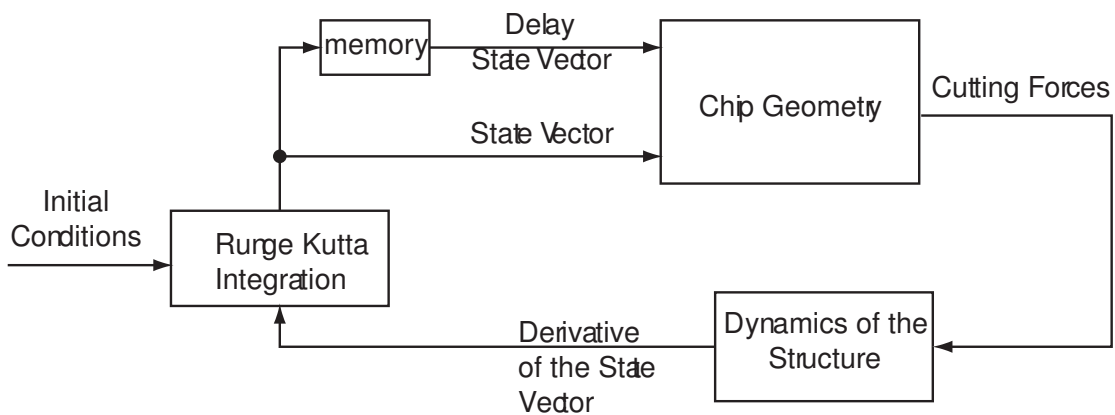


Figure 4-8: Schematic of time domain Simulation

Chip geometry changes due to the movements of the tool in present and previous cuts. (x, y) and (x_{τ}, y_{τ}) are the displacements in the directions of depth of cut and feed during the present and previous cut, respectively.

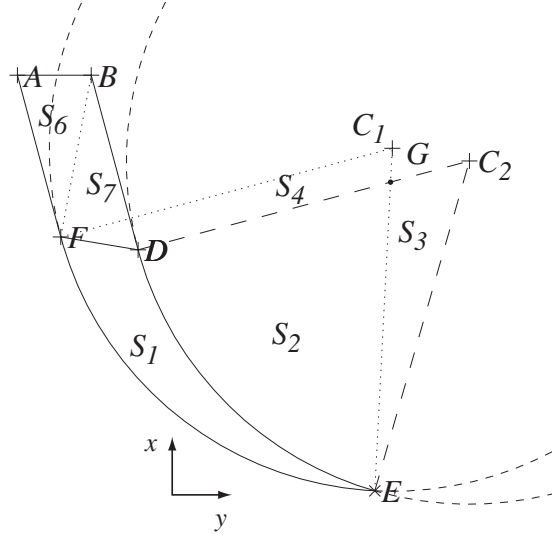


Figure 4-9: Chip area considering dynamic movements of tool in present and previous cuts

The center of the tool nose circle, $C_1 = \{C_{1x}, C_{1y}, 0\}^T$, is selected in a way that without dynamic vibrations, $C_{1x} = r_\epsilon, C_{1y} = 0$, and the center of the tool nose in the previous cut is at $C_2 = \{C_{2x}, C_{2y}, 0\}^T$, $C_{2x} = r_\epsilon, C_{2y} = c$ while with dynamic vibrations, the center of the cutting edge will change as (see Figure 4-9):

$$\begin{aligned} C_{1x} &= x + r_\epsilon, C_{1y} = y \\ C_{2x} &= x_\tau + r_\epsilon, C_{2y} = y_\tau \end{aligned} \quad (4-4)$$

The point $E = \{E_x, E_y, 0\}^T$ is the intersection of the round nose curves in the present and previous cuts. This point is obtained by letting $\overline{C_1E} = \overline{C_2E} = r_\epsilon$ and defining β as $\sphericalangle C_1EC_2$; its coordinates are obtained as:

$$\begin{aligned}
 E_{1x} &= C_{1x} - r_{\epsilon} \sin \beta \\
 E_{2x} &= C_{1y} + r_{\epsilon} \cos \beta \\
 (\beta &= \arccos\left(\frac{C_1 C_2}{2r_{\epsilon}}\right))
 \end{aligned} \tag{4-5}$$

The chip geometry is different if the straight part of the tool is engaged in cut (referred as case 1 below), or the cutting is only on the round nose region (case 2). Analytical relationships for calculating cutting forces are presented separately for each case.

Case 1: $a > r_{\epsilon}(1 - \cos \kappa_r)$

If the depth of cut is larger than the round nose region: ($a > r_{\epsilon}(1 - \cos \kappa_r)$), Points

$F = \{F_x \quad F_y \quad 0\}^T$ and $D = \{D_x \quad D_y \quad 0\}^T$ are defined as the points of tangency of

straight cutting edge on the nose circle in the present and previous cut:

$$\begin{aligned}
 F_x &= C_{1x} - r_{\epsilon} \cos \kappa_r, F_y = C_{1y} - r_{\epsilon} \sin \kappa_r \\
 D_x &= C_{2x} - r_{\epsilon} \cos \kappa_r, D_y = C_{2y} - r_{\epsilon} \sin \kappa_r
 \end{aligned} \tag{4-6}$$

and

$$\begin{aligned}
 A_x &= a, A_y = F_y - \frac{a - F_x}{\tan \kappa_r} \\
 B_x &= a, B_y = D_y - \frac{a - D_x}{\tan \kappa_r}
 \end{aligned} \tag{4-7}$$

Point G is defined as the intersection of the straight lines C_2D and C_1E . The coordinates of G are calculated using Cramer's rule.

The angles θ_1 and θ_2 are used for the calculation of the area between the arcs \widehat{EF} and C_1 and \widehat{ED} and C_2 respectively, they are calculated as:

$$\theta_1 = \angle EC_1F = 2 \arcsin\left(\frac{\overline{EF}}{2r_\varepsilon}\right) \quad \theta_2 = \angle EC_2D = 2 \arcsin\left(\frac{\overline{ED}}{2r_\varepsilon}\right) \quad (4-8)$$

S_1 is the area between arcs \widehat{ED} , \widehat{EF} and line FD and it is calculated using the following relationships:

$$\begin{aligned} S_2 + S_3 &= \frac{r_\varepsilon^2}{2} \theta_2 \\ S_2 + S_1 + S_4 &= \frac{r_\varepsilon^2}{2} \theta_1 \\ \Rightarrow S_1 &= \frac{r_\varepsilon^2}{2} (\theta_1 - \theta_2) + S_3 - S_4 \\ S_3 &= \frac{\hat{k}}{2} \cdot (\overline{EG} \times \overline{EC}) \\ S_4 &= \frac{\hat{k}}{2} \cdot (\overline{C_1G} \times \overline{C_1F} + \overline{DF} \times \overline{DG}) \end{aligned} \quad (4-9)$$

Therefore S_1 becomes:

$$S_1 = \frac{r_\varepsilon^2}{2} (\theta_1 - \theta_2) + \frac{\hat{k}}{2} \cdot (\overline{EG} \times \overline{EC} - \overline{C_1G} \times \overline{C_1F} - \overline{DF} \times \overline{DG}) \quad (4-10)$$

The area of tetragon ABFD is calculated as:

$$S_{ABFD} = \frac{\hat{k}}{2} \cdot (\overline{DF} \times \overline{DB} + \overline{AB} \times \overline{AF}) \quad (4-11)$$

and

$$Area = S_{ABFD} + S_1 \quad (4-12)$$

The Approximate chord length is $L = \overline{AE}$, and the Colwell's angle is obtained:

$$\theta = \theta_{Colwell} = \arctan\left(\frac{A_x - E_x}{E_y - A_y}\right) \left(\frac{\pi}{2} - \theta\right) \quad (4-13)$$

$$\theta_1 = \angle EC_1F = 2 \arcsin \left(\frac{\overline{EF}}{2r_\varepsilon} \right) \quad (4-16)$$

$$\begin{aligned} \text{Area} &= S_1 \\ S_1 &= \frac{r_\varepsilon^2}{2} (\theta_1 - \theta_2) + \frac{\hat{k}}{2} \cdot (\overline{EG} \times \overline{EC} - \overline{C_1G} \times \overline{C_1F} - \overline{DF} \times \overline{DG}) \end{aligned} \quad (4-17)$$

Approximating chord length as $L = \overline{FE}$ and the Colwell's angle becomes:

$$\theta = \theta_{Colwell} = \arctan \left(\frac{F_x - E_x}{E_y - F_y} \right) \quad (4-18)$$

4.3.1 State vector

The structure is assumed to have coupled dynamics in all three directions, therefore, the displacements of x and y are the result of the response of the coupled modes to the cutting forces in all directions, as in Laplace domain:

$$x = \frac{F_x}{K_{xx} \left(\frac{s^2}{\omega_{nxx}^2} + \frac{2\zeta_{xx}s}{\omega_{nxx}} + 1 \right)} + \frac{F_y}{K_{xy} \left(\frac{s^2}{\omega_{nxy}^2} + \frac{2\zeta_{xy}s}{\omega_{nxy}} + 1 \right)} + \frac{F_z}{K_{zx} \left(\frac{s^2}{\omega_{nzx}^2} + \frac{2\zeta_{zx}s}{\omega_{nzx}} + 1 \right)} \quad (4-19)$$

A similar relationship holds for y . To model the dynamics of the system properly, three independent dynamic variables (x_1 , x_2 and x_3) are introduced:

$$\begin{aligned}
 x &= x_1 + x_2 + x_3 \\
 x_1 &= \frac{F_x}{K_{xx} \left(\frac{s^2}{\omega_{nxx}^2} + \frac{2\zeta_{xx}s}{\omega_{nxx}} + 1 \right)}, \\
 x_2 &= \frac{F_y}{K_{xy} \left(\frac{s^2}{\omega_{nxy}^2} + \frac{2\zeta_{xy}s}{\omega_{nxy}} + 1 \right)} \\
 x_3 &= \frac{F_z}{K_{zx} \left(\frac{s^2}{\omega_{nzx}^2} + \frac{2\zeta_{zx}s}{\omega_{nzx}} + 1 \right)}
 \end{aligned} \tag{4-20}$$

The state vector includes these three variables and their first time derivatives and similar components for the feed (y) direction; therefore, the state vector's size is 12×1 :

$$X = \{x_1, \dot{x}_1, x_2, \dot{x}_2, x_3, \dot{x}_3, y_1, \dot{y}_1, y_2, \dot{y}_2, y_3, \dot{y}_3\}^T \tag{4-21}$$

The state vector considers only one mode for each direct or coupled mode. While there would be dynamic displacements in the cutting speed direction (z), displacements in this direction do not affect the chip area and cutting forces and are not included in simulation. Additional natural modes are possible to model only with a larger state vector.

4.3.2 Results of the time domain simulation

A time domain simulation based on suggested model is performed. A non-zero initial history is selected for the delay differential equation. For a stable cutting condition, the nonzero initial condition reaches a stable steady state, while for an unstable system, it leads to vibrations with growing amplitude as shown in Figure 4-11. Time domain simulations are computationally costly compared to analytical stability predictions; therefore, two analytical stability prediction methods are developed and will be presented in following sections.

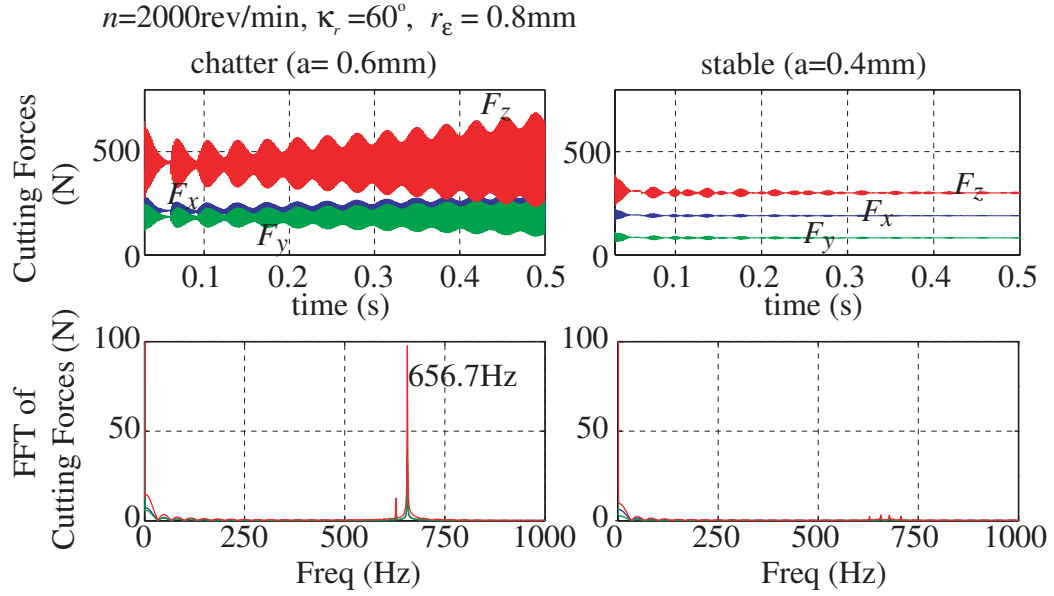


Figure 4-11: Results of time domain simulation ($\zeta_k = 0.05, \omega_{nk} = 600\text{Hz}$); **The modal stiffness values are given as** $k_{xx} = 40$, $k_{yy} = 100$, $k_{zz} = 25$, $k_{xy} = k_{yx} = 70$, $k_{zx} = k_{xz} = 25$, $k_{yz} = k_{zy} = 100$ [$\text{N}/\mu\text{m}$], **and cutting coefficients:** $K_{n0} = 39$, $K_{r0} = -146$, $K_{t0} = -3$ [N]; $K_{nl} = 75000$, $K_{rL} = 90000$, $K_{tL} = 73000$ [N/m], $K_{nA} = 1065$, $K_{rA} = 647$, $K_{tA} = 2516$ [MPa]

4.4 Analytical Model I: Regenerative Chip Model

The turning tool is assumed to cut along the equivalent chord and the cutting forces are assumed to have the following linear relationship with the equivalent chip thickness:

$$\{F_n \quad F_r \quad F_z\}^T = \{K_{nA} \quad K_{rA} \quad K_{tA}\}^T L h_c \quad (4-22)$$

where L is the equivalent chip width or chord length, and h_c is the equivalent chip thickness measured perpendicular to the chord (Figure 4-4) as suggested by Colwell [12].

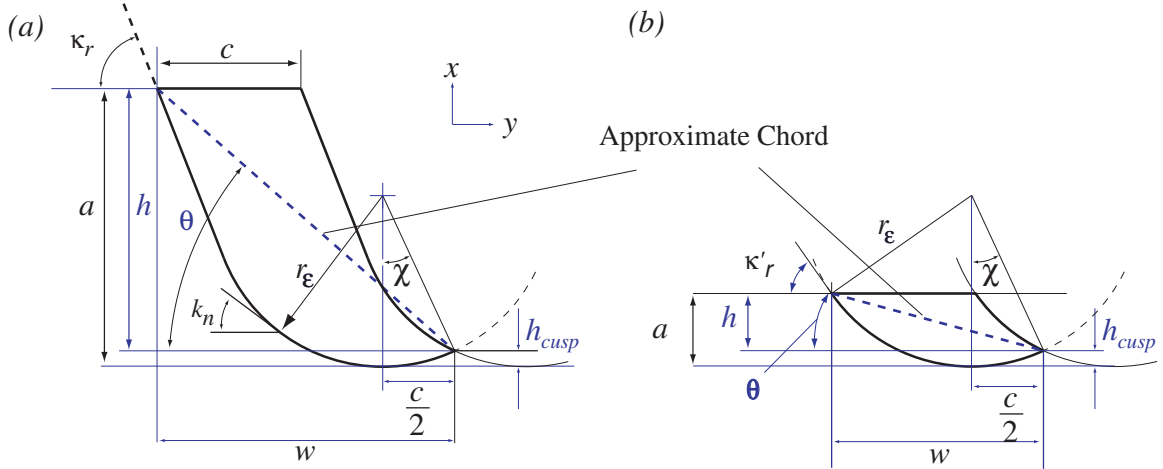


Figure 4-12: Parameters of chip area (a): $a > r_\epsilon (1 - \cos \kappa_r)$ (b) $a \leq r_\epsilon (1 - \cos \kappa_r)$

The chord angle (θ) and length (L) depend on the depth of cut (a), feed (c), nose radius (r_ϵ) and approach angle (κ_r), shown in Figure 4-12 and they are calculated as such:

$$\left. \begin{aligned}
 h_{cusp} &= r_\epsilon - \sqrt{r_\epsilon^2 - \left(\frac{c}{2}\right)^2} = r_\epsilon \left(1 - \sqrt{1 - \left(\frac{c}{2r_\epsilon}\right)^2} \right) \stackrel{\frac{c}{r_\epsilon} \ll 1}{\approx} r_\epsilon \left\{ 1 - \left[1 - \frac{1}{2} \left(\frac{c}{2r_\epsilon}\right)^2 \right] \right\} = \frac{c^2}{8r_\epsilon} \\
 h &= a - h_{cusp} = a - \frac{c^2}{8r_\epsilon} \\
 w &= \begin{cases} \frac{c}{2} + \frac{a - r_\epsilon (1 - \cos \kappa_r)}{\tan \kappa_r} + r_\epsilon \sin \kappa_r & a > r_\epsilon (1 - \cos \kappa_r) \\ \frac{c}{2} + \sqrt{r_\epsilon^2 - (r_\epsilon - a)^2} & a \leq r_\epsilon (1 - \cos \kappa_r) \end{cases} \\
 A = c a, \quad \theta = \arctan(w / h), \quad L = \sqrt{h^2 + w^2}
 \end{aligned} \right\} (4-23)$$

where A is the chip area and h and w are the projections of the approximate chord in the depth of cut and feed directions respectively. The cutting forces are projected in three Cartesian directions where the structural dynamics of the machine are defined:

$$\{F_x \quad F_y \quad F_z\}^T = [C_{nm}]^T \{F_n \quad F_r \quad F_t\}^T \quad (4-24)$$

By projecting the vibrations perpendicular to the chord, the equivalent regenerative chip thickness can be approximated as:

$$h_c = c \sin \theta - \{ [x(t) \cos \theta + y(t) \sin \theta] - [x(t - \tau) \cos \theta + y(t - \tau) \sin \theta] \} \quad (4-25)$$

where (τ) is the spindle rotation period. The vibrations in the direction of cutting speed (z) do not affect the chip thickness. The time independent, static chip load ($c \sin \theta$) is dropped from the equation since it does not affect the stability.

The force-displacement relationship in the structure of the machine, tool and the workpiece is also assumed linear:

$$\begin{Bmatrix} x(s) \\ y(s) \\ z(s) \end{Bmatrix} = \underbrace{\begin{bmatrix} \phi_{xx} & \phi_{xy} & \phi_{xz} \\ & \phi_{yy} & \phi_{yz} \\ sym & & \phi_{zz} \end{bmatrix}}_{\mathbf{\Phi}(s)} \underbrace{\begin{Bmatrix} F_x \\ F_y \\ F_z \end{Bmatrix}}_{\mathbf{F}_m} \quad (4-26)$$

Elements of $\mathbf{\Phi}(s)$ matrix are transfer functions in the Laplace domain, with $K_{pq,j}$, $\zeta_{pq,j}$ and $\omega_{pq,j}$ as stiffness, damping ratio and natural frequency in mode j where there are n_j modes in the structure:

$$\mathbf{\Phi}_{pq}(s) = \sum_{j=1}^{n_j} \frac{1}{K_{pq,j} (1 + 2\zeta_{pq,j} s / \omega_{pq,j} + s^2 / \omega_{pq,j}^2)} \quad p, q \in (x, y, z) \quad (4-27)$$

From (4-25) the dynamics of the regenerative chip is reduced to:

$$\begin{aligned}
 h_c(s) &= -(1-e^{-s\tau})\{\cos\theta \quad \sin\theta \quad 0\}\{x(s) \quad y(s) \quad z(s)\}^T \\
 h_c(s) &= -(1-e^{-s\tau})\{\cos\theta \quad \sin\theta \quad 0\}[\Phi(s)]\{F_m\} \\
 h_c(s) &= -(1-e^{-s\tau})\underbrace{\{\cos\theta \quad \sin\theta \quad 0\}[\Phi(s)][C_{nm}]^T\{K_{nA} \quad K_{rA} \quad K_{tA}\}^T}_{\Phi_0(s)} Lh_c(s) \quad (4-28)
 \end{aligned}$$

$$\begin{aligned}
 h_c(s) &= -(1-e^{-s\tau})\Phi_0(s)Lh_c(s) \\
 \therefore h_c(s) &\left[1 + (1-e^{-s\tau})L\Phi_0(s)\right] = 0
 \end{aligned}$$

The model in Eq. (4-28) gives an approximate single variable prediction of dynamic cutting forces and characteristic equation is obtained as:

$$1 + (1-e^{-s\tau})L\Phi_0(s) = 0 \quad (4-29)$$

The directional factors for oriented transfer function Φ_0 are derived as:

$$\begin{aligned}
 \Phi_0(s) &= \{\cos\theta \quad \sin\theta \quad 0\}[\Phi(s)][C_{nm}]^T\{K_{nA} \quad K_{rA} \quad K_{tA}\}^T \\
 &= \sum_{p,q} d_{pq} \Phi_{pq}(s), \quad (p,q) \in (x,y,z) \\
 \left. \begin{aligned}
 d_{xx} &= K_{nA} \cos^2\theta - 0.5K_{rA} \sin 2\theta, \quad d_{xy} = K_{rA} \cos^2\theta + 0.5K_{nA} \sin 2\theta, \\
 d_{xz} &= K_{tA} \cos\theta, \quad d_{yx} = -K_{rA} \sin^2\theta + 0.5K_{nA} \sin 2\theta, \\
 d_{yy} &= 0.5K_{rA} \sin 2\theta + K_{nA} \sin^2\theta, \\
 d_{yz} &= K_{tA} \sin\theta, \quad d_{zx} = d_{zy} = d_{zz} = 0
 \end{aligned} \right\} \quad (4-30)
 \end{aligned}$$

For a known depth of cut, feed, nose radius, the effective transfer function Φ_0 is calculated and system's stability is investigated using Nyquist stability criterion for the characteristic equation. Unlike simple orthogonal cutting, it is not possible to calculate the threshold of instability directly because Φ_0 varies as a function of the depth of cut.

4.5 Analytical Model II: Regenerative Chip Area and Chord Model

Cutting force changes due to displacements of the tool with respect to the workpiece in feed and depth of cut directions. In addition, the process will have additional damping when the cutting speed is low [48]. The dynamic cutting force vector is proposed to be modeled as:

$$\mathbf{F}_m(t) = [\mathbf{J}]Q(t) + [\mathbf{J}_\tau]Q(t - \tau) + [\mathbf{J}_v]\dot{Q}(t) \quad (4-31)$$

where the regenerative delay τ is equal to the spindle period, and the dynamic force $\mathbf{F}_m(t)$, displacement $Q(t)$ and velocity $\dot{Q}(t)$ vectors are:

$$\begin{aligned} \mathbf{F}_m(t) &= \{F_x(t) \quad F_y(t) \quad F_z(t)\}^T \\ Q(t) &= \{x(t) \quad y(t) \quad z(t)\}^T, \quad Q(t - \tau) = \{x(t - \tau) \quad y(t - \tau) \quad z(t - \tau)\}^T \\ \dot{Q}(t) &= \left\{ \frac{dx(t)}{dt} \quad \frac{dy(t)}{dt} \quad \frac{dz(t)}{dt} \right\}^T \end{aligned} \quad (4-32)$$

The gain matrices reflect the changes in the cutting forces due to the structural displacements and vibration velocities,

$$\begin{aligned} [\mathbf{J}] &= \begin{bmatrix} \frac{\partial \mathbf{F}_m}{\partial x} & \frac{\partial \mathbf{F}_m}{\partial y} & \frac{\partial \mathbf{F}_m}{\partial z} \end{bmatrix}, \quad [\mathbf{J}_\tau] = \begin{bmatrix} \frac{\partial \mathbf{F}_m}{\partial x_\tau} & \frac{\partial \mathbf{F}_m}{\partial y_\tau} & \frac{\partial \mathbf{F}_m}{\partial z_\tau} \end{bmatrix}, \\ [\mathbf{J}_v] &= \begin{bmatrix} \frac{\partial \mathbf{F}_m}{\partial \dot{x}} & \frac{\partial \mathbf{F}_m}{\partial \dot{y}} & \frac{\partial \mathbf{F}_m}{\partial \dot{z}} \end{bmatrix} \end{aligned} \quad (4-33)$$

where \mathbf{J} and \mathbf{J}_τ are the direct and delay process gain matrices respectively. \mathbf{J}_v is the velocity-dependent process damping gain matrix. The dynamics of the system is transformed into the Laplace domain as:

$$\begin{aligned} \{\mathbf{F}_m(s)\} &= [\mathbf{J} + \mathbf{J}_\tau e^{-s\tau} + s\mathbf{J}_v] \{Q(s)\} = [\mathbf{J} + \mathbf{J}_\tau e^{-s\tau} + s\mathbf{J}_v] [\Phi(s)] \{\mathbf{F}_m(s)\} \\ \{\mathbf{0}\}_{3 \times 1} &= ([\mathbf{I}]_{3 \times 3} - [\mathbf{J} + \mathbf{J}_\tau e^{-s\tau} + s\mathbf{J}_v]) [\Phi(s)] \{\mathbf{F}_m(s)\} \end{aligned} \quad (4-34)$$

Since the process gain matrices ($\mathbf{J}, \mathbf{J}_\tau, \mathbf{J}_v$) and delay (τ) are dependent on cutting conditions such as depth of cut, speed and feed, the direct stability lobes of the turning system cannot be identified by the matrix eigenvalue method of Altintas and Budak [3]. Instead, the critical stability limit is checked whether the system is stable or unstable at a given cutting condition. From Eq. (4-34) the characteristic equation is represented as:

$$\det\left(\left[\mathbf{I}\right]_{3 \times 3} - \left(\mathbf{J} + \mathbf{J}_\tau e^{-s\tau} + s\mathbf{J}_v\right) [\Phi(s)]\right) = 0 \quad (4-35)$$

Presence of unstable poles of this characteristic equation is investigated using Nyquist stability criterion in the frequency domain ($s \rightarrow j\omega$) [28],[31]; Details of application of Nyquist stability criterion are discussed in Appendix A. The stability of the turning system at specified cutting conditions is highly dependent on the modeling of process gain matrices which are derived in the following section.

4.5.1 Modeling of dynamic cutting force gains in turning

The process gain matrices ($\mathbf{J}, \mathbf{J}_\tau, \mathbf{J}_v$) are modeled by evaluating the partial derivatives of the cutting force with respect to the variables as indicated in Eq.(4-33). Considering the force model introduced in Eq.(4-3):

$$\{\mathbf{F}_m\} = [\mathbf{C}_{nm}(\theta)]^T \{F_n \quad F_r \quad F_z\}^T = [\mathbf{C}_{nm}(\theta)]^T [\mathbf{K}_c] \{1 \quad L \quad A\}^T$$

A , L and θ are not affected by displacements in cutting speed direction, therefore:

$$\frac{\partial \mathbf{F}_m}{\partial z} = \frac{\partial \mathbf{F}_m}{\partial z_\tau} = \mathbf{0} \quad (4-36)$$

Consequently, the third columns of \mathbf{J} and \mathbf{J}_τ are zero. The first and second columns of these matrices are obtained by differentiation with respect to x, x_τ, y and y_τ using a general variable u ($u = x, y, x_\tau, y_\tau$)

$$\begin{aligned}
 \{\mathbf{F}_m\} &= [\mathbf{C}_{nm}(\theta)]^T [\mathbf{K}_c] \{1 \quad L \quad A\}^T \\
 \Rightarrow \\
 \frac{\partial \mathbf{F}_m}{\partial u} &= \left[\frac{\partial \mathbf{C}_{nm}(\theta)}{\partial \theta} \right]^T [\mathbf{K}_c] \{1 \quad L \quad A\}^T \frac{\partial \theta}{\partial u} \\
 &\quad + [\mathbf{C}_{nm}(\theta)]^T [\mathbf{K}_c] \left\{ 0 \quad \frac{\partial L}{\partial u} \quad \frac{\partial A}{\partial u} \right\}^T
 \end{aligned} \tag{4-37}$$

The differentiation of transposed rotation matrix $\mathbf{C}_{nm}(\theta)$ is obtained from (4-3) as:

$$\frac{\partial [\mathbf{C}_{nm}]^T}{\partial \theta} = \begin{bmatrix} -\sin \theta & -\cos \theta & 0 \\ \cos \theta & -\sin \theta & 0 \\ 0 & 0 & 0 \end{bmatrix} \tag{4-38}$$

θ and L are functions of chip area width w and height h as described in (4-23):

$$\begin{aligned}
 \theta &= \arctan(h/w) \\
 \Rightarrow \frac{\partial \theta}{\partial u} &= \frac{1}{1 + \frac{h^2}{w^2}} \cdot \frac{w \frac{\partial h}{\partial u} - h \frac{\partial w}{\partial u}}{w^2} \\
 \therefore \frac{\partial \theta}{\partial u} &= \frac{1}{L} \left(\cos \theta \frac{\partial h}{\partial u} - \sin \theta \frac{\partial w}{\partial u} \right)
 \end{aligned}$$

$$L = \sqrt{h^2 + w^2} \tag{4-39}$$

$$\begin{aligned}
 \Rightarrow \frac{\partial L}{\partial u} &= \frac{2w \frac{\partial w}{\partial u} + 2h \frac{\partial h}{\partial u}}{2\sqrt{h^2 + w^2}} \\
 \Rightarrow \frac{\partial L}{\partial x} &= \frac{w}{L} \frac{\partial w}{\partial u} + \frac{h}{L} \frac{\partial h}{\partial u} \\
 \therefore \frac{\partial L}{\partial u} &= \frac{\partial w}{\partial u} \cos \theta + \frac{\partial h}{\partial u} \sin \theta
 \end{aligned}$$

Considering equations (4-33), it is necessary to find $\frac{\partial w}{\partial u}$, $\frac{\partial h}{\partial u}$ and $\frac{\partial A}{\partial u}$ in order to obtain

the first and second columns of \mathbf{J} and \mathbf{J}_τ . These differentials are calculated for the cases

where $u = x, y, x_\tau$ or y_τ .

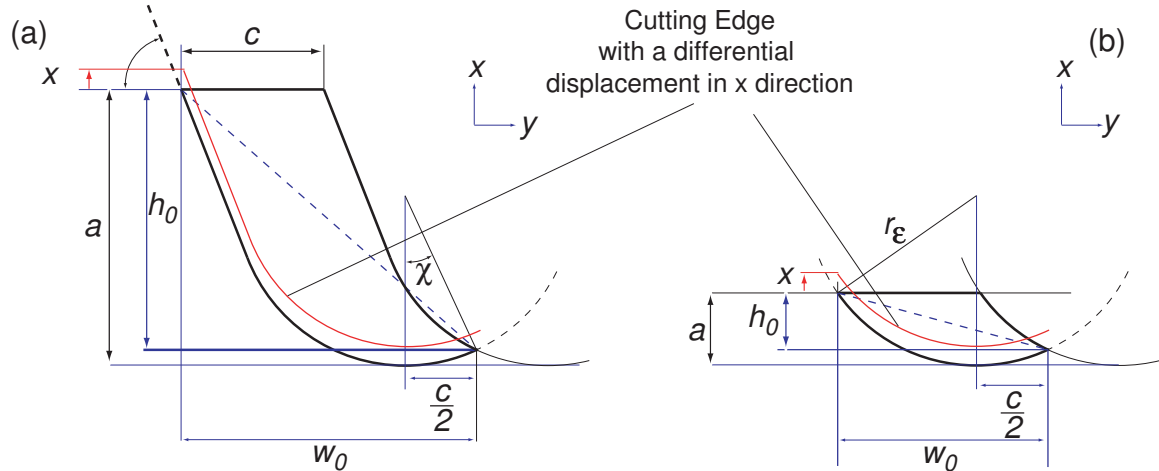


Figure 4-13: Displacement of the cutting edge in the depth of cut direction (a) $a > r_\epsilon(1 - \cos \kappa_r)$, (b) $a \leq r_\epsilon(1 - \cos \kappa_r)$

Differentials with respect to vibrations in the depth of cut direction

Let A_0 , h_0 , and w_0 be the vibration-free chip area, width and height respectively. If the tool vibrates in the x direction (Figure 4-13), the change in the area of chip can be approximately expressed by:

$$A \approx A_0 - w_0 \cdot x \quad \rightarrow \quad \frac{\partial A}{\partial x} = -w_0 = -L \cos \theta \quad (4-40)$$

The differential of the length ($\frac{\partial L}{\partial x}$) is evaluated from the uncut chip area's height (h) and

width (w) as follows:

$$\begin{aligned}
 h &\approx h_0 - \frac{x}{2} && \rightarrow \frac{\partial h}{\partial x} = -\frac{1}{2} \\
 w &= w_0 - \frac{x}{2 \tan \chi} - \frac{x}{\tan \kappa'_r} && \rightarrow \frac{\partial w}{\partial x} = -\frac{1}{2 \tan \chi} - \frac{1}{\tan \kappa'_r}
 \end{aligned}
 \tag{4-41}$$

where $\chi = \arcsin(c/2r_\epsilon)$ is the intersection angle of the present and previous cut as shown in Figure 4-13 and the local approach angle κ'_r is calculated depending on whether the depth of cut is less or greater than the nose radius:

$$\left. \begin{aligned}
 \text{if } a < r_\epsilon(1 - \cos \kappa_r) &\rightarrow \kappa'_r = \cos^{-1}\left(1 - \frac{a}{r_\epsilon}\right) \\
 \text{if } a \geq r_\epsilon(1 - \cos \kappa_r) &\rightarrow \kappa'_r = \kappa_r
 \end{aligned} \right\}
 \tag{4-42}$$

By substituting Eq. (4-41) into Eq. (4-40), the derivative terms $\frac{\partial L}{\partial x}$ and $\frac{\partial \theta}{\partial x}$ are obtained

as:

$$\begin{aligned}
 \frac{\partial L}{\partial x} &= -\frac{\cos \theta}{2 \tan \chi} - \frac{\cos \theta}{\tan \kappa'_r} - \frac{\sin \theta}{2} \\
 \frac{\partial \theta}{\partial x} &= \frac{-\cos \theta}{2L} + \frac{\sin \theta}{2L \tan \chi} + \frac{\sin \theta}{L \tan \kappa'_r}
 \end{aligned}
 \tag{4-43}$$

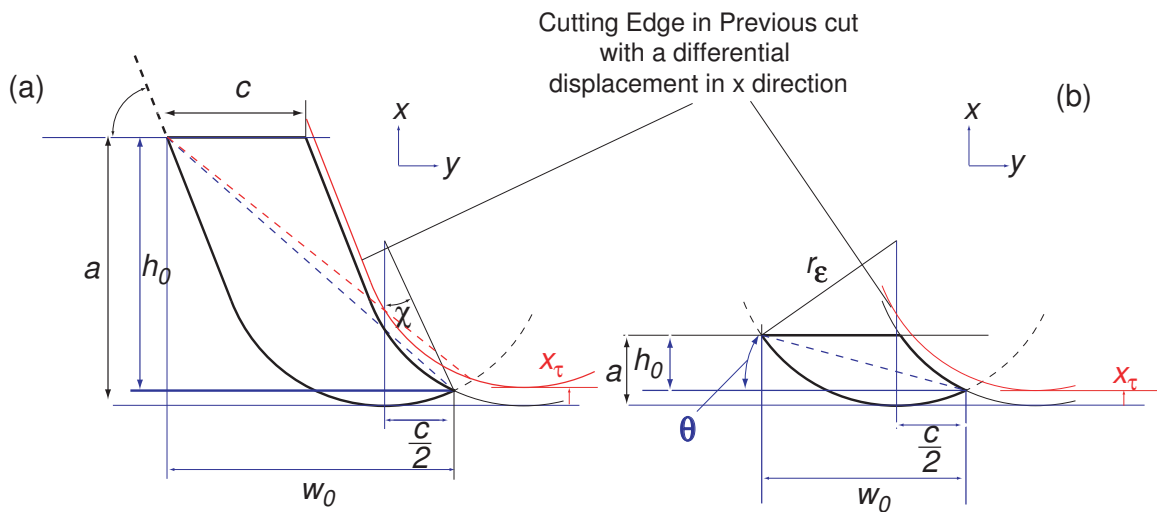


Figure 4-14: Chip area with displacement in depth of cut direction in previous cut

Similarly, the derivatives with respect to the displacement during the previous revolution

($\frac{\partial A}{\partial x_\tau}$, $\frac{\partial L}{\partial x_\tau}$, $\frac{\partial \theta}{\partial x_\tau}$, see Figure 4-14) are evaluated as follows:

$$\left. \begin{aligned} A &\approx A_0 + (w_0 - c)x_\tau \rightarrow \frac{\partial A}{\partial x_\tau} = (w_0 - c) = L \cos \theta - c \\ h &\approx h_0 - \frac{x_\tau}{2} \rightarrow \frac{\partial h}{\partial x_\tau} = -\frac{1}{2} \\ w &\approx w_0 + \frac{x_\tau}{2 \tan \chi} \rightarrow \frac{\partial w}{\partial x_\tau} = \frac{1}{2 \tan \chi} \end{aligned} \right\} \quad (4-44)$$

By substituting $\frac{\partial h}{\partial x_\tau}$ and $\frac{\partial w}{\partial x_\tau}$ from Eq. (4-44) into Eq. (4-39), $\frac{\partial L}{\partial x}$ and $\frac{\partial \theta}{\partial x}$ are found:

$$\left. \begin{aligned} \frac{\partial L}{\partial x_\tau} &= \frac{-\sin \theta}{2} + \frac{\cos \theta}{2 \tan \chi} \\ \frac{\partial \theta}{\partial x_\tau} &= -\frac{\cos \theta + \sin \theta / \tan \chi}{2L} \end{aligned} \right\} \quad (4-45)$$

Differentials with respect to vibrations in feed direction

The vibrations in the direction of feed shifts the chip in (y) direction and affects the chip

shape as follows:

$$\left. \begin{aligned} A &\approx A_0 - hy + \frac{y \cdot y \cdot \tan \chi}{4} \rightarrow \frac{\partial A}{\partial y} = -h = -L \sin \theta \\ h &= h_0 + \frac{y}{2} \cdot \tan \chi \rightarrow \frac{\partial h}{\partial y} = \frac{\tan \chi}{2} \\ w &= w_0 - y + \frac{y}{2} \rightarrow \frac{\partial w}{\partial y} = -\frac{1}{2} \end{aligned} \right\} \quad (4-46)$$

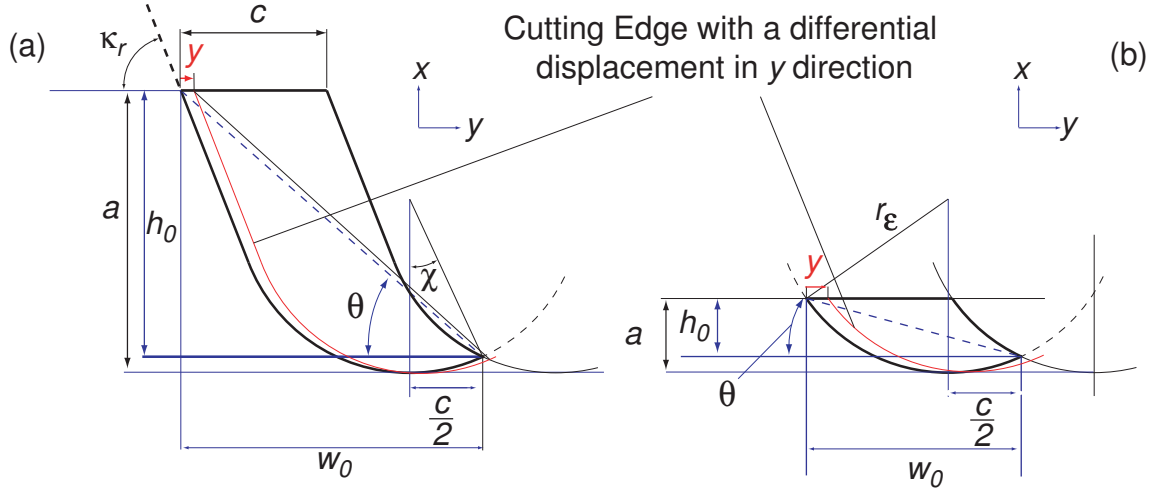


Figure 4-15: Chip area with displacement in depth of cut direction in previous

This leads to the identification of derivatives $\frac{\partial L}{\partial y}$ and $\frac{\partial \theta}{\partial y}$ from Eq. (4-39) as:

$$\left. \begin{aligned} \frac{\partial L}{\partial y} &= \cos \theta \frac{\partial w}{\partial y} + \sin \theta \frac{\partial h}{\partial y} = -\frac{\cos \theta}{2} + \frac{\tan \chi \sin \theta}{2} \\ \frac{\partial \theta}{\partial y} &= \frac{\cos \theta \frac{\partial h}{\partial y} - \sin \theta \frac{\partial w}{\partial y}}{L} = \frac{\cos \theta \tan \chi - \sin \theta}{2L} \end{aligned} \right\} \quad (4-47)$$

If the normal displacements at the present and previous revolutions are equal at a cut ($\Delta y = \Delta y_\tau$), the chip area and other dependant variables (A , L , or θ) will not change ($\Delta A = 0$, $\Delta L = 0$, $\Delta \theta = 0$ see Figure 4-16),

$$\Delta A = \frac{\partial A}{\partial y} \Delta y + \frac{\partial A}{\partial y_\tau} \Delta y_\tau = 0 \rightarrow \frac{\partial A}{\partial y_\tau} = -\frac{\partial A}{\partial y} \quad (4-48)$$

Similarly $\frac{\partial L}{\partial y_\tau} = -\frac{\partial L}{\partial y}$ and $\frac{\partial \theta}{\partial y_\tau} = -\frac{\partial \theta}{\partial y}$, the derivative of the chip area variables with respect to the vibrations in the feed direction during the previous spindle revolution will be identical to the equations given in (4-46) and (4-47) but with an opposite sign.

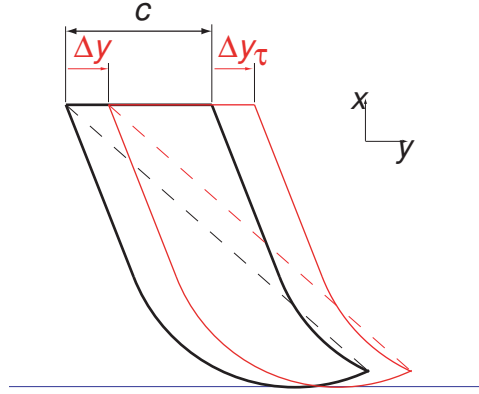


Figure 4-16: Equal displacements in feed direction for in present and previous cut

The summary of results is given in Table 4-1.

Table 4-1: Differentials of chord angle, length and area with respect to displacements in depth of cut and feed directions.

$\frac{\partial \theta}{\partial x} = \frac{-\cos \theta}{2L} + \frac{\sin \theta}{2L \tan \chi} + \frac{\sin \theta}{L \tan \kappa'_r}$	$\frac{\partial L}{\partial x} = -\frac{\cos \theta}{2 \tan \chi} - \frac{\cos \theta}{\tan \kappa'_r} - \frac{\sin \theta}{2}$	$\frac{\partial A}{\partial x} = -L \cos \theta$
$\frac{\partial \theta}{\partial x_\tau} = \frac{-\cos \theta}{2L} + \frac{\sin \theta}{2L \tan \chi}$	$\frac{\partial L}{\partial x_\tau} = \frac{-\sin \theta}{2} + \frac{\cos \theta}{2 \tan \chi}$	$\frac{\partial A}{\partial x_\tau} = L \cos \theta - c$
$\frac{\partial \theta}{\partial y} = \frac{\tan \chi \cos \theta}{2L} + \frac{\sin \theta}{2L}$	$\frac{\partial L}{\partial y} = -\frac{\cos \theta}{2} + \frac{\tan \chi \sin \theta}{2}$	$\frac{\partial A}{\partial y} = -L \sin \theta$
$\frac{\partial \theta}{\partial y_\tau} = -\frac{\tan \chi \cos \theta}{2L} - \frac{\sin \theta}{2L}$	$\frac{\partial L}{\partial y_\tau} = \frac{\cos \theta}{2} - \frac{\tan \chi \sin \theta}{2}$	$\frac{\partial A}{\partial y_\tau} = L \sin \theta$

4.5.2 Process damping gains contributed by flank wear

The process damping theory is employed to calculate \mathbf{J}_v matrix. Wallace and Andrew [48], Chiou and Liang [10], Clancy and Shin [11], and Wu [49] presented dynamic cutting force models which consider the compression of the volume of the work material under the flank face of the cutting tool as discussed in the previous chapter.

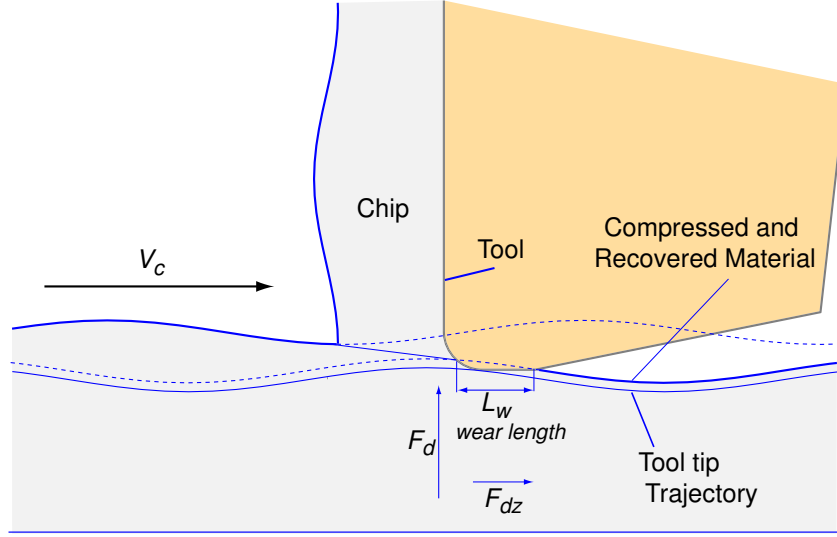


Figure 4-17: Tool wear and process damping forces

The normal (F_d) and friction (F_{dz}) forces caused by the contact are modeled as (Figure 4-17):

$$F_d = K_{sp} V_m, \quad F_{dz} = \mu_c F_d \quad (4-49)$$

where K_{sp} is the experimentally identified contact force coefficient and μ_c is the coefficient of friction and assumed to be 0.3 for steel [49]. As discussed in the previous chapter, Chiou and Liang [10] approximated the compressed volume of the material (V_m) under the tool flank as:

$$V_m = -\frac{1}{2} L_c L_w^2 \frac{\dot{h}}{V_c} \quad (4-50)$$

where \dot{h} is the vibration velocity in the direction normal to the plane defined by the cutting edge and cutting speed (V_c), L_w is the wear land, and L_c is the total length of cutting edge in cut. For a differential element of a curved cutting edge segment with length dL , the vibration velocity is:

$$\dot{h} = \dot{x} \cos \kappa_n + \dot{y} \sin \kappa_n \quad (4-51)$$

where κ_n is varying approach angle (see Figure 4-18).

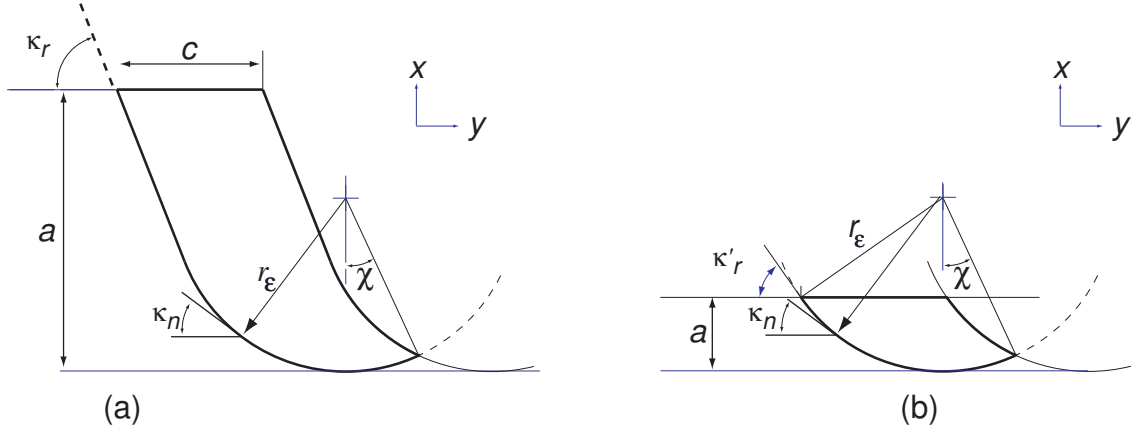


Figure 4-18: Variable Approach Angle

Substituting equations (4-50) and (4-51) into contact force (Eq. (4-49)):

$$dF_d = -\frac{dL L_w^2 K_{sp}}{2V_c} \dot{h} = -\frac{dL L_w^2 K_{sp}}{2V_c} (x \cos \kappa_n + y \sin \kappa_n) \quad (4-52)$$

and by projecting it in the x and y directions, leads to differential contact forces in three directions:

$$dF_{dx} = dF_d \cos \kappa_n, \quad dF_{dy} = dF_d \sin \kappa_n, \quad dF_{dz} = \mu_c dF_d \quad (4-53)$$

They are organized in the matrix form as:

$$\begin{Bmatrix} dF_{dx} \\ dF_{dy} \\ dF_{dz} \end{Bmatrix} = -\frac{L_w^2 K_{sp}}{2V_c} \begin{bmatrix} \cos^2 \kappa_n & \cos \kappa_n \sin \kappa_n & 0 \\ \cos \kappa_n \sin \kappa_n & \sin^2 \kappa_n & 0 \\ \mu_c \cos \kappa_n (\sin \kappa_n + \cos \kappa_n) & \mu_c \sin \kappa_n (\sin \kappa_n + \cos \kappa_n) & 0 \end{bmatrix} dL \begin{Bmatrix} x \\ y \\ z \end{Bmatrix} \quad (4-54)$$

Assuming a constant flank wear (L_w), the velocity-dependent process damping force acting on the structure is evaluated by integrating the differential forces along the cutting

edge. By substituting $L_{\kappa_r} = \frac{a - r_\epsilon (1 - \cos \kappa_r)}{\sin \kappa_r}$, $dL = r_\epsilon \cdot d\kappa_n$ for the straight and curved

sections of the cutting edge, the process damping matrix (\mathbf{J}_v) is obtained as a function of depth of cut:

$$\mathbf{J}_v = \begin{cases} -L_w^2 \cdot \frac{K_{sp}}{2V_c} \cdot \left(L_{\kappa_r} \begin{bmatrix} \cos^2 \kappa_r & \sin \kappa_r \cos \kappa_r & 0 \\ \sin \kappa_r \cos \kappa_r & \sin^2 \kappa_r & 0 \\ \mu_c \cos \kappa_r (\cos \kappa_r + \sin \kappa_r) & \mu_c \sin \kappa_r (\cos \kappa_r + \sin \kappa_r) & 0 \end{bmatrix} + \int \begin{bmatrix} \cos^2 \kappa_n & \sin \kappa_n \cos \kappa_n & 0 \\ \sin \kappa_n \cos \kappa_n & \sin^2 \kappa_n & 0 \\ -\chi \mu_c \cos \kappa_n (\cos \kappa_n + \sin \kappa_n) & \mu_c \sin \kappa_n (\cos \kappa_n + \sin \kappa_n) & 0 \end{bmatrix} r_\epsilon d \kappa_n \right) & a > r_\epsilon (1 - \cos \kappa_r) \\ -L_w^2 \cdot \frac{K_{sp}}{2V_c} \cdot \left(\int \begin{bmatrix} \cos^2 \kappa_n & \sin \kappa_n \cos \kappa_n & 0 \\ \sin \kappa_n \cos \kappa_n & \sin^2 \kappa_n & 0 \\ -\chi \mu_c \cos \kappa_n (\cos \kappa_n + \sin \kappa_n) & \mu_c \sin \kappa_n (\cos \kappa_n + \sin \kappa_n) & 0 \end{bmatrix} r_\epsilon d \kappa_n \right) & a \leq r_\epsilon (1 - \cos \kappa_r) \end{cases} \quad (4-55)$$

$$(\kappa'_r = \cos^{-1}(1 - a / r_\epsilon) \text{ when } a \leq r_\epsilon (1 - \cos \kappa_r))$$

\mathbf{J}_v relates the vibration velocities in the x, y directions to the dynamic cutting forces. It must be noted that an effective process damping gain could be calculated in the direction normal to the approximate chord and considered in one dimensional analytical model (Model I, section 4.4) in addition to analytical Model II.

4.6 Simulations and Experimental Results

Static Cutting Tests: The proposed cutting force model (Eq. (4-3)) is experimentally validated by cylindrical turning of AISI 1045 steel bar as discussed earlier in 4.2. The cutting force coefficients are identified from chatter-free turning tests. The model is able to capture the influence of nose radius, depth of cut and feed with an acceptable accuracy as shown in Figure 4-5 where the tool geometry and evaluated cutting force coefficients are given.

4.6.1 Sensitivity analysis of stability models

A general cylindrical turning process with flexibilities in all directions is simulated to compare the prediction sensitivities of different stability methods as shown in Figure 4-19. The structure is assumed to have equal damping ratio and natural frequencies in all directions ($\zeta_k = 0.05, \omega_{nk} = 600\text{Hz}$); The modal stiffness values are given as $k_{xx} = 40$, $k_{yy} = 100$, $k_{zz} = 25$ and $k_{xy} = k_{yx} = 70$, $k_{zx} = k_{xz} = 25$, $k_{yz} = k_{zy} = 100$ [N/ μm]. The cutting coefficients can be found in the caption of Figure 4-19. The system is considered to be more flexible in the direction of depth of cut like in single point boring operations. The stability analysis has been carried out using the proposed two models, and the effect of process damping is neglected.

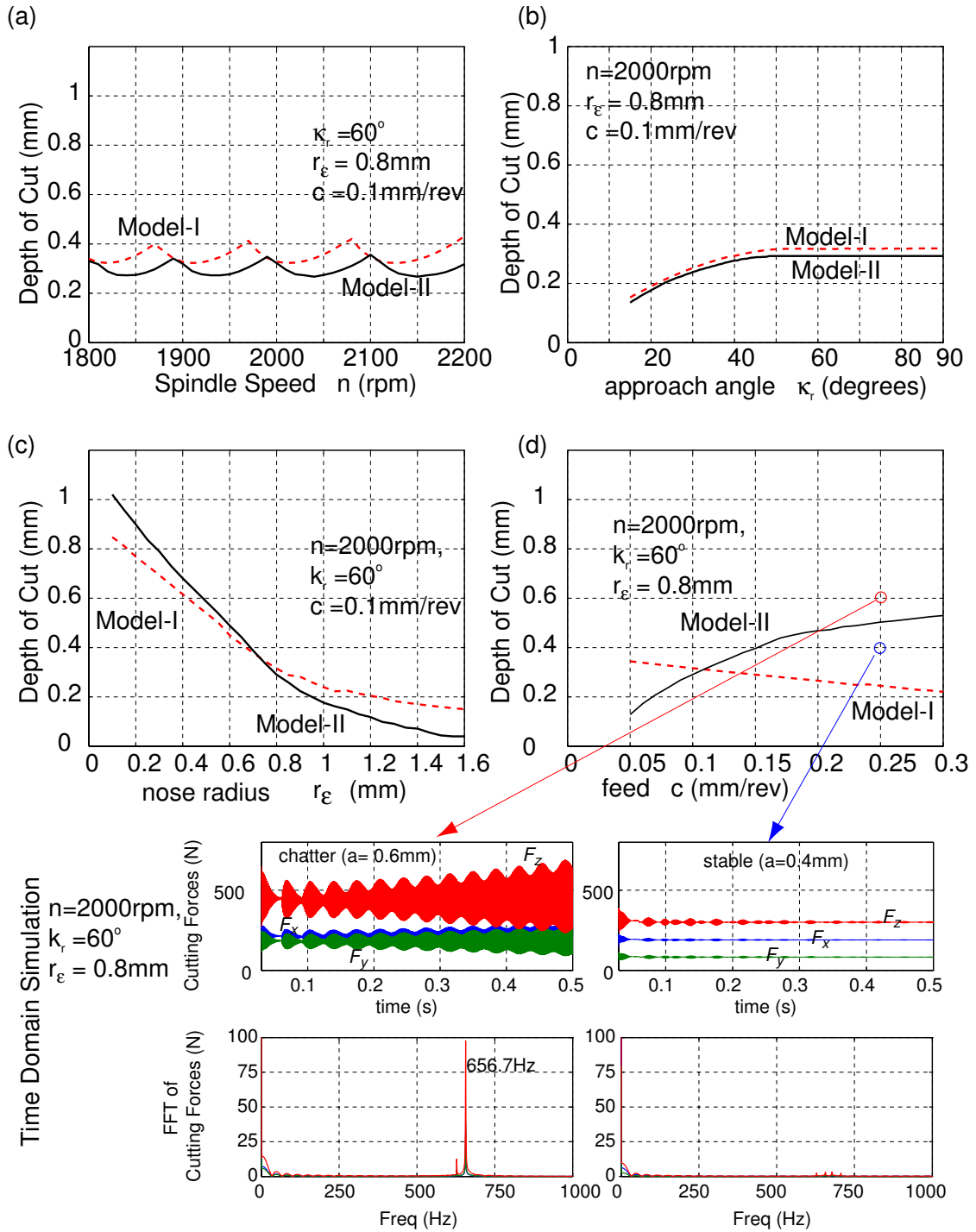


Figure 4-19: Comparison of three stability prediction methods (a) stability chart for a tool $r_\epsilon = 0.8\text{mm}$, $\kappa_r = 60^\circ$ and $c = 0.1\text{mm/rev}$ (b) Effect of approach angle (c) Effect of nose radius; (d) Effect of feed. cutting coefficients: $K_{n0} = 39$, $K_{r0} = -146$, $K_{t0} = -3$ [N]; $K_{nl} = 75000$, $K_{rL} = 90000$, $K_{tL} = 73000$ [N/m], $K_{nA} = 1065$, $K_{rA} = 647$, $K_{tA} = 2516$ [MPa].

Model I: As presented in section 4.4, the approximate chord is used as the equivalent cutting edge and chip regeneration perpendicular to the chord is considered. Since the critical depth of cut and feed are not known a priori, they are recursively searched by evaluating the stability at each cutting condition using Nyquist stability criterion.

Model II: The regeneration of chip area and chord length is considered as presented in Section 4.5. The dynamic cutting model is three dimensional, and threshold of instability is investigated using Nyquist stability criterion by recursively investigating the stability at each cutting condition.

The predicted stability limits at different conditions are compared in Figure 4-19. In Figure 4-19a, the tool has a nose radius of $r_e = 0.8$ mm and approach angle of $\kappa_r = 60^\circ$, and the feed rate is $c = 0.1$ mm/rev. The spindle speed is kept constant at $n=2000$ rev/min while the approach angle varies in Figure 4-19b and the nose radius varies in Figure 4-19c. Models I and II give similar results since the equivalent chord handles the effect of approach angles and nose radius similarly when the feed rate is constant. Model I and II differ significantly when the feed rate varies as shown in Figure 4-19d. The validity of the approximations in evaluating regenerative gains is demonstrated with time domain simulations in Figure 4-19 which indicates the improved accuracy of Model II. The time domain model evaluates the chip area (A), chord angle (θ) and length L analytically by considering the exact geometry of the chip area. Larger feeds change the distribution of chip area and cause smaller overlaps in successive spindle periods; hence, they affect the gains in flexible directions. Ozlu and Budak also observed similar results by discretization the chip into small differential segments along the curved nose and straight section and applying the iterative eigenvalue solution derived from [3]. Particularly, the

regeneration in the direction of depth of cut becomes very strong if the system is flexible in the same direction, which is the case in turning long, slender shafts.

4.6.2 Chatter tests with varying nose radius and feed rates

A series of turning tests with various feeds and nose radii have been conducted on 41.3mm in diameter and 235mm long AISI1045 steel bars. The bars are cantilevered at the chuck with an experimentally identified, single-degree of freedom dynamics at the free end where the cutting tests are conducted. The identified modal parameters in the radial and tangential directions are: $\omega_n = 402$ [Hz], $\zeta = 0.026$ and $k_{yy} = 5.301$ [N/ μm]. The shafts are rigid in the axial direction, and the tool is fed in the radial direction. The cutting force coefficients for this particular tool and work material are identified experimentally as: $K_{n0} = 3$, $K_{r0} = -24$, $K_{t0} = -1$ [N]; $K_{nL} = 83$, $K_{rL} = 26$, $K_{tL} = 44$ [N/mm]; $K_{nA} = 1544$, $K_{rA} = -124$, $K_{tA} = 2881$ [N/mm²].

The effect of nose radius is validated by keeping the spindle speed and feed rate constant at 2000rev/min and 0.1mm/rev respectively. The chatter test results are given in Figure 4-20. As elaborated in the sensitivity analysis (Figure 4-19), the predicted stability limits obtained from models I and II agree well with the experiments. It should be noted that the larger nose radius directs the cutting forces towards the rigid axial direction and provides a higher stability limit in this experimental set up. However, if the feed was along the shaft axis, a larger nose radius would direct the cutting forces towards the more flexible radial direction and decrease the stability limit. The models I and II are able to consider the effect of nose radius which shifts the orientation of the major force.

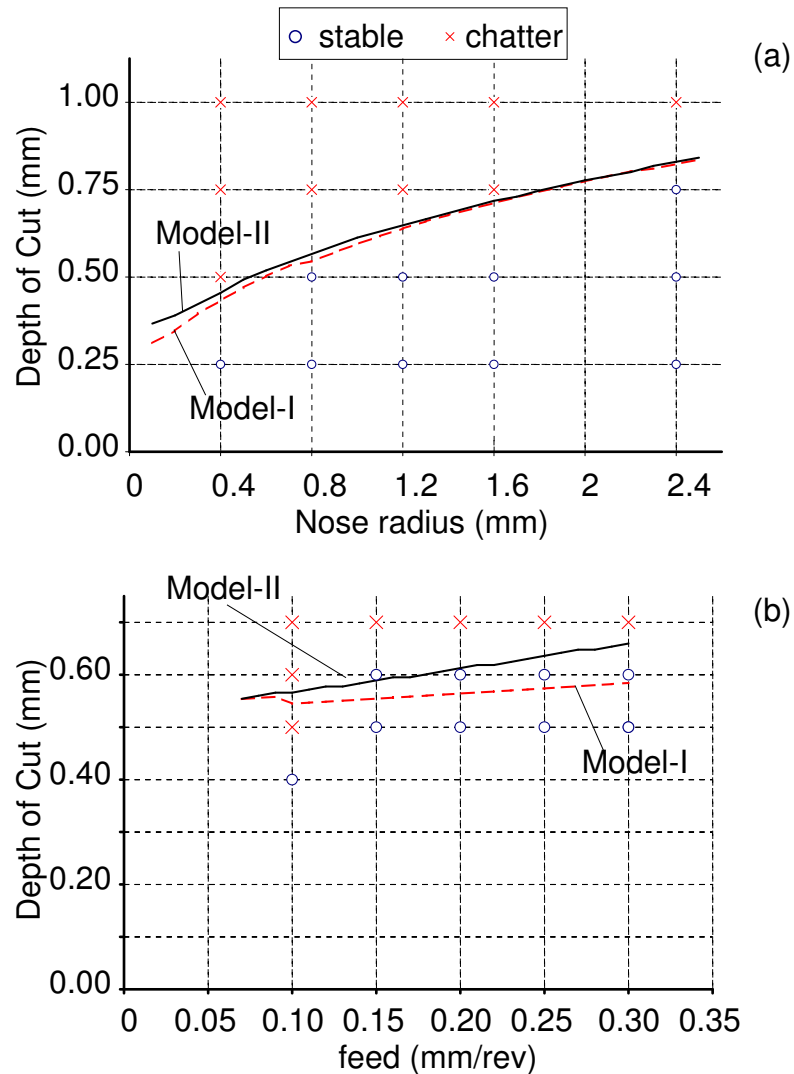


Figure 4-20: (a) Effect of nose radius and (b) effect of feed on stability limit. Tool: Sandvik CNMA1204 KR 3205 series coated inserts on DLCNL holder with -6° rake, -6° inclination, and $\kappa_r = 95^\circ$ approach angles, respectively.

The effect of feed rate is validated using the same experimental set up where the nose radius and spindle speed are kept constant at 0.8mm and 2000rev/min respectively. Although model II predicts the stability limit slightly more accurately than Model I in this particular set up, the discrepancy may be bigger depending on the direction of flexibilities.

4.6.3 Chatter tests with varying spindle speed

The effect of process damping is validated by turning the same shaft material with the same tool but with a constant nose radius of $r_{\epsilon} = 0.8 \text{ mm}$ and approach angle of $\kappa_r = 95^\circ$. However, the shaft is kept short, i.e. rigid, and the feed was along the rigid shaft axis. The flexibility originated from the tool holder fixture whose measured modal parameters are given in Table 4-2. The turret has dominant structural modes at 242 and 340Hz with coupling terms which affect the regeneration in both feed (y) and radial depth of cut (x) directions.

The contact force coefficient (K_{sp}) needed in the process damping matrix is obtained by forcing the tool flank, which had $L_w = 130 \mu\text{m}$ wear, to penetrate into the work material at a $5 \mu\text{m}$ interval. The contact force is measured by the tool dynamometer and the penetrations into the work material are controlled by CNC. The depth of cut is 2.0 mm, and the contact forces increase linearly with a slope of $F_x / x = 4.2 \text{ N}/\mu\text{m}$ and $F_y / y = 7.7 \text{ N}/\mu\text{m}$, which led to a contact force coefficients of $K_{sp} = 4.7 \times 10^{13} \text{ N/m}^3$ in x and $K_{sp} = 3.2 \times 10^{13} \text{ N/m}^3$ in y directions. The tools have varying flank wear between 0.075mm (fresh) and 0.175mm (worn) during tests. An average contact force coefficient of $K_{sp} = 4.0 \times 10^{13} \text{ N/m}^3$ is used in calculating the stability limits shown in Figure 4-21.

The onset of the chatter is detected by monitoring the sound pressure measured with a microphone and an accelerometer attached underneath the tool holder. When the frequency spectrum has significant strength around modal frequencies but not at the spindle's rotational frequency accompanied by high pitch noise and poor surface finish,

the presence of chatter is assumed. Sample acceleration measurements and their spectra are shown for a stable ($a=2.5\text{mm}$, $n=200\text{rev/min}$) and unstable ($a=2.5\text{mm}$, $n=400\text{rev/min}$) cutting conditions. The chatter free cutting conditions at higher speeds above 1500rev/min correspond to stability pockets. The experiments indicate an unexpected decrease in the stability at lower speeds, where the cutting process exhibited poor shear and surface finish even without chatter. The experimental evaluation of cutting force coefficients shown in Table 4-3 reveals that the magnitude starts to increase at cutting speeds under 100m/min , which causes chatter during experiments in smaller depth of cuts. However, the process damping also starts becoming most effective at this zone, leading to increased stability. Since the proposed model evaluates the stability at each cutting condition, speed-dependent cutting force coefficient, interpolated from data listed in Table 4-3, is used to calculate depth of cut and feed dependent process gains.

Table 4-2: Modal Parameters of chatter test setup

Modes	Directional Stiffness ($\text{N}/\mu\text{m}$)					
	XX	YY	ZZ	XY	ZX	YZ
$\omega_n = 242$ [Hz] $\zeta = 0.03$	125	91		-109		
$\omega_n = 340$ [Hz] $\zeta = 0.04$		59	185	735		133

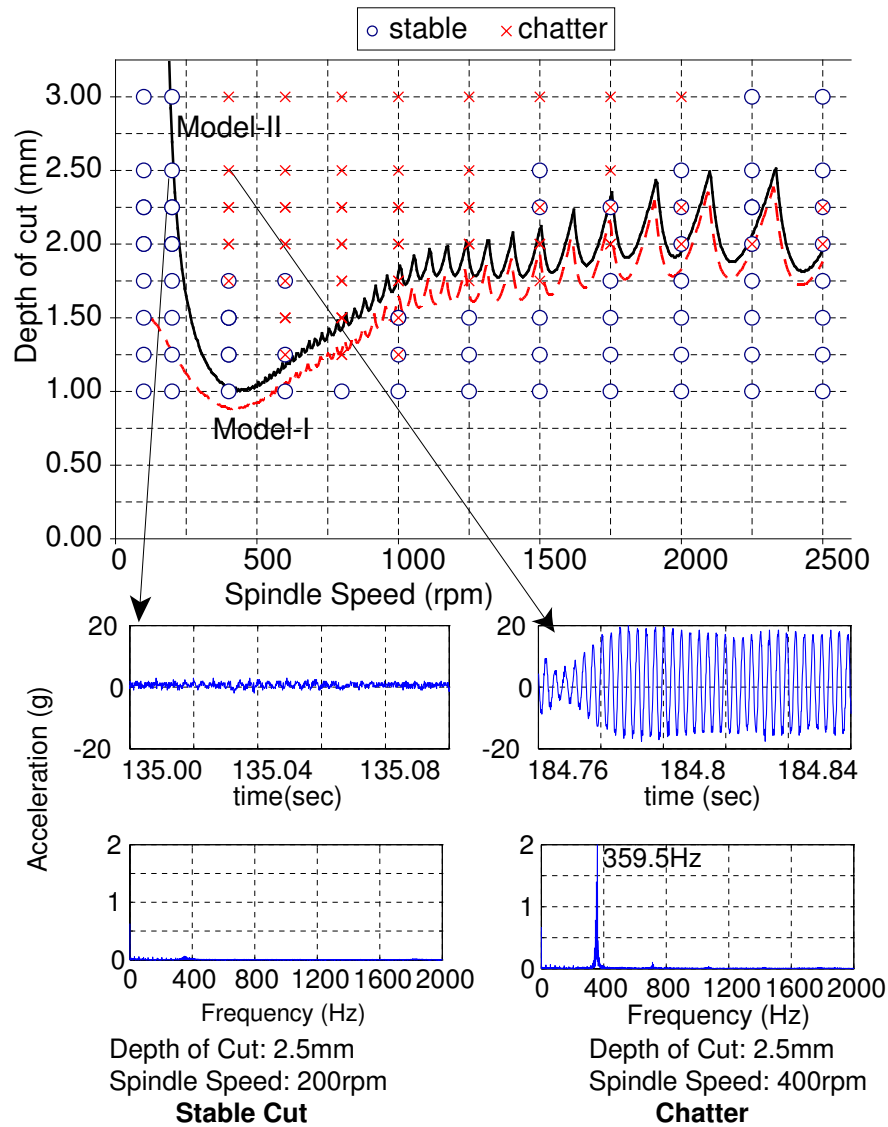


Figure 4-21: Comparison of predicted and experimentally observed chatter stability results for turning with sample vibration measurements at stable ($a = 2.5$ mm, $n = 200$ rev/min) and unstable ($a = 2.5$ mm, $n = 400$ rev/min) cutting conditions. Feed rate $c = 0.1$ mm/rev and nose radius $r_e = 0.8$ mm . See Table 4-2 and Table 4-3 for the modal parameters and cutting coefficients respectively.

The stability of the process is predicted by the proposed Model I and II. The effect of nose radius and the depth of cut are considered using equivalent chord length, but the dynamic changes in the chip area and chord length are neglected in Model I (section 4.4).

The proposed Model II (section 4.5) considers cutting conditions (depth of cut, feed and speed), tool geometry, and the regenerative displacements and their effects on the

dynamic chip area and edge contact length. The penetration of tool flank into the finish surface at low speeds, which adds damping to the process, is considered only in Model II using the contact force model. The stability limit at high speeds is predicted similarly by both models, and the influence of process damping at low speeds is predicted by Model II.

Table 4-3: Cutting coefficients for AISI 1045 steel at different speeds; same tool is used as given in Figure 6.

n (rpm)	V_c (m/min)	K_{nL} (N/mm)	K_{nA} (MPa)	K_{rL} (N/mm)	K_{rA} (MPa)	K_{tL} (N/mm)	K_{tA} (MPa)
100	12	50	1816	10	-25	43	3512
200	25	28	2458	0	-5	32	3776
400	49	0	4359	-2	188	10	4811
600	74	31	3364	-5	172	25	4152
800	99	57	2509	10	53	37	3623
1000	123	77	1937	23	-52	46	3235
1250	154	79	1773	28	-81	46	3102
1500	185	81	1639	26	-85	39	3294
1750	216	81	1580	27	-115	44	2937
2000	247	83	1544	26	-124	44	2881
2250	278	81	1619	35	-219	41	2929
2500	308	80	1698	44	-293	37	3042

4.7 Conclusion

This chapter proposes one and three-dimensional dynamic cutting models for the prediction of chatter stability in single point cutting operations. One-dimensional Model I is based on the equivalent chord and it considers the regeneration of the chip which is assumed to take place perpendicular to the chord drawn between the two ends of chip cross section. Model II, however, considers the changes in the chip area and equivalent chip contact length due to vibrations in depth of cut and feed directions. The contact between the tool flank and finish surface is included by predicting the amount of material

volume indented by the flank of the tool. The experimental results indicate that the accuracy of chatter stability prediction of both models is acceptable except the influence of feed rate is captured by Model II. The process damping model, which considers tool flank contact with the finish surface, predicts the increased stable depth of cut at low speeds.

Chapter 5: Stability of Milling at Process Damping

Speeds

5.1 Introduction

As discussed in earlier chapters, while aluminum alloys are machined at high speeds, thermal-resistant and steel alloys are milled mostly at low speeds in aerospace and die and mold industries. High speed milling machines use high power electro-spindles with small shaft diameters. Machine tools dedicated to machining thermal-resistant and steel alloys use spindles with high torque and stiffness. One of the fundamental obstacles in improving the material removal rates in all milling operations is chatter, the instability caused by the relative vibrations between the tool and the workpiece. The rotating spindle, tool-holder and cutter are the most flexible parts of the machine; hence they are the main causes of chatter in milling. Vibrations create wavy chips, which in turn generates oscillating cutting forces at the same frequency of chatter vibrations. When the spindle speed (i.e. phase) and the depth of cut (i.e. gain) violate the chatter stability limits, exponentially growing unstable vibrations generate poor surface finish and may damage both the machine tool spindle and the workpiece. When the tooth passing frequency matches with the integer fraction of spindle speed, the phase between the outer and inner waves generated on the chips become minimum, which occurs at the first few stability pockets as discovered by Tobias [46]. Smith and Tlustý used the high speed spindle technology to operate the machines in these stability pockets, and they demonstrated significant gains in metal removal rates [40]. High speed machining led to

improved chatter stability laws which considered periodic, time-varying dynamics of milling. As discussed in Chapter 2, several stability prediction methods were proposed by Sridhar et. al. [39], Minis and Yanushevsky[27], Altintas and Budak [3] and Insperger et al. [21]. Altintas and Weck summarized the state of dynamic cutting research, and indicated that speed-dependent process damping and structural dynamics of the machines were still the main obstacles in predicting chatter stability limits in metal cutting [5].

This chapter presents a new dynamic model of milling with process damping and a cutter having asymmetric structural dynamics. The previous studies assumed that the structural dynamics of the system remain stationary at fixed directions. Li et al. [25] showed that when the structural dynamic system rotates, it has considerable effects in single-point boring systems which have time invariant directional factors. Schmitz et al. showed that the frequency response function of the spindle-tool holder assembly changes with speed [37], which may be due to the gyroscopic effects and bearing preload adjustments as the speed increases [37]. In addition, if a milling cutter has two teeth or uneven spacing between the teeth, the effective frequency response function of the tool varies as the cutter rotates due to asymmetric dynamics. Furthermore, the directional factors also vary with time due to milling process kinematics. A rotating coordinate system is attached to the cutter and a fixed coordinate system is used for the workpiece dynamics in this chapter. The proposed model is therefore applicable to all milling configurations with rotating and/or fixed structural dynamics. The process damping force has also been taken account of in the proposed dynamic milling model. The process damping coefficient is identified either experimentally [41] [20], or from contact mechanics models proposed in

the literature [49] considering the tool wear and material penetration coefficient (K_{sp}) [48]. Based on these work, in this chapter, the process damping force is considered to be proportional to the angle between the tool's wear land and the freshly cut workpiece during the vibration; this angle is proportional to the vibration speed divided by the cutting speed. The stability of the speed-dependent milling system is investigated using Nyquist stability criterion after averaging time-varying directional factors. The validity of the stability model is illustrated with numerical simulations and low/high speed milling experiments.

Henceforth, the chapter is organized as follows: The mathematical model of dynamic milling process is presented in Section 5.2. The structural dynamics of the tool in rotating and the workpiece in fixed coordinate systems are presented in section 5.3. The characteristic equation for stability analysis of dynamic milling system is derived in section 5.4, followed by simulation and experimental results in section 5.5. The chapter is concluded in section 5.6 and derivations of directional factor matrices are given in the Appendix C.

5.2 Dynamic Cutting Force Model

A rotating end mill and a stationary workpiece couple have dynamic flexibilities in two orthogonal directions as shown in Figure 5-1. The dynamics of the end mill is modeled in rotating coordinate system in orthogonal (v) and (u) directions whereas the workpiece is modeled in a fixed Cartesian coordinate system with feed (x) and normal (y) directions. (v) and (u) are selected to be the principal directions of the tool's most

flexible vibration mode. This choice eliminates dynamic cross coupling between these two directions.

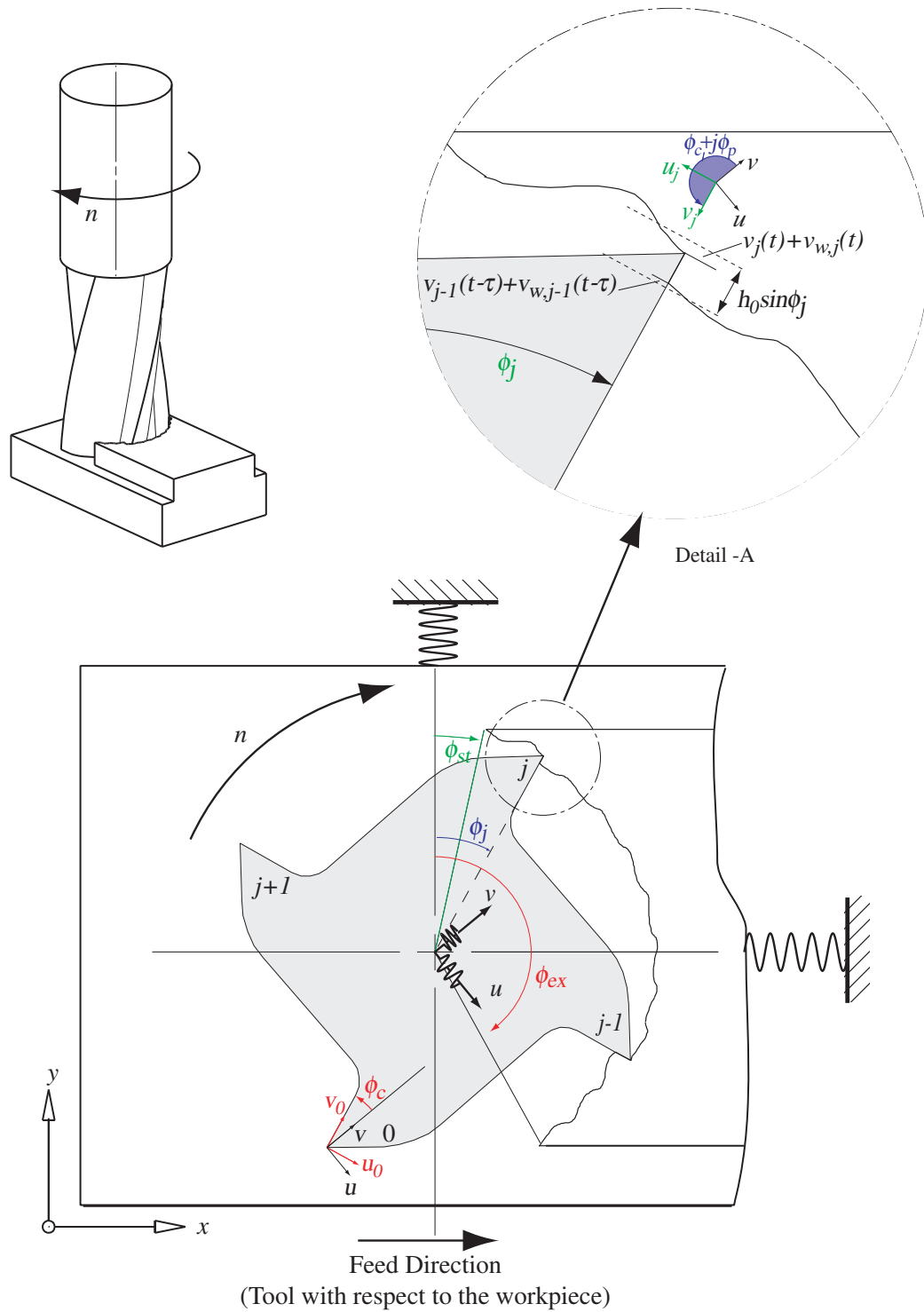


Figure 5-1: Milling of a flexible workpiece with a rotating and vibrating cutter.

When the vibrating part is fed linearly towards rotating and vibrating cutter, the dynamic chip thickness experienced by the tooth (j) is expressed as:

$$h_j(t) = \left\{ c \sin \phi_j(t) - [v_j(t) - v_{j-1}(t - \tau)] - [v_{wj}(t) - v_{w,j-1}(t - \tau)] \right\} \quad (5-1)$$

where c is the feed per tooth, ϕ_j is the angular immersion of the tooth j ; and τ is the tooth passing delay between teeth j and $j - 1$. $v_j(t)$ and $v_{w,j}(t)$ are the vibrations of the tool and workpiece reflected on tooth j in the radial direction respectively.

The displacements of the tooth j is related to two displacements in orthogonal (v, u) system as,

$$\begin{Bmatrix} v_j(t) \\ u_j(t) \end{Bmatrix} = \mathbf{R}_j \begin{Bmatrix} v(t) \\ u(t) \end{Bmatrix}, \quad \mathbf{R}_j = \begin{bmatrix} \cos(j\phi_p + \phi_c) & -\sin(j\phi_p + \phi_c) \\ \sin(j\phi_p + \phi_c) & \cos(j\phi_p + \phi_c) \end{bmatrix} \quad j = 0, 1, \dots, N - 1 \quad (5-2)$$

where $\phi_p = 2\pi/N$ is the pitch angle of the cutter with N equally spaced teeth and ϕ_c is the angle between the principal direction “ v ” and the tooth zero ($j = 0$). The instantaneous angle of the rotating coordinate system is given by $\phi = \Omega t$, where Ω (rad/s) is the angular spindle speed as seen in Figure 5-1. The angular position of flute j becomes:

$$\phi_j = \phi - j\phi_p - \phi_c \quad (5-3)$$

The fixed workpiece vibrations in (x, y) directions are carried to the rotating coordinate system (v_w, u_w) and to the tooth j as:

$$\begin{aligned} \begin{Bmatrix} v_w(t) \\ u_w(t) \end{Bmatrix} &= \mathbf{W}(t) \begin{Bmatrix} x(t) \\ y(t) \end{Bmatrix}, \quad \mathbf{W}(t) = \begin{bmatrix} \sin \phi & \cos \phi \\ \cos \phi & -\sin \phi \end{bmatrix} \\ \begin{Bmatrix} v_{w,j}(t) \\ u_{w,j}(t) \end{Bmatrix} &= \mathbf{R}_j \begin{Bmatrix} v_w(t) \\ u_w(t) \end{Bmatrix} = \mathbf{R}_j \mathbf{W}(t) \begin{Bmatrix} x(t) \\ y(t) \end{Bmatrix} \end{aligned} \quad (5-4)$$

The rigid body term ($c \sin \phi_j(t)$) is dropped from the dynamic chip load (Eq. (5-1)) for stability analysis since it works as a forced excitation which does not affect the stability of the linearized system. The resulting dynamic chip thickness generated by the vibrations is expressed as:

$$\begin{aligned} h_j(t) = -[1 \quad 0] &\left(\begin{bmatrix} \mathbf{R}_j \end{bmatrix} \begin{Bmatrix} v(t) \\ u(t) \end{Bmatrix} - \begin{bmatrix} \mathbf{R}_{j-1} \end{bmatrix} \begin{Bmatrix} v(t-\tau) \\ u(t-\tau) \end{Bmatrix} \right) \\ &+ \begin{bmatrix} \mathbf{R}_j \mathbf{W}(t) \end{bmatrix} \begin{Bmatrix} x(t) \\ y(t) \end{Bmatrix} - \begin{bmatrix} \mathbf{R}_j \mathbf{W}(t) \end{bmatrix} \begin{Bmatrix} x(t-\tau) \\ y(t-\tau) \end{Bmatrix} \end{aligned} \quad (5-5)$$

The tangential ($F_{t,j}$) and radial ($F_{r,j}$) cutting forces have two parts: regenerative force proportional to the dynamic chip thickness ($h_j(t)$) and process damping effect which is proportional to the ratio of velocities of vibration ($V_{j/lw}$) and cutting speed (V_c) or the slope change on the waves left on the cut surface:

$$\begin{Bmatrix} F_{r,j} \\ F_{t,j} \end{Bmatrix} = g(\phi_j) a \left(\begin{Bmatrix} K_r \\ K_t \end{Bmatrix} h_j(t) - \begin{Bmatrix} C_r \\ C_t \end{Bmatrix} \frac{V_{j/lw}}{V_c} \right) \quad (5-6)$$

The depth of cut is a and the pairs, K_r , K_t and C_r , C_t are the static cutting force and the process damping coefficients respectively. In Equation (5-6), the helix angle of the tool is assumed zero to simplify the formulation. The unit step function $g(\phi_j)$ is used to model whether the tooth is in or out of cut:

$$g(\phi_j) = \begin{cases} 1 & \phi_{st} \leq \text{mod}(\phi_j, 2\pi) \leq \phi_{ex} \\ 0 & \text{otherwise} \end{cases} \quad (5-7)$$

The velocity of the workpiece vibration is transformed to the cutting edge j from equations (5-2) and (5-4):

$$\begin{Bmatrix} V_{wj}(t) \\ U_{wj}(t) \end{Bmatrix} = \mathbf{R}_j \mathbf{W}(t) \begin{Bmatrix} \frac{dx}{dt} \\ \frac{dy}{dt} \end{Bmatrix} = \begin{Bmatrix} \sin \phi_j x + \cos \phi_j y \\ \cos \phi_j x - \sin \phi_j y \end{Bmatrix} \quad (5-8)$$

The vector $\vec{P} = v\hat{v} + u\hat{u}$ is the position of the centre of the tool. The velocity of this point is:

$$\frac{d\vec{P}}{dt} = v\dot{\hat{v}} + u\dot{\hat{u}} + \Omega v\hat{u} - \Omega u\hat{v} \Rightarrow \begin{Bmatrix} V_p \\ U_p \end{Bmatrix} = \begin{Bmatrix} \dot{v} \\ \dot{u} \end{Bmatrix} + \Omega \begin{bmatrix} 0 & -1 \\ 1 & 0 \end{bmatrix} \begin{Bmatrix} v \\ u \end{Bmatrix} \quad (5-9)$$

Therefore, the velocity of tip j in v_j, u_j coordinate system becomes:

$$\begin{Bmatrix} V_j \\ U_j \end{Bmatrix} = \begin{Bmatrix} 0 \\ -V_c \end{Bmatrix} + \mathbf{R}_j \begin{Bmatrix} V_p \\ U_p \end{Bmatrix} = \begin{Bmatrix} 0 \\ -V_c \end{Bmatrix} + \mathbf{R}_j \begin{Bmatrix} \dot{v} \\ \dot{u} \end{Bmatrix} + \Omega \mathbf{R}_j \begin{bmatrix} 0 & -1 \\ 1 & 0 \end{bmatrix} \begin{Bmatrix} v \\ u \end{Bmatrix} \quad (5-10)$$

The relative velocity of the tool penetrating into the workpiece ($V_{j/w}$) is found from the vector summation of the velocities of the workpiece and the cutting edge in the fixed coordinate system:

$$\begin{aligned} V_{j/w} &= [1 \ 0] \left(\begin{Bmatrix} V_{wj}(t) \\ U_{wj}(t) \end{Bmatrix} + \begin{Bmatrix} V_j(t) \\ U_j(t) \end{Bmatrix} \right) \\ &= [1 \ 0] \mathbf{R}_j \mathbf{W}(t) \begin{Bmatrix} \dot{x} \\ \dot{y} \end{Bmatrix} + [1 \ 0] \mathbf{R}_j \begin{Bmatrix} \dot{v}(t) \\ \dot{u}(t) \end{Bmatrix} + \Omega [1 \ 0] \mathbf{R}_j \begin{bmatrix} 0 & -1 \\ 1 & 0 \end{bmatrix} \begin{Bmatrix} v(t) \\ u(t) \end{Bmatrix} \end{aligned} \quad (5-11)$$

By substituting dynamic chip thickness (Eq.(5-1)) and tool penetration velocity (Eq.(5-12)) into cutting force on tooth j (Eq. (5-6)), the following can be obtained:

$$\begin{aligned} \begin{Bmatrix} F_{r,j} \\ F_{t,j} \end{Bmatrix} &= g(\phi_j) a \begin{bmatrix} -K_r \\ K_t \end{bmatrix} [1 \ 0] \left(\mathbf{R}_j \begin{Bmatrix} v(t) \\ u(t) \end{Bmatrix} - \mathbf{R}_{j-1} \begin{Bmatrix} v(t-\tau) \\ u(t-\tau) \end{Bmatrix} + \mathbf{R}_j \mathbf{W}(t) \begin{Bmatrix} x(t) \\ y(t) \end{Bmatrix} - \mathbf{R}_j \mathbf{W}(t) \begin{Bmatrix} x(t-\tau) \\ y(t-\tau) \end{Bmatrix} \right) \\ &\quad - \frac{1}{V_c} \begin{Bmatrix} C_r \\ C_t \end{Bmatrix} \left([1 \ 0] \mathbf{R}_j \mathbf{W}(t) \begin{Bmatrix} \dot{x} \\ \dot{y} \end{Bmatrix} + [1 \ 0] \mathbf{R}_j \begin{Bmatrix} \dot{v} \\ \dot{u} \end{Bmatrix} + \Omega [1 \ 0] \mathbf{R}_j \begin{bmatrix} 0 & -1 \\ 1 & 0 \end{bmatrix} \begin{Bmatrix} v \\ u \end{Bmatrix} \right) \end{aligned} \quad (5-12)$$

The corner radius of a tool generates a curved chip cross-section and affects the direction of cutting forces; in such case, the dynamic force model would be expressed using equivalent edge model of Colwell as shown in Chapter 4. The total dynamic cutting forces are evaluated by projecting all forces from individual flutes to the reference coordinate system and adding them together:

$$\begin{Bmatrix} F_v \\ F_u \end{Bmatrix} = \sum_{j=0}^{N-1} \mathbf{R}_j^{-1} \begin{Bmatrix} F_{r,j} \\ F_{t,j} \end{Bmatrix} \quad (5-13)$$

Taking (5-12) into consideration, Eq. (5-13) becomes:

$$\begin{aligned} \begin{Bmatrix} F_v \\ F_u \end{Bmatrix} &= -a \underbrace{\sum_{j=0}^{N-1} g(\phi_j) \mathbf{R}_j^{-1} \begin{bmatrix} K_r \\ K_t \end{bmatrix} [1 \ 0] \mathbf{R}_j + \frac{\Omega}{V_c} \begin{Bmatrix} C_r \\ C_t \end{Bmatrix} [1 \ 0] \mathbf{R}_j \begin{bmatrix} 0 & -1 \\ 1 & 0 \end{bmatrix}}_{\mathbf{A}} \begin{Bmatrix} v(t) \\ u(t) \end{Bmatrix} \\ &\quad + a \underbrace{\sum_{j=0}^{N-1} g(\phi_j) \mathbf{R}_j^{-1} \begin{bmatrix} K_r \\ K_t \end{bmatrix} [1 \ 0] \mathbf{R}_{j-1}}_{\mathbf{B}} \begin{Bmatrix} v(t-\tau) \\ u(t-\tau) \end{Bmatrix} \\ &\quad - a \underbrace{\sum_{j=0}^{N-1} g(\phi_j) \mathbf{R}_j^{-1} \begin{bmatrix} K_r \\ K_t \end{bmatrix} [1 \ 0] \mathbf{R}_j \mathbf{W}(t)}_{\mathbf{C}} \begin{Bmatrix} x(t) \\ y(t) \end{Bmatrix} \\ &\quad + a \underbrace{\sum_{j=0}^{N-1} g(\phi_j) \mathbf{R}_j^{-1} \begin{bmatrix} K_r \\ K_t \end{bmatrix} [1 \ 0] \mathbf{R}_j \mathbf{W}(t)}_{\mathbf{C}} \begin{Bmatrix} x(t-\tau) \\ y(t-\tau) \end{Bmatrix} \\ &\quad - a \underbrace{\sum_{j=0}^{N-1} g(\phi_j) \frac{\mathbf{R}_j^{-1}}{V_c} \begin{Bmatrix} C_r \\ C_t \end{Bmatrix} [1 \ 0] \mathbf{R}_j}_{\mathbf{E}} \begin{Bmatrix} \dot{v}(t) \\ \dot{u}(t) \end{Bmatrix} \\ &\quad - a \underbrace{\sum_{j=0}^{N-1} g(\phi_j) \frac{\mathbf{R}_j^{-1}}{V_c} \begin{Bmatrix} C_r \\ C_t \end{Bmatrix} [1 \ 0] \mathbf{R}_j \mathbf{W}(t)}_{\mathbf{F}} \begin{Bmatrix} \dot{x}(t) \\ \dot{y}(t) \end{Bmatrix} \end{aligned} \quad (5-14)$$

Therefore, the following equation would result:

$$\begin{aligned}
 \begin{Bmatrix} F_v \\ F_u \end{Bmatrix} &= a \left(-\mathbf{A}(t) \begin{Bmatrix} v(t) \\ u(t) \end{Bmatrix} + \mathbf{B}(t) \begin{Bmatrix} v(t-\tau) \\ u(t-\tau) \end{Bmatrix} - \mathbf{C}(t) \begin{Bmatrix} x(t) \\ y(t) \end{Bmatrix} \right. \\
 &\quad \left. + \mathbf{C}(t) \begin{Bmatrix} x(t-\tau) \\ y(t-\tau) \end{Bmatrix} - \mathbf{E}(t) \begin{Bmatrix} \dot{v}(t) \\ \dot{u}(t) \end{Bmatrix} - \mathbf{F}(t) \begin{Bmatrix} \dot{x}(t) \\ \dot{y}(t) \end{Bmatrix} \right)
 \end{aligned} \tag{5-15}$$

The components of the dynamic cutting force acting on the fixed workpiece are obtained by projecting the forces from the rotating reference system to the feed (x) and normal (y) directions:

$$\begin{aligned}
 \begin{Bmatrix} F_x(t) \\ F_y(t) \end{Bmatrix} &= \mathbf{W}^{-1}(t) \begin{Bmatrix} F_v(t) \\ F_u(t) \end{Bmatrix} \\
 &= a \left(-\mathbf{W}^{-1}(t) \mathbf{A}(t) \begin{Bmatrix} v(t) \\ u(t) \end{Bmatrix} + \mathbf{W}^{-1}(t) \mathbf{B}(t) \begin{Bmatrix} v(t-\tau) \\ u(t-\tau) \end{Bmatrix} \right. \\
 &\quad \left. - \mathbf{C}(t) \begin{Bmatrix} x(t) \\ y(t) \end{Bmatrix} + \mathbf{W}^{-1}(t) \mathbf{C}(t) \begin{Bmatrix} x(t-\tau) \\ y(t-\tau) \end{Bmatrix} \right. \\
 &\quad \left. - \mathbf{W}^{-1}(t) \mathbf{E}(t) \begin{Bmatrix} \dot{v}(t) \\ \dot{u}(t) \end{Bmatrix} - \mathbf{W}^{-1}(t) \mathbf{F}(t) \begin{Bmatrix} \dot{x}(t) \\ \dot{y}(t) \end{Bmatrix} \right)
 \end{aligned} \tag{5-16}$$

The forces in rotational and fixed coordinates are expressed in a matrix form as linear functions of displacement vectors:

$$\begin{aligned}
 \begin{Bmatrix} F_v(t) \\ F_u(t) \\ F_x(t) \\ F_y(t) \end{Bmatrix} &= -a \underbrace{\begin{bmatrix} \mathbf{A}(t) & \mathbf{C}(t) \\ \mathbf{W}^{-1}(t)\mathbf{A}(t) & \mathbf{W}^{-1}(t)\mathbf{C}(t) \end{bmatrix}}_{\mathbf{P}(t)} \begin{Bmatrix} v(t) \\ u(t) \\ x(t) \\ y(t) \end{Bmatrix} \\
 &+ a \underbrace{\begin{bmatrix} \mathbf{B}(t) & \mathbf{C}(t) \\ \mathbf{W}^{-1}(t)\mathbf{B}(t) & \mathbf{W}^{-1}(t)\mathbf{C}(t) \end{bmatrix}}_{\mathbf{Q}(t)} \begin{Bmatrix} v(t-\tau) \\ u(t-\tau) \\ x(t-\tau) \\ y(t-\tau) \end{Bmatrix} \\
 &- a \underbrace{\begin{bmatrix} \mathbf{E}(t) & \mathbf{F}(t) \\ \mathbf{W}^{-1}(t)\mathbf{E}(t) & \mathbf{W}^{-1}(t)\mathbf{F}(t) \end{bmatrix}}_{\mathbf{J}(t)} \begin{Bmatrix} \dot{v}(t) \\ \dot{u}(t) \\ \dot{x}(t) \\ \dot{y}(t) \end{Bmatrix}
 \end{aligned} \tag{5-17}$$

Calculation of the relationship between vibrations and dynamic forces are summarized in block diagram in Figure 5-2. Note that the sub-matrices $(\mathbf{W}^{-1}(t)\mathbf{C}(t))$ and $\mathbf{W}^{-1}(t)\mathbf{F}(t)$, which relate the forces on the workpiece to the workpiece vibrations, are periodic at the tooth passing period.

The remaining sub-matrices are periodic at the spindle; hence, the matrices $\mathbf{P}(t)$, $\mathbf{Q}(t)$ and $\mathbf{J}(t)$ are periodic at spindle period $(N\tau)$ in time domain or 2π intervals in angular domain.

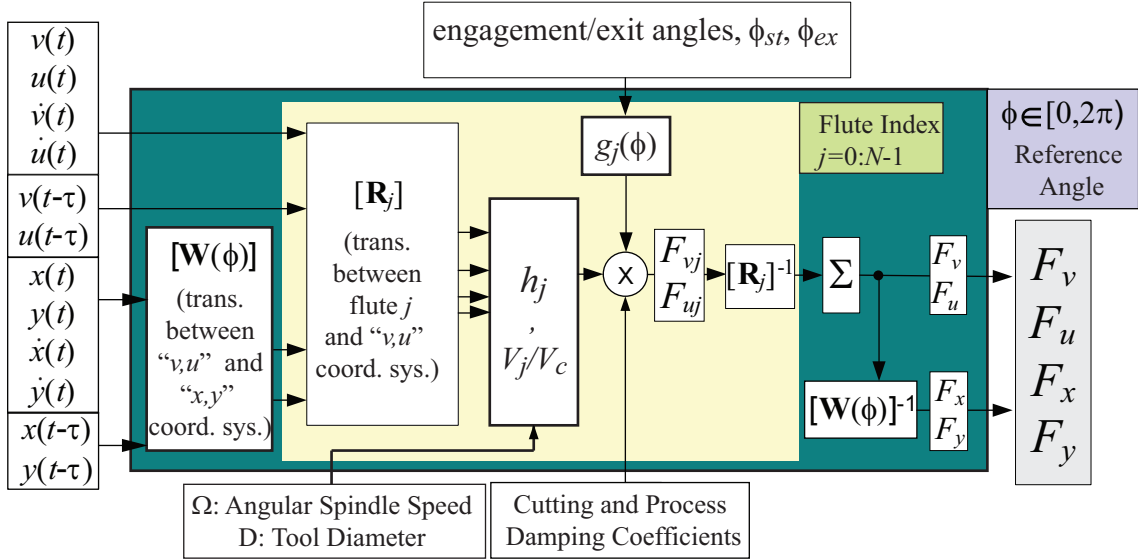


Figure 5-2: Calculation of relationship between forces and vibrations

5.3 Structural Dynamic Model

The vibrations of the workpiece are expressed in the stationary Cartesian coordinate system as:

$$\begin{Bmatrix} x(s) \\ y(s) \end{Bmatrix} = [\Phi]_W \begin{Bmatrix} F_x(s) \\ F_y(s) \end{Bmatrix} \Rightarrow [\Phi]_W = \begin{bmatrix} \Phi_{xx}(s) & \Phi_{xy}(s) \\ \Phi_{xy}(s) & \Phi_{yy}(s) \end{bmatrix} \quad (5-18)$$

where the transfer functions are expressed in the form:

$$\Phi_{pq}(s) = \sum_{l=1}^{K_l} \left(\frac{\omega_{nl}^2 / k_l}{s^2 + 2\zeta_l \omega_{nl} s + \omega_{nl}^2} \right) \quad p, q \in \{x, y\} \quad (5-19)$$

The natural frequency (ω_{nl}), damping ratio (ζ_l) and stiffness (k_l) of mode l in pq direction are identified experimentally from modal tests on the workpiece or non-rotating parts of the machine such as its column.

The dynamic forces in the rotating coordinate system must include inertial forces due to the rotation of the non-inertial rotating coordinate system as:

$$\begin{aligned}
 \begin{Bmatrix} F_v(t) \\ F_u(t) \end{Bmatrix} &= \begin{bmatrix} k_v + c_v \frac{d}{dt} + m_v \frac{d^2}{dt^2} & 0 \\ 0 & k_u + c_u \frac{d}{dt} + m_u \frac{d^2}{dt^2} \end{bmatrix} \begin{Bmatrix} v(t) \\ u(t) \end{Bmatrix} \\
 &+ \begin{bmatrix} -\Omega^2 m_v & -2\Omega m_v \frac{d}{dt} \\ 2\Omega m_u \frac{d}{dt} & -\Omega^2 m_u \end{bmatrix} \begin{Bmatrix} v(t) \\ u(t) \end{Bmatrix}
 \end{aligned} \tag{5-20}$$

where (m_v, m_u) , (k_v, k_u) and (c_v, c_u) are equivalent lumped mass, stiffness and damping values in the principal dynamic directions (v, u) , respectively. The transfer function in the rotating coordinate system is obtained by using Laplace transformation and matrix inversion of Eq. (5-20):

$$\begin{aligned}
 \begin{Bmatrix} v(t) \\ u(t) \end{Bmatrix} &= \Phi_{vu} \begin{Bmatrix} F_v(t) \\ F_u(t) \end{Bmatrix} \\
 \Rightarrow \\
 \Phi_{vu} &= \begin{bmatrix} k_v + c_v s + m_v s^2 - \Omega^2 m_v & -2\Omega m_v s \\ +2\Omega m_u s & k_u + c_u \frac{d}{dt} + m_u s^2 - \Omega^2 m_u \end{bmatrix}^{-1}
 \end{aligned} \tag{5-21}$$

The vibrations in the rotating and fixed coordinate systems are combined as:

$$\begin{Bmatrix} v(s) \\ u(s) \\ x(s) \\ y(s) \end{Bmatrix} = \underbrace{\begin{bmatrix} [\Phi]_{vu} & [0] \\ [0] & [\Phi]_w \end{bmatrix}}_{\Phi(s, \Omega)} \begin{Bmatrix} F_v(s) \\ F_u(s) \\ F_x(s) \\ F_y(s) \end{Bmatrix} \tag{5-22}$$

5.4 Stability of the System

The dynamic milling system expressed in Eq. (5-17) is simulated numerically in time domain as:

$$\begin{Bmatrix} F_v(t) \\ F_u(t) \\ F_x(t) \\ F_y(t) \end{Bmatrix} = -a\mathbf{P}(t) \begin{Bmatrix} v(t) \\ u(t) \\ x(t) \\ y(t) \end{Bmatrix} + a\mathbf{Q}(t) \begin{Bmatrix} v(t-\tau) \\ u(t-\tau) \\ x(t-\tau) \\ y(t-\tau) \end{Bmatrix} - a\mathbf{J}(t) \begin{Bmatrix} \dot{v}(t) \\ \dot{u}(t) \\ \dot{x}(t) \\ \dot{y}(t) \end{Bmatrix} \quad (5-23)$$

The vibration vector is calculated from Eq. (5-22) considering the transfer matrices and dynamic cutting forces in state space. The numerical solution considers the time-varying directional matrices ($\mathbf{P}(t), \mathbf{Q}(t), \mathbf{J}(t)$). However, the numerical solution is not computationally efficient, thus analytical stability analysis is preferred either using the semi-discrete time domain solution method of Insperger and Stepan [21], or the Nyquist stability criterion by averaging directional matrices similar to the stability law for the dynamic milling case presented by Altintas and Budak [3]; the later approach is selected henceforth:

$$\bar{\mathbf{P}} = \frac{1}{N\tau} \int_0^{N\tau} \mathbf{P}(t) dt, \bar{\mathbf{Q}} = \frac{1}{N\tau} \int_0^{N\tau} \mathbf{Q}(t) dt, \bar{\mathbf{J}} = \frac{1}{N\tau} \int_0^{N\tau} \mathbf{J}(t) dt \quad (5-24)$$

The averaging procedure approximates the dynamics of milling as a time invariant system and the $\bar{\mathbf{P}}$, $\bar{\mathbf{Q}}$ and $\bar{\mathbf{J}}$ matrices and their detailed derivations are discussed in the Appendix C. The resulting time invariant dynamic system is expressed in the Laplace domain as:

$$\begin{Bmatrix} F_v(s) \\ F_u(s) \\ F_x(s) \\ F_y(s) \end{Bmatrix} = a \left(-\bar{\mathbf{P}} + e^{-s\tau} \bar{\mathbf{Q}} - s\bar{\mathbf{J}} \right) \begin{Bmatrix} v(s) \\ u(s) \\ x(s) \\ y(s) \end{Bmatrix} \quad (5-25)$$

Transfer functions of the displacements are incorporated into the dynamic milling forces (Eq.(5-25)) in the Laplace domain as:

$$\begin{aligned}
 \begin{Bmatrix} F_v(s) \\ F_u(s) \\ F_x(s) \\ F_y(s) \end{Bmatrix} &= a(-\bar{\mathbf{P}} + e^{-s\tau}\bar{\mathbf{Q}} - s\bar{\mathbf{J}}) \underbrace{\begin{bmatrix} [\Phi]_{vu} & [0] \\ [0] & [\Phi]_{w} \end{bmatrix}}_{\Phi(s, \Omega)} \begin{Bmatrix} F_v(s) \\ F_u(s) \\ F_x(s) \\ F_y(s) \end{Bmatrix} \\
 \Rightarrow & \\
 \left[\mathbf{I}_{4 \times 4} + a(\bar{\mathbf{P}} - e^{-s\tau}\bar{\mathbf{Q}} + s\bar{\mathbf{J}}) \Phi(s, \Omega) \right] \begin{Bmatrix} F_v(s) \\ F_u(s) \\ F_x(s) \\ F_y(s) \end{Bmatrix} &= \mathbf{0}_{4 \times 1}
 \end{aligned} \tag{5-26}$$

Therefore, this system has the following characteristic equation:

$$\det\left(\mathbf{I}_{4 \times 4} + a(\bar{\mathbf{P}} - e^{-s\tau}\bar{\mathbf{Q}} + s\bar{\mathbf{J}}) \Phi(s, \Omega)\right) = 0 \tag{5-27}$$

Since the matrices in the characteristic equation depend on the tooth period (τ) and cutting speed (V_c), the stability of the system at a given spindle speed, and the axial and radial depth of cut is checked via Nyquist stability criterion in frequency domain by substituting $s = i\omega_c$, where ω_c is a possible chatter frequency around the natural frequencies of the structure. By scanning the cutting conditions (i.e. speeds and depth of cuts), the chatter stability charts are constructed. If the structural dynamics of the rotating cutter and process damping terms are neglected, the Eq.(5-27) is then reduced to the speed independent characteristic equation of stationary dynamic systems formulated by Budak and Altintas [9] as proven in Appendix C.2.

5.5 Simulation and Experimental Results

Sample numerical simulations and milling experiments were conducted to validate the proposed stability model. A carbide tipped end mill with two inserts was used to cut AISI1045 steel with 21 HRC hardness (Figure 5-3). The workpiece was attached to a

force dynamometer which was considerably more rigid than the rotating cutter; hence, its flexibility was ignored in the stability prediction. The structural dynamic parameters of the rotating cutter, cutting force and process damping coefficients of the tool-workpiece pair are given in Table 5-1. Cutting force coefficients were identified mechanistically from vibration free cutting tests as described in [2]. The measured and predicted cutting forces were in agreement as shown in Figure 5-4, which indicates the validity of cutting force coefficients used in the stability prediction. The process damping coefficients were obtained experimentally by indenting the insert to the work material as presented in [15]. The chatter stability lobes were predicted and compared against slot milling experiments as shown in Figure 5-5. It must be noted that the process damping zone is highly sensitive to flank wear; therefore, an average measured flank wear of $130\mu\text{m}$ was maintained in chatter tests. The critical axial depth of cut was limited to about only 0.25mm at spindle speeds beyond 1500rev/min, but it reached 2mm at low spindle speeds. The cutter has identical natural frequencies (665 Hz) in two principal directions but with different modal stiffness. Due to rotational dynamics, directional factors and process damping, the chatter occurred at 776Hz with a 0.5mm axial depth of cut and 3580rev/min spindle speed (i.e. tooth passing frequency of 112.7Hz) while the milling process was stable at a depth of cut of 2mm and 1250rev/min spindle speed.



Figure 5-3: Setup for milling stability test

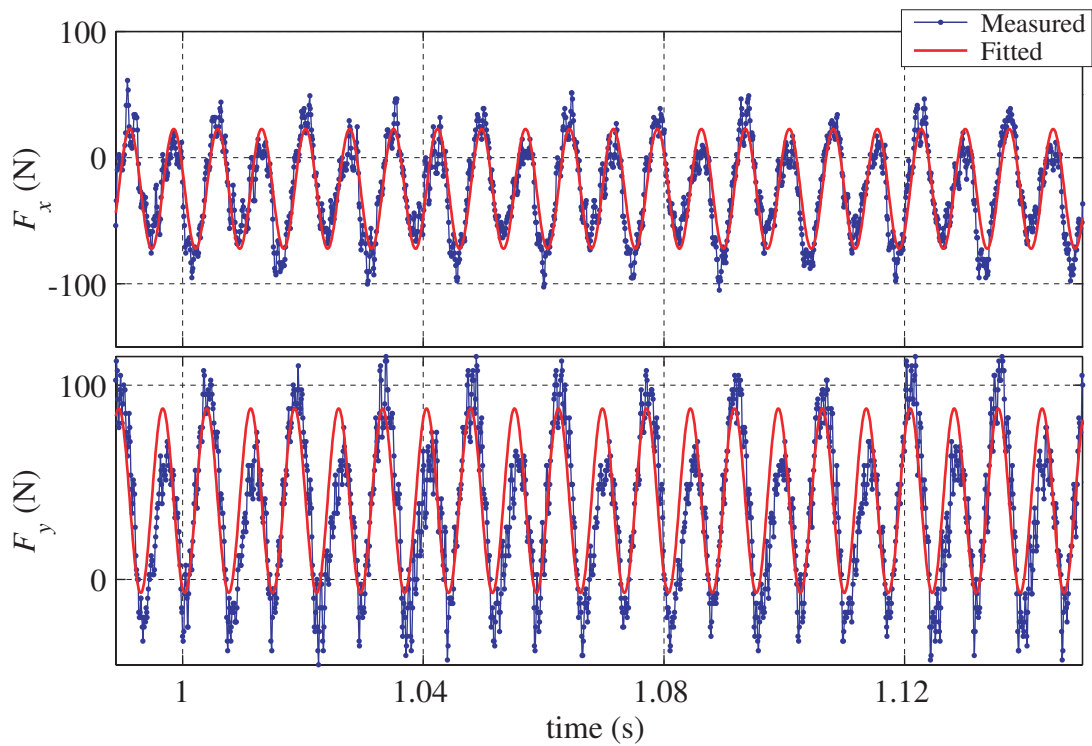


Figure 5-4: Predicted and measured milling forces in slot milling of AISI1045 steel. Cutting conditions: Spindle speed: 4297 rev/min, depth of cut: 0.25 mm, feed-rate= 0.1 mm/flute, number of inserts=2. Cutting coefficients are given in Table 5-1.

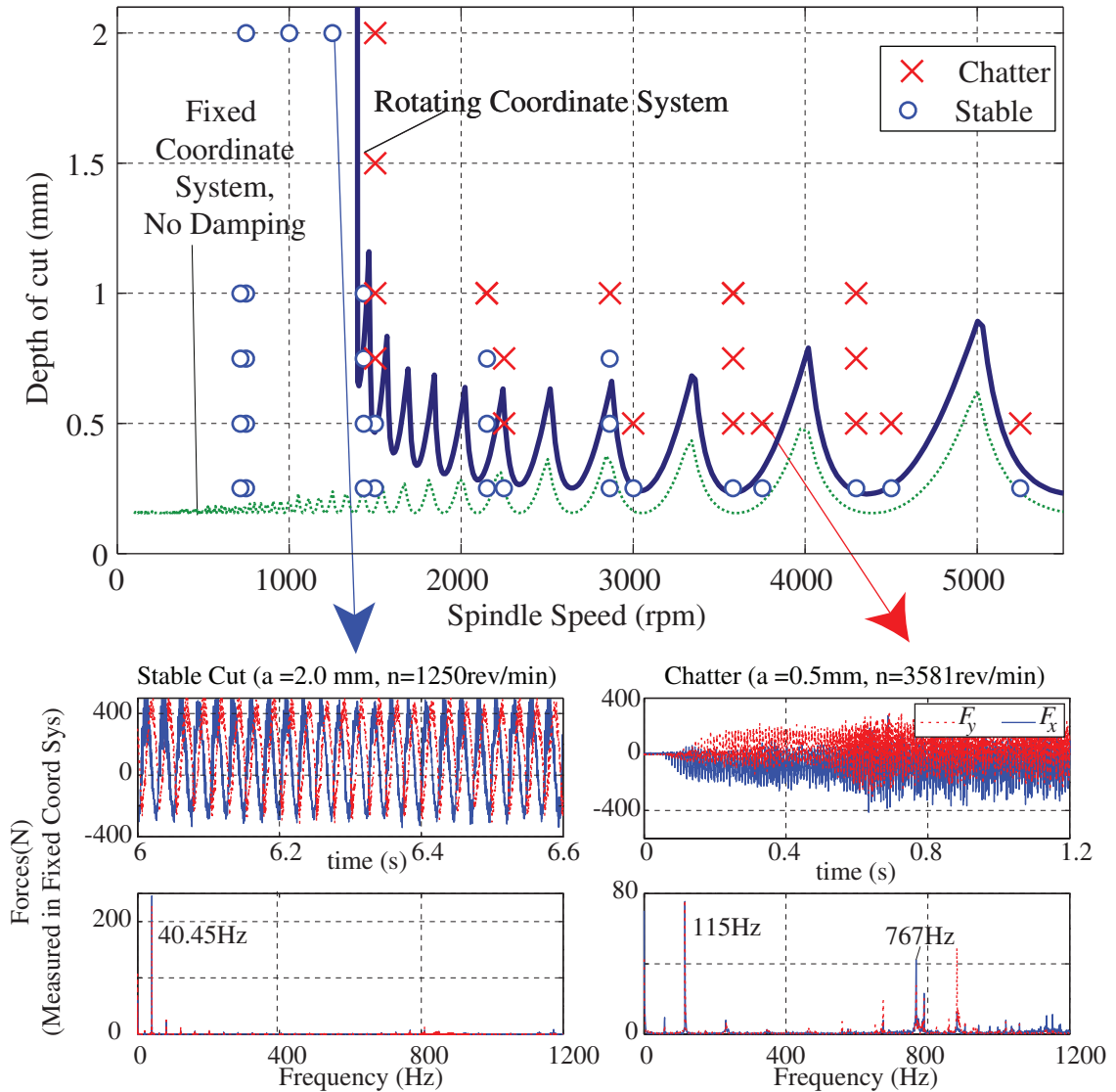


Figure 5-5: Predicted and measured chatter stability results in slot milling of AISI 1045 steel with a two teeth cutter. Cutting conditions and parameters are given in Table 5-1

Table 5-1: Parameters used in slot milling of AISI 1045 steel with R390-020A20L-11L tool holder having 2 R390-11 T302E-PM-4240 inserts.

Modal parameters	Cutting Force Coefficients	Process Damping Coefficients
$k_u = 8.16 \text{ N}/\mu\text{m}$, $\omega_{nu} = 665 \text{ Hz}$, $\zeta_u = 0.023$ $k_v = 5.22 \text{ N}/\mu\text{m}$, $\omega_{nv} = 665 \text{ Hz}$, $\zeta_v = 0.023$	$K_{rc} = 778 \text{ MPa}$ $K_{tc} = 1877 \text{ MPa}$	$K_{sp} = 4.0 \times 10^{13} \text{ N}/\text{m}^3$ $l_w = 130 \mu\text{m}$, $\mu_c = 0.9$ $C_t = \mu_c \frac{l_w^2}{2} K_{sp} = 0.30 \text{ N}/\mu\text{m}$ $C_r = \frac{l_w^2}{2} K_{sp} = 0.34 \text{ N}/\mu\text{m}$

A numerical model of the proposed dynamic milling system was developed to study the stability of the system without the averaging of time varying directional factors as was done in analytical prediction. An asymmetric structure was selected in order to illustrate the effect of rotating dynamics on the stability of the system. The analytical stability charts predicted in rotating and fixed coordinate systems are shown in Figure 5-6. The dotted stability limit was obtained when the tool was assumed to be rigid, and the workpiece was assigned to have flexible modes in the fixed coordinate system. The same modal parameters were given to the tool in the rotating coordinate system while the workpiece was assumed to be rigid to obtain the stability limit shown by solid line. The analytical stability charts predicted in fixed and rotating coordinate systems give contradictory stability predictions. Time domain simulations of the system with flexible tool agree well with the rotating coordinate system based stability model. Two sample simulations are presented which show the presence of chatter at 4880rev/min and a stable milling process at 5500rev/min with axial depths of cuts 0.4mm and 0.5mm, respectively. These results indicate the importance of considering the rotating structural dynamics in the prediction model when the modes are not equal in the two principal directions.

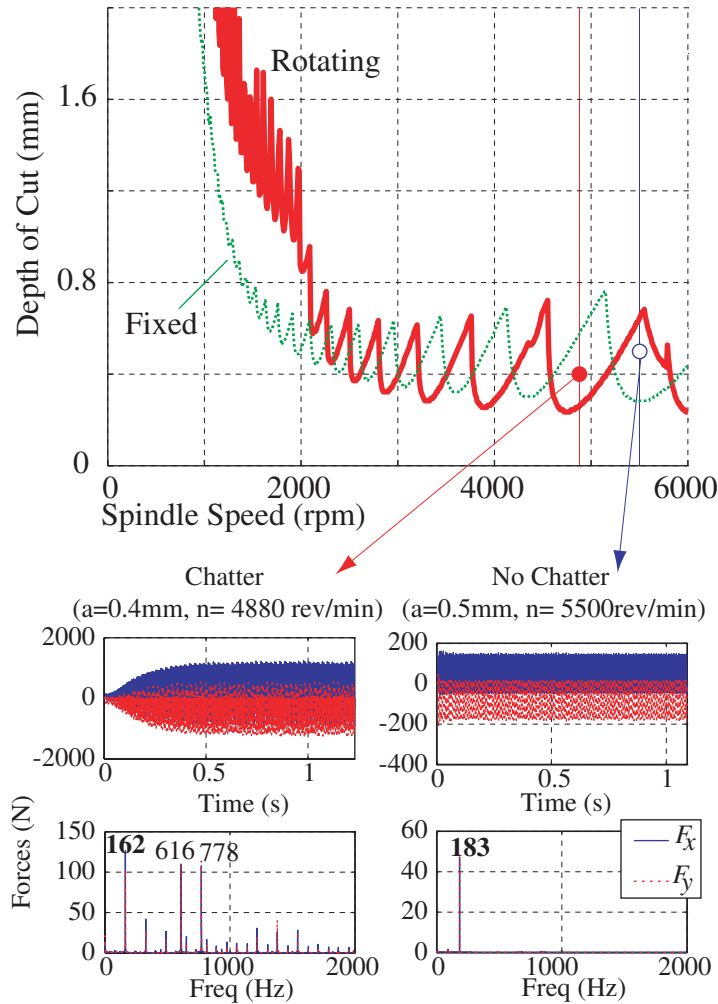


Figure 5-6: Time domain verification of analytical stability for slot milling with two inserts. (Cutting coefficients: $K_{rc} = 1978\text{MPa}$, $K_{tc} = 3242\text{MPa}$, $C_r = 0.61\text{N}/\mu\text{m}$, $C_t = 0.18\text{N}/\mu\text{m}$; modal parameters: $k_u = 15.7\text{N}/\mu\text{m}$, $\omega_{nu} = 1152\text{Hz}$, $\zeta_u = 0.023$; $k_v = 5.22\text{N}/\mu\text{m}$, $\omega_{nv} = 665\text{Hz}$, $\zeta_v = 0.023$)

The stability of several cases with symmetric and non-symmetric structural dynamic characteristics was predicted analytically in stationary and rotating coordinate systems, as seen in Figure 5-7. When the system has symmetric dynamics ($k_u = k_v$, $\omega_u = \omega_v$), the stability limit predictions are different for tools with one or two flutes, but both models give the same stability results for a five-flute tool. For an asymmetric tool with stiffness difference in u and v directions, the stability limits are predicted differently for tools with one or two flutes while they stay the same for the five-flute tool. When the number

of flutes increases, the effect of time-varying directional factors, which are more accurately considered in rotating coordinate system, diminishes. When the natural frequencies are different in the two principal (u, v) directions and independent of the number of flutes, the predicted stability charts with rotating coordinate system and fixed coordinate system have peaks and valleys at different spindle speeds. This indicates the importance of using rotating coordinate system model in finding the stability lobes accurately, when the asymmetric rotating tool has different natural frequencies in orthogonal directions.

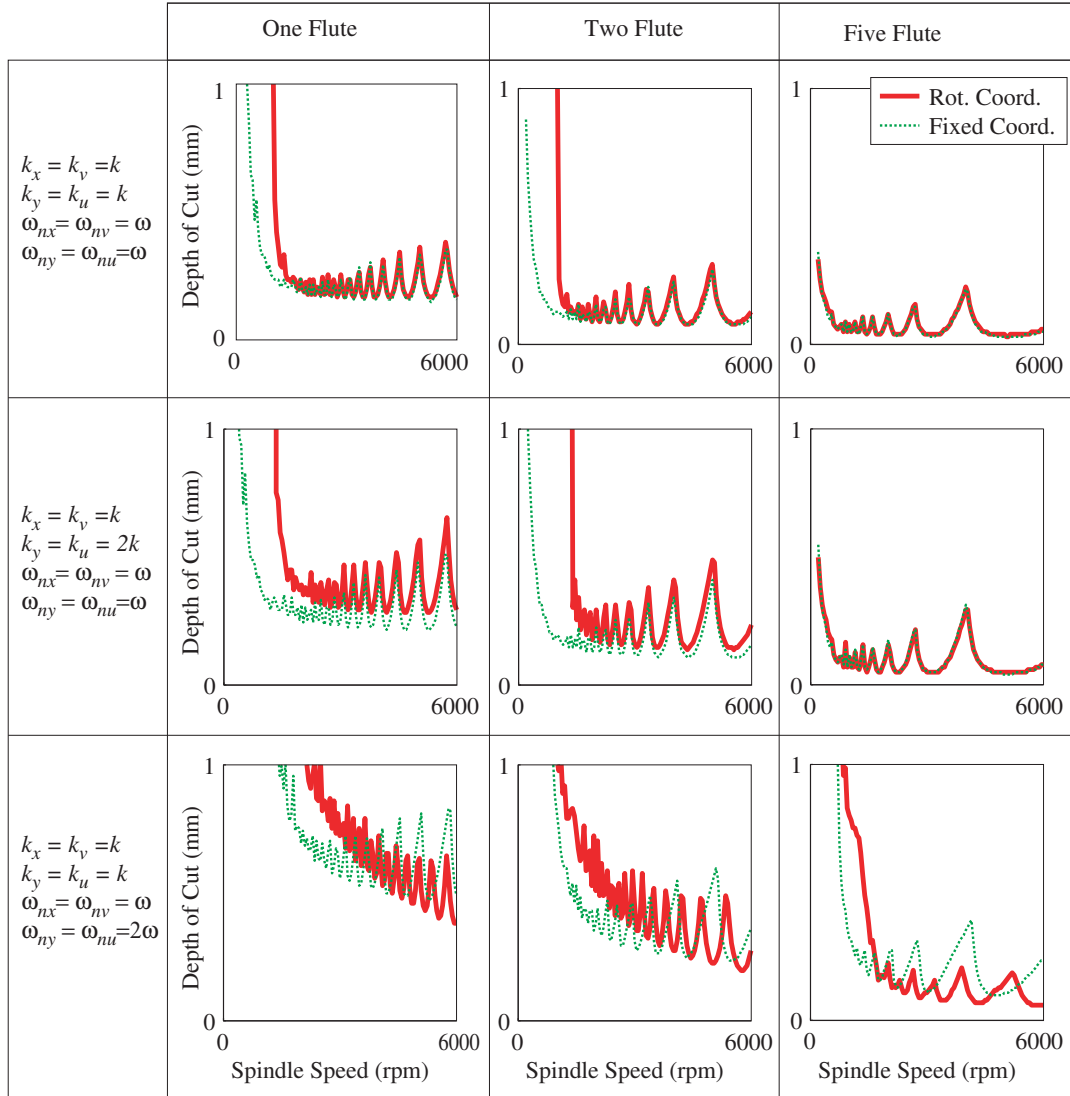


Figure 5-7: Sensitivity of stability charts to structural dynamic parameters of the system. Simulation conditions are same as Figure 5-6 except the following modal parameters are used: $k = 5.22\text{N}/\mu\text{m}$, $\omega = 2\pi \times 655\text{Hz}$, $\zeta = 0.023$

5.6 Conclusion

Machine tools have both fixed and rotating structures which contribute to chatter during machining. The chapter presents a dynamic milling model which considers the structural dynamics of both rotating and fixed modes along with a process damping model based on the contact between the tool's flank and the wavy surface finish. The structural dynamics of the rotating systems are defined in two principal directions which rotate with the

cutter. A rotating coordinate frame attached to the cutter considers the changes in directional factors of both cutting forces and resulting vibrations as spindle rotates. The fixed coordinate system assumes that the direction of structural modes remains constant, which is applicable to the systems where the structure is fixed (i.e. machine tool body and workpiece) or the rotating system has symmetric dynamics. The proposed dynamic model can be extended to boring, reaming and mill-turn operations with asymmetric rotating structures.

Chapter 6: Conclusion and the Future Works

6.1 Conclusions

The main objective of this thesis is to improve chatter stability limit prediction in turning and milling operations. The research started with the study of process damping mechanism in simple orthogonal cutting, then it was extended to the areas of three-dimensional turning with tools having nose radii and milling with dynamically asymmetric rotating tools. In both milling and turning cases, process damping effect was considered. The contributions of this thesis are listed in the following three main categories:

6.1.1 Process damping mechanism

The physics of process damping has been debated among scientists and several theories have been suggested to explain the phenomenon in the past. The fundamental difficulty has been the separation of process damping effect from the regeneration of chip in measuring dynamic cutting forces. A new experimental approach has been introduced in this research to cancel the effect of regeneration by creating waves in phase in successive spindle rotations. The vibration is introduced via a piezo-driven fast tool servo synchronized with the integer multiples of spindle's rotation frequency. The process damping force is extracted and the coefficient of damping contributed by wave cutting is identified in frequency domain. The relationship between the process damping effect and tool wear has been demonstrated with the experimental set up and the proposed model.

The scholarly contribution has been published in CIRP Annals, Manufacturing Technology [4].

6.1.2 Stability of three dimensional turning

The rate of changes in the dynamic cutting forces with respect to displacements is only determined with a cutting coefficient and the width of cut in orthogonal cutting models. However, the nose radius, approach angle of the tool, and feed per revolution affect the process dynamics and stability of most turning operations. In addition, the structure could be flexible in several directions and create cross-coupling between depth of cut, feed and cutting speed directions. A new dynamic turning model and analytical stability limit prediction method are introduced in chapter 4. The proposed model is experimentally validated to demonstrate its capability of predicting chatter stability limits for turning tools having nose radius and arbitrary approach angle. Process damping effect is also included in the model by considering the contribution of differential lengths of cutting edges when the tool moves with respect to the workpiece and compresses work material under its worn flank. Stability limit predictions have been favourably compared with the experimental results conducted at low speed ($V_c \approx 25\text{m/min}$) and high speed ($V_c \approx 350\text{m/min}$) cutting tests. The scholarly contributions are published in the Transactions of ASME, Journal of Manufacturing Science and Technology [15].

6.1.3 Stability of milling with rotating cutter dynamics at process damping speeds

The milling stability prediction model of Altintas and Budak [3] has been improved by including process damping effects and the effects of a rotating tool with asymmetric

dynamics in this thesis. While researchers were aware of process damping effects in milling [20], there has not been a previous work for analytical prediction of stability limit in the presence of process damping. In addition, the effects of asymmetry on dynamics of a rotating tool were ignored; so its dynamics could be studied in a fixed coordinate system. In chapter 5, the general dynamics of milling with four degrees of freedom is introduced which considers process damping and both the dynamics of flexible and symmetric or asymmetric tools, as well as flexible work holding systems with stationary dynamics. It is shown that the effects of asymmetric modes are important in predicting the chatter limits. A paper summarizing the contributions in milling dynamics has been submitted for publication in August 2009 to ASME Journal of Manufacturing Science and Technology [16].

6.2 Future Works

Process damping coefficient was extracted from oscillation test or indentation tests as suggested by previous researchers[49]; however, extraction of these coefficients from more basic material properties such as Young's modulus and Poisson's ratio would make application of process damping model more convenient for various materials. Stability of three-dimensional turning was investigated in chapter 4 assuming a tool with a completely round nose section and negligible inclination and rake angles. As inclination angle would affect the direction of chip flow, a more sophisticated method may become necessary to predict stability limit with acceptable errors. An additional improvement could come from allowing more generalized cutting edge geometry, similar to those in wiper tools, which have complex cutting edge geometry to minimize machined surface's

roughness, rather than a simple circular arc connected to two straight lines as major and minor cutting edges.

In case of milling, the industry uses tools with complex features, such as tapered geometry, round nose (ball end mills and bull end mills), non-constant pitch and serrations. It would be worthwhile to add the process damping effect to the mathematical models that are used for stability limit prediction in these tools.

Bibliography

- [1] Albrecht, P., 1960, “New Developments in the Theory of the Metal Cutting Process, Part I: The Ploughing Process in Metal Cutting”, Transactions of the ASME, Journal of Engineering for Industry. **82**(11), pp. 348-358.
- [2] Altintas, Y., “Manufacturing Automation, Metal Cutting Mechanics, Machine Tool Vibrations, and CNC Design”, Cambridge University Press, 2000.
- [3] Altintas, Y., Budak, E., 1995, “Analytical Prediction of Stability Lobes in Milling”, CIRP Annals, **44**(1), pp. 357–362.
- [4] Altintas, Y., Eynian, M., Onozuka, H., 2008, “Identification of Dynamic Cutting Force Coefficients and Chatter Stability with Process Damping”, CIRP, **57**(1), pp.371-374.
- [5] Altintas, Y., Weck, M., 2004, “Chatter Stability in Metal Cutting and Grinding”, Annals of CIRP, Key Note Paper of STC-M, **53**(2), pp. 619-642.
- [6] Armarego, E.J.A. and Samaranayake, P., 1999 , “Performance prediction models for turning with rounded corner plane faced lathe tools II. Verification of model”, Machining Science and Technology **3**(2) (1999), pp. 173–200.
- [7] Arnold, R. N. “The Mechanism of tool vibration in the cutting of steel”, Proceedings of institution of mechanical engineers, vol.**54**, pp. 261-284, 1946.
- [8] Atabey, F., “Modeling of mechanics and dynamics of boring”, MSc Thesis, University of British Columbia, 2001.

-
- [9] Budak, E., Altintas Y., 1998, “Analytical prediction of chatter stability in milling- Part I: General Formulation”, *Journal of dynamic systems, measurement, and control*, **120**(1), pp. 22-30.
- [10] Chiou, R. Y., Liang, S.Y., 1998, “Chatter Stability of a Slender Cutting Tool in Turning with Wear Effect”, *International Journal of Machine Tools and Manufacture*, **38**(4), pp.315-327.
- [11] Clancy, B. E., Shin, Y.C., 2002, “A Comprehensive Chatter Prediction Model for Face Turning Operation Including the Tool Wear Effect”, *International Journal of Machine Tools and Manufacture*, **42**(9), pp.1035-1044.
- [12] Colwell L. V., 1954, “Predicting the Angle of Chip Flow for Single Point Cutting Tools”, *Transactions of the ASME*, **76**, pp. 199-204.
- [13] Das, M. K., Tobias, S. A., 1967, “The Relation between the Static and the Dynamic Cutting of Metals”, *International Journal of Machine Tool Design and Research*, **7**, pp. 63-89.
- [14] Doi, S, and S Kato, 1956, “Chatter vibration of lathe tools”, *Transactions of ASME*.
- [15] Eynian, M. Altintas, Y., 2009, “Chatter Stability of General Turning Operations with Process Damping”, *ASME Journal of Manufacturing Science and Engineering*, August 2009, **131**, 041005.
- [16] Eynian, M., Altintas, Y., 2009, “Analytical Chatter Stability of Milling with Rotating Cutter Dynamics at Process Damping Speeds”, Submitted to the *ASME Journal of Manufacturing Science and Technology*.

-
- [17] Hahn, R. S., 1946, "Metal cutting chatter and its elimination", Transactions of ASME, Journal of engineering for industry, **75**, pp. 1073-1080.
- [18] Hoshi, T., 1972, "Cutting Dynamics Associated with Vibration Normal to Cut Surface", Annals of the CIRP, **21**(1), pp. 101-102.
- [19] Hu, R. S., P. Mathew, P. L. B. Oxley and H. T. Young, 1986, "Allowing for end Cutting Edge Effects in predicting Forces in Bar turning with oblique machining conditions", Proceedings of the Institution of Mechanical Engineers, Mechanical engineering science, Part C **200** (2), pp. 89-99.
- [20] Huang, C. Y., Wang, J.J.J., 2007, "Mechanistic Modeling of Process Damping in Peripheral Milling", Transactions of the ASME, Journal of Manufacturing Science and Engineering, **129**(1), pp.12-20.
- [21] Insperger, T., Mann, B. P., Stépán, G. , and Bayly, P. V., 2003, "Stability of up-milling and down-milling, part 1: alternative analytical methods", International Journal of Machine Tools and Manufacture, **43**, pp. 25-34.
- [22] Jawahir, I. S., 1991, "An investigation of three-dimensional chip flow in machining of steels with grooved chip forming tool insert", Transactions of NAMRC, **19**, pp. 222-231.
- [23] Kegg, R. L., 1965, "Cutting Dynamics in Machine tool Chatter, Contribution to Machine tool Chatter Research 3", Transactions of the ASME, Journal of Engineering for Industry, pp. 464-470.
- [24] Lazoglu, I., Atabey, F., Altintas, Y., 2002, "Dynamics of Boring Processes: Part III-Time Domain Modeling", Journal of Machine Tools and Manufacture, **42**(14), pp. 1567-1576.

-
- [25] Li, C. J., Ulsoy, A. G., Endres, W. J., 2003, “The effect of flexible-tool rotation on regenerative instability in machining”, *Journal of manufacturing science and engineering*, **125**, pp. 39-47.
- [26] Merritt, H. E., 1965 “Theory of self-excited Machine-Tool Chatter”, *ASME Journal of Engineering for Industry*, **87**, pp. 447-454.
- [27] Minis, I., Yanushevsky, T., Tembo, R., and Hocken, R., 1990, “Analysis of Linear and Nonlinear Chatter in Milling”, *CIRP Annals*, **39**, pp. 459–462.
- [28] Minis, I.E., Magrab, E.B., Pandelidis, I.O., 1990, “Improved Methods for the Prediction of Chatter in Turning, Part 3: A Generalized Linear Theory” *ASME Journal of Engineering for Industry*, **112**(1), pp. 28–35.
- [29] Montgomery, D., Altintas, Y., 1991, “Mechanism of Cutting Force and Surface Generation in Dynamic Milling”, *Transactions of the ASME, Journal of Engineering for Industry*, **113**(5), pp. 160-168.
- [30] Muszynska, A., 2005, *Rotordynamics*, Taylor Francis, Boca Raton.
- [31] Olgac, N., Zhao, G., 1987, “A relative stability study on the dynamics of the turning mechanism”, *Transaction of ASME* **109**, pp. 164–170.
- [32] Opitz H. and F. Bernardi, 1970, “Investigation and calculation of the chatter behaviour of lathes and milling machines”, *Annals of the CIRP*, **XVIII**, pp. 335-343,.
- [33] Ozlu, E., Budak, E., 2007, “Analytical Modeling of Chatter Stability in Turning and Boring Operations, Part II: Experimental Verification”, *Journal of Manufacturing Science and Engineering*, **129**(4), pp. 733-739.

-
- [34] Peters, J, Vanherck, P., Van Brussel, H., 1971, “The Measurement of the Dynamic Cutting Coefficient”, *Annals of the CIRP*, **21**(2), pp. 129-136.
- [35] Rao, B. C. and Y. C. Shin, 1999, “A comprehensive dynamic cutting force model for chatter prediction in turning”, *International Journal of Machine Tools and Manufacture*, **39**, pp. 1631-1654.
- [36] Reddy, R. G., Ozdoganlar, O. B., Kapoor, S. G., DeVor, R. E., and Liu, X., 2002, “A Stability Solution for the Axial Contour-Turning Process”, *ASME Journal of Manufacturing Science and Engineering*, **124**(3), pp. 581-587.
- [37] Schmitz, T. L., Ziegert, J., Stanislaus, 2004, C., “A method for predicting chatter stability for systems with speed-dependent spindle dynamics”, Schmitz, T.; Ziegert, J.; Stanislaus, C. SME technical paper TP04PUB182, *Transactions of NAMRI/SME*, **32**, pp.17–24.
- [38] Sisson, T. R. and R.L. Kegg, 1969, “An Explanation of Low Speed Chatter Effects”, *Transactions of ASME, Journal of Engineering for Industry*, **91**(4), pp. 951-955,.
- [39] Sridhar, R., Hohn, R. E., and Long, G. W., 1968, “A Stability Algorithm for the General Milling Process—Contribution to Machine Tool Chatter Research—7”, *ASME Journal of Engineering for Industry*, pp. 330–334.
- [40] Smith, S., Tlusty, J., 1997, “Current trends in high-speed machining”, *Transactions of the ASME, Journal of manufacturing Science and Engineering*, **119**, pp. 664-666.
- [41] Tlusty, J., 1978 “Analysis of state of research in cutting dynamics”, *Annals of the CIRP, Manufacturing Technology*, **27**, pp. 583-589.

-
- [42] Tlusty, J. and M. Polacek, 1963, "The stability of machine tool against self excited vibrations in machining", International research in production engineering, ASME, pp. 465-474.
- [43] Tlusty, J., 1970, "Machine Tool Structures: The Theory of Chatter and Stability Analysis", Edited by Koenigsberger, F. and Tlusty, Section 2, pp. 115-274. .
- [44] Tlusty, J., Ismail, F., 1981, "Basic Nonlinearity in Machining Chatter", Annals of the CIRP, **30/1**, pp. 299-304.
- [45] Tlusty, J., Zaton, W., Ismail, F., 1983, "Stability lobes in milling" Annals of the CIRP.
- [46] Tobias, S.A. and W. Fishwick, 1958, "A theory of regenerative chatter", The engineer- London.
- [47] Usui, E., A. Hirota, M. Masuko, 1978, "Analytical Prediction of three dimensional cutting process - Part 1, Basic Cutting Process", Transactions of the ASME, **100**, pp. 222-228.
- [48] Wallace, P. W., Andrew, C., 1965, "Machining Forces: Some Effects of Tool Vibration", Journal of mechanical engineering science, **7**, pp.152-162.
- [49] Wu, D. W., 1989, "A new approach of formulating the transfer function for dynamic cutting processes", Transactions of the ASME, Journal of Engineering for industry, 111(2), pp. 37-47.
- [50] Zhu W. H., M.B. Jun and Y. Altintas, 2001, "A fast tool servo design for precision turning of shafts on conventional CNC lathes", International Journal of Machine Tools and Manufacture, **41**, pp. 953-965.
- [51] Zorev, N. N, 1966, Metal Cutting Mechanics, Pergamon, Oxford.

APPENDICES

Appendix A: Nyquist Stability Criterion

A.1 Application of Nyquist Stability Criterion in Chatter Problems

In this section, application of Nyquist stability criterion for stability analysis of a turning system with a characteristic equation of $CH(s) = \det \left[\mathbf{I} + \left(\mathbf{J} + \mathbf{J}_\tau e^{-s\tau} + s\mathbf{J}_v \right) \Phi(s) \right] = 0$ is presented. There is a similar approach for application of this method in the milling stability limit prediction. Poles of the characteristic equation $CH(s)$ are the poles of the structure (Φ) which are all stable. Any unstable zero of the characteristic equation $CH(s)$ creates a clockwise encirclement of the origin of complex plane by Nyquist mapping of the characteristic equation. Unstable zeros of the characteristic equation are unstable poles of the system, as the characteristic equation appears in the denominator of the input-output transfer functions in the closed loop system.

Nyquist plot is the mapping of the Nyquist contour (Figure A-1) by the characteristic equation onto a complex plane. The first part of the Nyquist contour starts from $0 - i\infty$ to $0 + i\infty$. Since the characteristic equation is a pseudo-polynomial with real coefficients, the characteristic equation is symmetric with respect to the real axis:

$$\begin{aligned} \operatorname{Re}[CH(-s)] &= \operatorname{Re}[CH(s)] \\ \operatorname{Im}[CH(-s)] &= -\operatorname{Im}[CH(s)] \end{aligned} \tag{A-1}$$

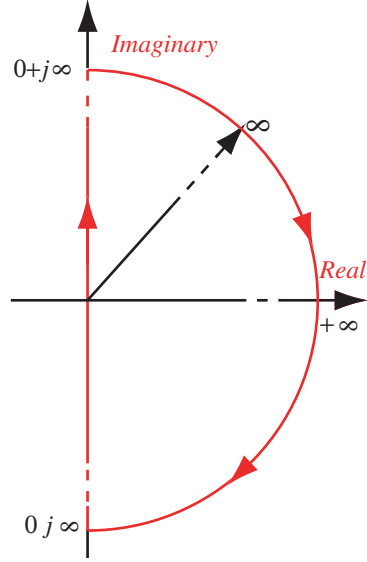


Figure A-1: Nyquist Contour

Because of this symmetry, the mapping of the only upper part of the imaginary axis is sufficient for stability prediction. On the other hand, while the highest order of s in $(\mathbf{J} + \mathbf{J}_\tau e^{-s\tau} + s\mathbf{J}_v)$ is one, the lowest order in $\Phi(s)$ is s^{-2} (second order structural dynamics); consequently, $(\mathbf{J} + \mathbf{J}_\tau e^{-s\tau} + s\mathbf{J}_v)\Phi(s) \rightarrow \frac{1}{s} \rightarrow 0$ as $|s| \rightarrow \infty$, and $\det[\mathbf{I} + (\mathbf{J} + \mathbf{J}_\tau e^{-s\tau} + s\mathbf{J}_v)\Phi(s)] \rightarrow \det(\mathbf{I}) = 1$. This means that the semicircle part of the Nyquist contour will be mapped to the point +1 on the real axis. Based on these observations, it is sufficient to count the encirclements for mapping of the positive imaginary axis. This is equivalent to replacing s with $j\omega$ where ω is a nonnegative real number.

Nyquist plot of two stable and unstable time delay systems with similar transfer functions are plotted in Figure A-2. For encirclement of the origin, a crossing of the negative real axis is necessary and would represent instability.

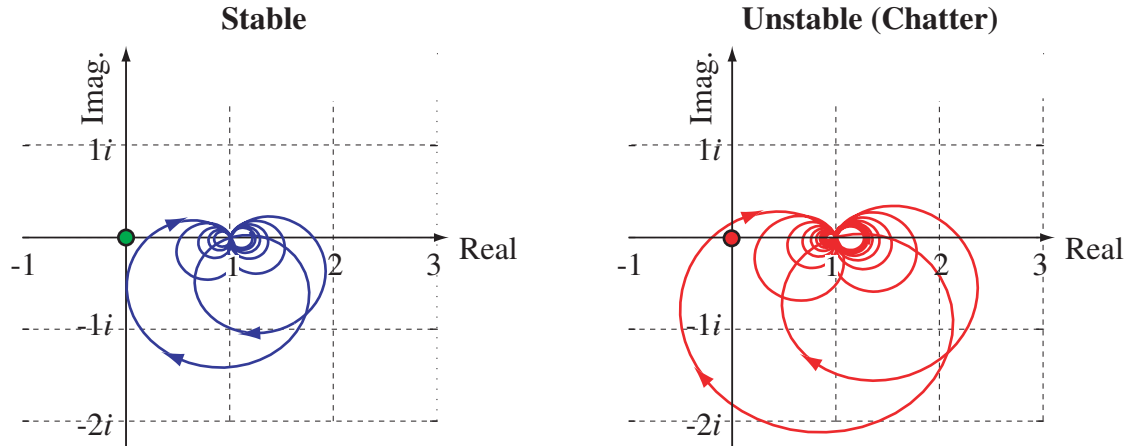


Figure A-2: Nyquist plot in stable and unstable cutting conditions

A.2 Numerical Evaluation of Stability

Nyquist contour is a continuous path; however, on a digital computer, discrete frequencies are used for Nyquist mapping. In addition, frequency response function of the machining structure $[\Phi(\omega)]$, is measured as a set of complex numbers in discrete frequencies. Thus, Nyquist plot is obtained in the form of a set of points. The following algorithm is used to access stability of a system on a digital computer:

1. Select a set of frequencies that cover the flexible modes $\omega_1, \dots, \omega_m, \dots, \omega_k$
2. set $m = 1$
3. Calculate $CH_0 = CH(j\omega_m)$
4. While $m < k$ do the following steps:
 - calculate $CH_1 = CH(j\omega_{m+1})$
 - If CH_0 is in the third quadrant of the complex plane ($\text{Re}(CH_0) < 0, \text{Im}(CH_0) < 0$) and CH_1 is in the second quadrant,

$\text{Re}(CH1) < 0, \text{Im}(CH1) \geq 0$, a crossing of the negative real axis has happened and the system is unstable.

- If $CH0$ is in the third quadrant and the $CH1$ is in the first quadrant, ($\text{Re}(CH1) \geq 0, \text{Im}(CH1) \geq 0$) calculate approximate intersection point with the real axis. A simple line interpolation method is shown to calculate the intersection point in Figure A-3. If this point has negative real part, the system is unstable. If the system is unstable, go to the step 5.
- If $m = k - 1$ then the system is stable; otherwise, increment m and go to the step 4.

5. End

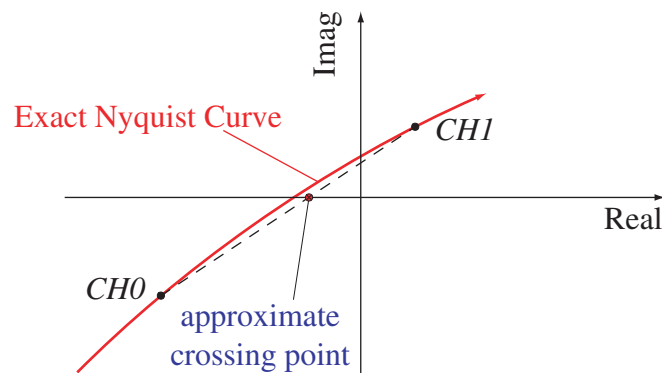


Figure A-3: Approximate Crossing Point

Appendix B: Extraction of Dynamic Cutting Coefficients from Sampled Signals

In chapter 3, oscillation cutting tests are described with the purpose of studying the nature of process damping forces. In this appendix, application of discrete time Fourier transform for extraction of dynamic cutting coefficients is discussed.

B.1 Discrete Time Fourier Transform (DTFT)

Cutting forces and tool's displacements are recorded as a series of discrete measurements. Frequency of oscillation, ω (rad/s), is known in advance but the measured cutting forces and displacements contain noise and high frequency components which are generated due to the slip-stick mechanism in chip generation and electrical noise that affects the force measurement. Discrete Time Fourier Transform (DTFT) for an infinite series $y[n]$, ($n \in \mathbb{Z}, n = -\infty \dots \infty$), is defined as:

$$Y(\omega) = \sum_{n=-\infty}^{\infty} y[n] e^{-i.n.\omega T_s} \quad (\text{B-1})$$

where ω (rad/sec) is an arbitrary frequency and T_s (sec/sample) is the sampling period of the sequence. In oscillation cutting tests, forces and displacements form a discrete series of finite length L . The finite length Discrete Time Fourier transform for these signals are obtained as:

$$\begin{aligned}
 Y(\omega) &= \sum_{n=0}^{L-1} y[n] e^{-i.n.\omega T_s} \\
 F_y(\omega) &= \sum_{n=0}^{L-1} F_y[n] e^{-i.n.\omega T_s} \\
 F_z(\omega) &= \sum_{n=0}^{L-1} F_z[n] e^{-i.n.\omega T_s}
 \end{aligned} \tag{B-2}$$

A sinusoidal displacement of the tool at the frequency ω and amplitude y_c and the corresponding dynamic cutting forces with the dynamic cutting coefficients $K_y(\omega)$ and $K_z(\omega)$ with a width of cut a will be as described below:

$$\begin{aligned}
 y[n] &= y_c \operatorname{Re}(e^{i.n.\omega T_s}) \\
 F_y[n] &= a \operatorname{Re} \left[K_y(\omega) \cdot y_c e^{i.n.\omega T_s} \right] \\
 F_z[n] &= a \operatorname{Re} \left[K_z(\omega) \cdot y_c e^{i.n.\omega T_s} \right]
 \end{aligned} \tag{B-3}$$

Therefore, the DTFT of the displacement would be

$$\begin{aligned}
 Y(\omega) &= \sum_{n=0}^{L-1} \operatorname{Re} \left[y_c e^{i.n.\omega T_s} \right] e^{-i.n.\omega T_s} \\
 &= y_c \sum_{n=0}^{L-1} \left[\cos^2 n.\omega T_s - i \cos n.\omega T_s \cdot \sin n.\omega T_s \right] \approx \frac{Ly_c}{2}
 \end{aligned} \tag{B-4}$$

Note that $\sum_{n=0}^{L-1} \cos^2(n.\omega T_s) = \frac{L}{2}$ and $\sum_{n=0}^{L-1} \sin(n.\omega T_s) \cdot \cos(n.\omega T_s) = 0$ if ω is an integer multiple of $\frac{2\pi}{LT_s}$ (sampling frequency divided to the number of samples). Even if this is

not the case, the relationships are approximately correct if $\frac{LT_s \omega}{2\pi}$ is a large number.

$F_y(\omega)$, the DTFT of F_y at frequency ω is calculated as:

$$\begin{aligned}
 F_y(\omega) &= \sum_{n=0}^{L-1} a \cdot \text{Re} \left[K_y(\omega) \cdot y_c e^{i \cdot n \cdot \omega T_s} \right] e^{-i \cdot n \cdot \omega T_s} \\
 &= \sum_{n=0}^{L-1} a \cdot y_c \cdot \text{Re} \left[(\text{Re} K_y + i \text{Im} K_y) \cdot (\cos n \cdot \omega T_s + i \sin n \cdot \omega T_s) \right] \cdot (\cos n \cdot \omega T_s - i \sin n \cdot \omega T_s) \\
 &= a \cdot y_c \cdot \sum_{n=0}^{L-1} \left[\text{Re} K_y \cos n \cdot \omega T_s - \text{Im} K_y \sin n \cdot \omega T_s \right] \cdot (\cos n \cdot \omega T_s - i \sin n \cdot \omega T_s) \quad (\text{B-5}) \\
 &= a \cdot y_c \cdot \sum_{n=0}^{L-1} \left[\text{Re} K_y \cos^2 n \cdot \omega T_s + i \text{Im} K_y \sin^2 n \cdot \omega T_s + (\dots) \sin n \cdot \omega T_s \cdot \cos n \cdot \omega T_s \right] \\
 &\approx \frac{a \cdot y_c \cdot L}{2} (\text{Re} K_y(\omega) + i \text{Im} K_y(\omega)) = \frac{a \cdot y_c \cdot L}{2} K_y(\omega)
 \end{aligned}$$

Similarly,

$$F_z(\omega) \approx \frac{a \cdot y_c \cdot L}{2} K_z(\omega) \quad (\text{B-6})$$

Therefore, the dynamic cutting coefficients are calculated from DTFT's at the frequency of oscillation as:

$$K_y(\omega) = \frac{F_y(\omega)}{aY(\omega)}, \quad K_z(\omega) = \frac{F_z(\omega)}{aY(\omega)} \quad (\text{B-7})$$

B.2 Extraction of Signal Components at the Main Oscillation

Frequency

Inverse Discrete Time Fourier transform is used to extract the displacement signal and force signals at the frequency ω shown as $y_\omega[n]$ and $F_{y\omega}[n], F_{z\omega}[n]$ here respectively:

$$\begin{aligned}
 y_\omega[n] &= \frac{2}{L} \text{Re} \left[Y(\omega) e^{i \cdot n \cdot \omega T_s} \right] \\
 F_{y\omega}[n] &= \frac{2}{L} \text{Re} \left[F_y(\omega) e^{i \cdot n \cdot \omega T_s} \right] \\
 F_{z\omega}[n] &= \frac{2}{L} \text{Re} \left[F_z(\omega) \cdot y_c e^{i \cdot n \cdot \omega T_s} \right] \quad (\text{B-8})
 \end{aligned}$$

Considering (B-7):

$$\begin{aligned}
 F_{y\omega}[n] &= \frac{2}{L} \operatorname{Re} \left[K_y(\omega) a Y(\omega) e^{i.n.\omega T_s} \right] \\
 &= \frac{2a}{L} \operatorname{Re} \left[(\operatorname{Re} K_y + i \operatorname{Im} K_y) \cdot (\operatorname{Re}[Y(\omega) e^{i.n.\omega T_s}] + i \operatorname{Im}[Y(\omega) e^{i.n.\omega T_s}]) \right] \quad (\text{B-9}) \\
 &= a \left(\operatorname{Re}[K_y] \cdot \frac{2}{L} \operatorname{Re}[Y(\omega) e^{i.n.\omega T_s}] - \operatorname{Im}[K_y] \cdot \frac{2}{L} \operatorname{Im}[Y(\omega) e^{i.n.\omega T_s}] \right)
 \end{aligned}$$

and (B-8):

$$\begin{aligned}
 y_\omega[n] &= \frac{2}{L} \operatorname{Re} \left[Y(\omega) e^{i.n.\omega T_s} \right] \\
 \dot{y}_\omega[n] &= \frac{2}{L} \operatorname{Re} \left[i \omega Y(\omega) e^{i.n.\omega T_s} \right] = -\frac{2\omega}{L} \operatorname{Im} \left[Y(\omega) e^{i.n.\omega T_s} \right] \quad (\text{B-10})
 \end{aligned}$$

After substituting (B-8) and (B-10) into (B-9), the following relationship would result:

$$F_{y\omega}[n] = a \left(\operatorname{Re}[K_y] \cdot y_\omega[n] + \operatorname{Im}[K_y] \cdot \frac{\dot{y}_\omega[n]}{\omega} \right) \quad (\text{B-11})$$

Similarly, forces in the tangential direction can be obtained as well:

$$F_{z\omega}[n] = a \left(\operatorname{Re}[K_z] \cdot y_\omega[n] + \operatorname{Im}[K_z] \cdot \frac{\dot{y}_\omega[n]}{\omega} \right) \quad (\text{B-12})$$

B.3 Example

An example of an oscillation test that involves cutting AISI1045 steel with an orthogonal carbide tool is shown in Figure B-1. Displacement signal y has very little noise and it is almost identical to y_ω ; the sinusoidal component of the signal is extracted using (B-8).

The cutting force signals contain more energy in frequencies other than ω . Also, the imaginary part of the cutting coefficients multiplied to the tool's penetration velocity \dot{y}_ω at the frequency of the oscillation has a major contribution to the dynamic cutting forces in y and z directions. This means that the dynamic cutting forces are mainly created by

the process damping mechanism. The extracted dynamic cutting coefficients are presented in Table B-1 along with the parameters used in DTFT calculation.

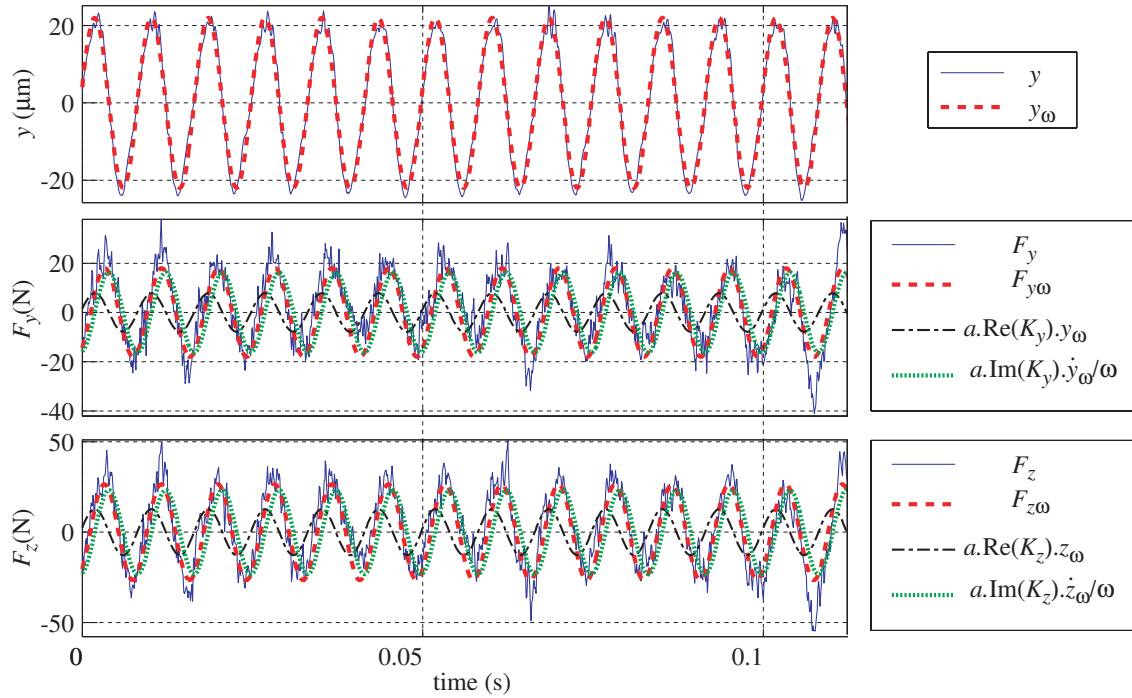


Figure B-1: Dynamic cutting test, AIS1045, width of cut $a = 0.5\text{mm}$, carbide tool, orthogonal cutting, Spindle Speed: 300rpm, oscillation frequency: 120Hz. The phase between inner and outer wave is zero.

Table B-1: Cutting conditions and dynamic cutting coefficients in the sample dynamic cutting test

Width of cut	$a = 0.5 \times 10^{-3} [\text{m}]$
Number of samples	$L = 2250$
Sampling Period	$T_s = 1.0 \times 10^{-4} [\text{s}]$
Oscillation Frequency	$\omega = 120 \times 2\pi [\text{rad/s}]$
DTFT of displacement	$Y(\omega) = 4569 - i 24292 [\mu\text{m}]$
DTFT of F_y	$F_y(\omega) = -16292 - i 12030 [\text{N}]$
DTFT of F_z	$F_z(\omega) = -23050 - i 18921 [\text{N}]$
Dynamic cutting coefficient in y direction at ω	$K_y(\omega) = 713 - i 1475 [\text{MPa}]$
Dynamic cutting coefficient in z direction at ω	$K_z(\omega) = 1160 - i 2116 [\text{MPa}]$

Appendix C: Averaging Dynamic Matrices in Milling

The directional matrix elements in milling stability prediction are periodic at spindle periods, i.e. at 2π in angular or $\tau_p = 2\pi/\Omega$ in time intervals. However, the directional factors are nonzero only when their corresponding tooth is in cut, $\phi_{st} \leq \text{mod}(\phi_j, 2\pi) \leq \phi_{ex}$. Since $\phi_j(t) = \phi - \phi_c - j\phi_p$, the pulse function $g(\phi_j)$ from Eq. (5-7) is related to $\phi(t)$ as:

$$g(\phi_j) = g_j(\phi) = \begin{cases} 1 & \phi_{st} + j\phi_p + \phi_c \leq \text{mod}(\phi, 2\pi) \leq \phi_{ex} + j\phi_p + \phi_c \\ 0 & \text{otherwise} \end{cases} \quad (\text{C-1})$$

The $g_j(\phi)$ functions are periodic at 2π intervals as illustrated for a sample cutter with an engagement shown in Figure C-1.

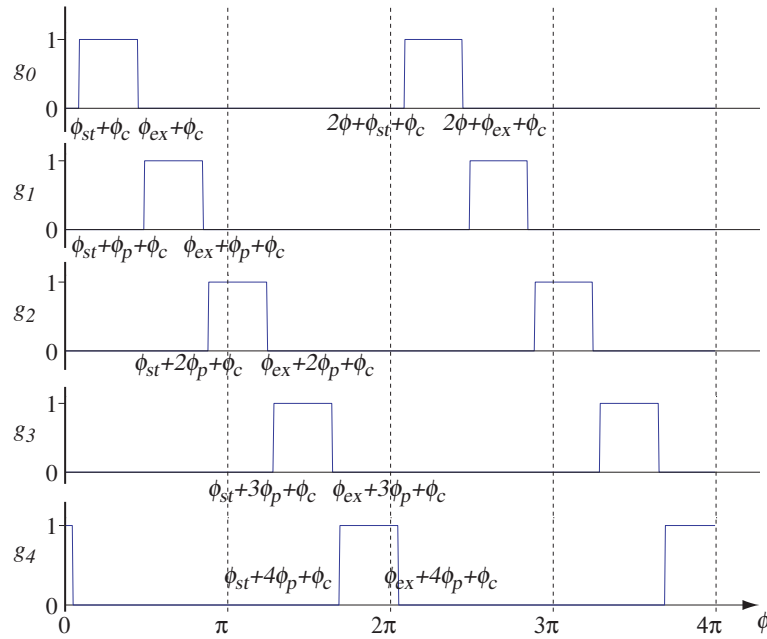


Figure C-1: $g_j(\phi)$ functions for a five flute cutter with $\phi_c = 0$, $\phi_{st} = 15/180\pi$ and $\phi_{ex} = 80/180\pi$

Directional matrices are first analytically expressed as a function of angular position of the reference system as follows. As an example, the upper left 2x2 sub-matrix of $\mathbf{P}(t)$ is $\mathbf{A}(t)$ which is summation of time invariant \mathbf{A}_j matrices multiplied to time variant $g_j(\phi)$ functions:

$$\mathbf{A}(t) = \sum_{j=0}^{N-1} g_j(\phi) \mathbf{A}_j \quad (\text{C-2})$$

$$\mathbf{A}_j = \mathbf{R}_j^{-1} \left(\begin{Bmatrix} K_r \\ K_t \end{Bmatrix} [1 \quad 0] \mathbf{R}_j + \frac{\Omega}{V_c} \begin{Bmatrix} C_r \\ C_t \end{Bmatrix} [1 \quad 0] \mathbf{R}_j \begin{bmatrix} 0 & -1 \\ 1 & 0 \end{bmatrix} \right)$$

The lower left sub-matrix is $\mathbf{W}^{-1}(t) \mathbf{A}(t)$:

$$\mathbf{W}^{-1}(t) \mathbf{A}(t) = \mathbf{W}^{-1}(\phi) \mathbf{A}(\phi) = \sum_{j=0}^{N-1} g_j(\phi) \mathbf{W}^{-1}(\phi) \mathbf{A}_j \quad (\text{C-3})$$

This matrix has time-varying elements such as $\phi = \Omega t$. These matrices are averaged to obtain time invariant characteristic equation of dynamic milling. Note that the elements are periodic at spindle rotation time (τ_p) or angular ($\Omega \tau_p = 2\pi$) intervals; hence, the averages are made in angular domain by change of variables as:

$$\phi = \Omega t \Rightarrow d\phi = \Omega dt \Rightarrow dt = \frac{1}{\Omega} d\phi \quad (\text{C-4})$$

Let $\alpha(\phi) = \alpha(\phi + 2\pi)$ represent a periodic function with a 2π period. $\bar{\alpha}$, the mean of this periodic function modulated by the unit pulse function $g_j(\phi)$ is evaluated as such:

$$\begin{aligned}
 \bar{\alpha} &= \frac{1}{\tau_p} \int_0^{\tau_p} g_j(t) \cdot \alpha(t) dt \\
 &= \frac{1}{2\pi} \int_0^{2\pi} g_j(\phi) \cdot \alpha(\phi) d\phi \\
 &= \frac{1}{2\pi} \int_{\phi_{st} + j\phi_p + \phi_c}^{2\pi + \phi_{st} + j\phi_p + \phi_c} g_j(\phi) \cdot \alpha(\phi) d\phi \\
 &= \frac{1}{2\pi} \int_{\phi_{st} + j\phi_p + \phi_c}^{\phi_{ex} + j\phi_p + \phi_c} \underbrace{g_j(\phi) \cdot \alpha(\phi)}_1 d\phi + \frac{1}{2\pi} \int_{\phi_{ex} + j\phi_p + \phi_c}^{2\pi + \phi_{st} + j\phi_p + \phi_c} \underbrace{g_j(\phi) \cdot \alpha(\phi)}_0 d\phi \\
 &= \frac{1}{2\pi} \int_{\phi_{st} + j\phi_p + \phi_c}^{\phi_{ex} + j\phi_p + \phi_c} \alpha(\phi) d\phi
 \end{aligned} \tag{C-5}$$

Hence, the average of the sample sub-matrix $\mathbf{W}^{-1}(t) \mathbf{A}(t)$ is expressed as:

$$\begin{aligned}
 \overline{\mathbf{W}^{-1}(\phi) \mathbf{A}(\phi)} &= \sum_{j=0}^{N-1} \overline{\left(g_j(\phi) \mathbf{W}^{-1}(\phi) \mathbf{A}_j \right)} \\
 &= \sum_{j=0}^{N-1} \frac{1}{2\pi} \int_{\phi_{st} + j\phi_p + \phi_c}^{\phi_{ex} + j\phi_p + \phi_c} \mathbf{W}^{-1}(\phi) \mathbf{A}_j d\phi
 \end{aligned} \tag{C-6}$$

Similarly, the averages of all sub-matrices in characteristic equation (Eq. (5-27)) are evaluated.

$$\overline{\mathbf{H}} = \sum_{j=0}^{N-1} \overline{g_j(\phi) \mathbf{H}_j(\phi)} = \sum_{j=0}^{N-1} \underbrace{\frac{1}{2\pi} \int_{\phi_{st} + j\phi_p + \phi_c}^{\phi_{ex} + j\phi_p + \phi_c} \mathbf{H}_j(\phi) d\phi}_{\overline{\mathbf{H}}_j}, \quad \mathbf{H} \in (\mathbf{P}, \mathbf{Q}, \mathbf{J}) \tag{C-7}$$

The matrix elements which need averaging (the $\mathbf{H}_j(\phi)$ matrices) are as follows:

$$\begin{aligned}
 \mathbf{P}_j(\phi) = & \\
 & \frac{K_r}{2} \begin{bmatrix} 1 + \cos(2j\phi_p + 2\phi_c) & -\sin(2j\phi_p + 2\phi_c) & \sin\phi + \sin(\phi - 2j\phi_p - 2\phi_c) & \cos\phi + \cos(\phi - 2j\phi_p - 2\phi_c) \\ -\sin(2j\phi_p + 2\phi_c) & 1 - \cos(2j\phi_p + 2\phi_c) & \cos\phi - \cos(\phi - 2j\phi_p - 2\phi_c) & -\sin\phi + \sin(\phi - 2j\phi_p - 2\phi_c) \\ \sin\phi + \sin(\phi - 2j\phi_p - 2\phi_c) & \cos\phi - \cos(\phi - 2j\phi_p - 2\phi_c) & 1 - \cos(2\phi - 2j\phi_p - 2\phi_c) & \sin(2\phi - 2j\phi_p - 2\phi_c) \\ \cos\phi + \cos(\phi - 2j\phi_p - 2\phi_c) & -\sin\phi + \sin(\phi - 2j\phi_p - 2\phi_c) & \sin(2\phi - 2j\phi_p - 2\phi_c) & 1 + \cos(2\phi - 2j\phi_p - 2\phi_c) \end{bmatrix} \\
 & + \frac{K_t}{2} \begin{bmatrix} \sin(2j\phi_p + 2\phi_c) & \cos(2j\phi_p + 2\phi_c) - 1 & -\cos\phi + \cos(\phi - 2j\phi_p - 2\phi_c) & \sin\phi - \sin(\phi - 2j\phi_p - 2\phi_c) \\ \cos(2j\phi_p + 2\phi_c) + 1 & -\sin(2j\phi_p + 2\phi_c) & \sin\phi + \sin(\phi - 2j\phi_p - 2\phi_c) & \cos\phi + \cos(\phi - 2j\phi_p - 2\phi_c) \\ \cos\phi + \cos(\phi - 2j\phi_p - 2\phi_c) & -\sin\phi + \sin(\phi - 2j\phi_p - 2\phi_c) & \sin(2\phi - 2j\phi_p - 2\phi_c) & \cos(2\phi - 2j\phi_p - 2\phi_c) + 1 \\ -\sin\phi - \sin(\phi - 2j\phi_p - 2\phi_c) & -\cos\phi + \cos(\phi - 2j\phi_p - 2\phi_c) & \cos(2\phi_0 - 2\phi_p - 2\phi_c) - 1 & -\sin(2\phi - 2j\phi_p - 2\phi_c) \end{bmatrix} \quad (\text{C-8}) \\
 & + \frac{C_r \Omega}{2V_c} \begin{bmatrix} -\sin(2j\phi_p + 2\phi_c) & -1 - \cos(2j\phi_p + 2\phi_c) & 0 & 0 \\ 1 - \cos(2j\phi_p + 2\phi_c) & \sin(2j\phi_p + 2\phi_c) & 0 & 0 \\ \cos\phi - \cos(\phi - 2j\phi_p - 2\phi_c) & -\sin\phi - \sin(\phi - 2j\phi_p - 2\phi_c) & 0 & 0 \\ -\sin\phi + \sin(\phi - 2j\phi_p - 2\phi_c) & -\cos\phi - \cos(\phi - 2j\phi_p - 2\phi_c) & 0 & 0 \end{bmatrix} \\
 & + \frac{C_t \Omega}{2V_c} \begin{bmatrix} -1 + \cos(2j\phi_p + 2\phi_c) & -\sin(2j\phi_p + 2\phi_c) & 0 & 0 \\ -\sin(2j\phi_p + 2\phi_c) & -1 - \cos(2j\phi_p + 2\phi_c) & 0 & 0 \\ \sin(\phi - 2j\phi_p - 2\phi_c) - \sin\phi & -\cos(\phi - 2j\phi_p - 2\phi_c) - \cos\phi & 0 & 0 \\ -\cos\phi + \cos(\phi - 2j\phi_p - 2\phi_c) & \sin(\phi - 2j\phi_p - 2\phi_c) + \sin\phi & 0 & 0 \end{bmatrix}
 \end{aligned}$$

$$\begin{aligned}
 \mathbf{Q}_j(\phi) = & \\
 & \frac{K_r}{2} \begin{bmatrix} \cos\phi_p + \cos((2j-1)\phi_p + 2\phi_c) & -\sin((2j-1)\phi_p + 2\phi_c) + \sin\phi_p & \sin(\phi - 2j\phi_p - 2\phi_c) + \sin\phi & \cos(\phi - 2j\phi_p - 2\phi_c) + \cos\phi \\ -\sin((2j-1)\phi_p + 2\phi_c) - \sin\phi_p & \cos\phi_p - \cos((2j-1)\phi_p + 2\phi_c) & -\cos(\phi - 2j\phi_p - 2\phi_c) + \cos\phi & \sin(\phi - 2j\phi_p - 2\phi_c) - \sin\phi \\ \sin(\phi - \phi_p) + \sin(\phi - (2j-1)\phi_p - 2\phi_c) & -\cos(\phi - (2j-1)\phi_p - 2\phi_c) + \cos(\phi - \phi_p) & -\cos(2\phi - 2j\phi_p - 2\phi_c) + 1 & \sin(2\phi - 2j\phi_p - 2\phi_c) \\ \cos(\phi - (2j-1)\phi_p - 2\phi_c) + \cos(\phi - \phi_p) & -\sin(\phi - \phi_p) + \sin(\phi - (2j-1)\phi_p - 2\phi_c) & \sin(2\phi - 2j\phi_p - 2\phi_c) & \cos(2\phi - 2j\phi_p - 2\phi_c) + 1 \end{bmatrix} \quad (\text{C-9}) \\
 & + \frac{K_t}{2} \begin{bmatrix} -\sin((2j-1)\phi_p - 2\phi_c) + \sin\phi_p & -\cos\phi_p + \cos((2j-1)\phi_p + 2\phi_c) & \cos(\phi - 2j\phi_p - 2\phi_c) - \cos\phi & -\sin(\phi - 2j\phi_p - 2\phi_c) + \sin\phi \\ \cos\phi_p + \cos((2j-1)\phi_p + 2\phi_c) & -\sin((2j-1)\phi_p + 2\phi_c - \phi_p) + \sin\phi_p & \sin(\phi - 2j\phi_p - 2\phi_c) + \sin\phi & \cos(\phi - 2j\phi_p - 2\phi_c) + \cos\phi \\ \cos(\phi - (2j-1)\phi_p - 2\phi_c) + \cos(\phi - \phi_p) & -\sin(\phi - \phi_p) + \sin(\phi - 2j\phi_p + \phi_p - 2\phi_c) & \sin(2\phi - 2j\phi_p - 2\phi_c) & \cos(2\phi - 2j\phi_p - 2\phi_c) + 1 \\ -\sin(\phi - \phi_p) - \sin(\phi - (2j-1)\phi_p - 2\phi_c) & \cos(\phi - (2j-1)\phi_p - 2\phi_c) - \cos(\phi - \phi_p) & \cos(2\phi - 2j\phi_p - 2\phi_c) - 1 & -\sin(2\phi - 2j\phi_p - 2\phi_c) \end{bmatrix}
 \end{aligned}$$

$$\begin{aligned}
 \mathbf{J}_j(\phi) = & \\
 & \frac{C_r}{2V_c} \begin{bmatrix} \cos(2j\phi_p + 2\phi_c) + 1 & -\sin(2j\phi_p + 2\phi_c) & \sin(\phi - 2j\phi_p - 2\phi_c) + \sin\phi & \cos(\phi - 2j\phi_p - 2\phi_c) + \cos\phi \\ -\sin(2j\phi_p + 2\phi_c) & 1 - \cos(2j\phi_p + 2\phi_c) & -\cos(\phi - 2j\phi_p - 2\phi_c) + \cos\phi & \sin(\phi - 2j\phi_p - 2\phi_c) - \sin\phi \\ \sin(\phi - 2j\phi_p - 2\phi_c) + \sin\phi & -\cos(\phi - 2j\phi_p - 2\phi_c) + \cos\phi & -\cos(2\phi - 2j\phi_p - 2\phi_c) + 1 & \sin(2\phi - 2j\phi_p - 2\phi_c) \\ \cos(\phi - 2j\phi_p - 2\phi_c) + \cos\phi & \sin(\phi - 2j\phi_p - 2\phi_c) - \sin\phi & \sin(2\phi - 2j\phi_p - 2\phi_c) & \cos(2\phi - 2j\phi_p - 2\phi_c) + 1 \end{bmatrix} \quad (\text{C-10}) \\
 & + \frac{C_t}{2V_c} \begin{bmatrix} \sin(2j\phi_p + 2\phi_c) & -1 + \cos(2j\phi_p + 2\phi_c) & \sin(\phi - 2j\phi_p - 2\phi_c) + \sin\phi & \cos(\phi - 2j\phi_p - 2\phi_c) + \cos\phi \\ \cos(2j\phi_p + 2\phi_c) + 1 & -\sin(2j\phi_p + 2\phi_c) & -\cos(\phi - 2j\phi_p - 2\phi_c) + \cos\phi & \sin(\phi - 2j\phi_p - 2\phi_c) - \sin\phi \\ \cos(\phi - 2j\phi_p - 2\phi_c) + \cos\phi & \sin(\phi - 2j\phi_p - 2\phi_c) - \sin\phi & \sin(2\phi - 2j\phi_p - 2\phi_c) & \cos(2\phi - 2j\phi_p - 2\phi_c) + 1 \\ -\sin(\phi - 2j\phi_p - 2\phi_c) - \sin\phi & \cos(\phi - 2j\phi_p - 2\phi_c) - \cos\phi & \cos(2\phi - 2j\phi_p - 2\phi_c) - 1 & -\sin(2\phi - 2j\phi_p - 2\phi_c) \end{bmatrix}
 \end{aligned}$$

C.1 Summation of Average Matrices

The average matrices, $\bar{\mathbf{P}}$, $\bar{\mathbf{Q}}$ and $\bar{\mathbf{J}}$, are summations of $\bar{\mathbf{P}}_j$, $\bar{\mathbf{Q}}_j$ and $\bar{\mathbf{J}}_j$ for $j = 0 \cdots N - 1$. These summations are evaluated analytically using a simplifying lemma introduced in the next section.

C.1.1 Summation lemma

If m/N is not an integer:

$$\sum_{j=0}^{N-1} \cos\left(j \cdot \frac{2\pi m}{N} + \theta\right) = 0 \quad \text{and} \quad \sum_{j=0}^{N-1} \sin\left(j \cdot \frac{2\pi m}{N} + \theta\right) = 0 \quad (\text{C-14})$$

Proof:

$$\begin{aligned} \sum_{j=0}^{N-1} e^{i\left(j \cdot \frac{2\pi m}{N} + \theta\right)} &= \sum_{j=1}^N e^{i\left((j-1) \cdot \frac{2\pi m}{N} + \theta\right)} = e^{-i \frac{2\pi m}{N}} \sum_{j=1}^N e^{i\left(j \cdot \frac{2\pi m}{N} + \theta\right)} \\ \sum_{j=1}^N e^{i\left(j \cdot \frac{2\pi m}{N} + \theta\right)} &= \sum_{j=1}^{N-1} e^{i\left(j \cdot \frac{2\pi m}{N} + \theta\right)} + e^{i\left(N \cdot \frac{2\pi m}{N} + \theta\right)} \\ e^{i\left(N \cdot \frac{2\pi m}{N} + \theta\right)} &= e^{i(\theta)} \Rightarrow \sum_{j=1}^N e^{i\left(j \cdot \frac{2\pi m}{N} + \theta\right)} = \sum_{j=0}^{N-1} e^{i\left(j \cdot \frac{2\pi m}{N} + \theta\right)} \\ \sum_{j=0}^{N-1} e^{i\left(j \cdot \frac{2\pi m}{N} + \theta\right)} &= e^{-i \frac{2\pi m}{N}} \sum_{j=1}^N e^{i\left(j \cdot \frac{2\pi m}{N} + \theta\right)} = e^{-i \frac{2\pi m}{N}} \sum_{j=0}^{N-1} e^{i\left(j \cdot \frac{2\pi m}{N} + \theta\right)} \\ \Rightarrow \left(1 - e^{-i \frac{2\pi m}{N}}\right) \sum_{j=0}^{N-1} e^{i\left(j \cdot \frac{2\pi m}{N} + \theta\right)} &= 0 \\ m/N \text{ is not an integer} \Rightarrow \left(1 - e^{-i \frac{2\pi m}{N}}\right) &\neq 0 \end{aligned} \quad \left. \vphantom{\sum_{j=0}^{N-1} e^{i\left(j \cdot \frac{2\pi m}{N} + \theta\right)}} \right\} \Rightarrow \sum_{j=0}^{N-1} e^{i\left(j \cdot \frac{2\pi m}{N} + \theta\right)} = 0 \quad (\text{C-15})$$

(Here, j is an integer while $i = \sqrt{-1}$ is the imaginary unit).

Considering the Euler's formula:

$$\sum_{j=0}^{N-1} e^{i\left(j \cdot \frac{2\pi m}{N} + \theta\right)} = \sum_{j=0}^{N-1} \cos\left(j \cdot \frac{2\pi m}{N} + \theta\right) + i \sum_{j=0}^{N-1} \sin\left(j \cdot \frac{2\pi m}{N} + \theta\right) \quad (\text{C-16})$$

If the sum of a series is zero, then its real and imaginary parts are zero, hence the lemma

is valid. Note that **if $\frac{m}{N} = p$ is an integer, the following would result:**

$$\cos\left(j \cdot \frac{2\pi m}{N} + \theta\right) = \cos \theta \quad \text{and} \quad \sin\left(j \cdot \frac{2\pi m}{N} + \theta\right) = \sin \theta$$

\Rightarrow

$$\sum_{j=0}^{N-1} \cos\left(j \cdot \frac{2\pi m}{N} + \theta\right) = \sum_{j=0}^{N-1} \cos \theta = N \cos \theta, \quad (\text{C-17})$$

$$\sum_{j=0}^{N-1} \sin\left(j \cdot \frac{2\pi m}{N} + \theta\right) = \sum_{j=0}^{N-1} \sin \theta = N \sin \theta$$

These lemmas lead to following relations:

$$\begin{aligned}
 \sum_{j=0}^{N-1} c &= Nc \quad (c \text{ is constant with respect to } j) \\
 \sum_{j=0}^{N-1} \sin(j\phi_p + \phi_c) &= \sum_{j=0}^{N-1} \sin\left(j \frac{2\pi}{N} + \phi_c\right) = \begin{cases} \sin \phi_c & \text{for } N = 1 \\ 0 & \text{for } N > 1 \end{cases} \\
 \sum_{j=0}^{N-1} \cos(j\phi_p + \phi_c) &= \sum_{j=0}^{N-1} \cos\left(j \cdot \frac{2\pi}{N} + \phi_c\right) = \begin{cases} \cos \phi_c & \text{for } N = 1 \\ 0 & \text{for } N > 1 \end{cases} \\
 \sum_{j=0}^{N-1} \sin(2j\phi_p + 2\phi_c) &= \sum_{j=0}^{N-1} \sin\left(j \cdot \frac{2\pi \cdot 2}{N} + 2\phi_c\right) = \begin{cases} \sin 2\phi_c & \text{for } N = 1 \\ 2 \sin 2\phi_c & \text{for } N = 2 \\ 0 & \text{for } N > 2 \end{cases} \\
 \sum_{j=0}^{N-1} \cos(2j\phi_p + 2\phi_c) &= \sum_{j=0}^{N-1} \cos\left(j \cdot \frac{2\pi \cdot 2}{N} + 2\phi_c\right) = \begin{cases} \cos 2\phi_c & \text{for } N = 1 \\ 2 \cos 2\phi_c & \text{for } N = 2 \\ 0 & \text{for } N > 2 \end{cases} \quad (\text{C-18}) \\
 \sum_{j=0}^{N-1} \sin^2(j\phi_p + \phi_c) &= \sum_{j=0}^{N-1} \frac{1 - \cos(2j\phi_p + 2\phi_c)}{2} = \begin{cases} \sin^2 \phi_c & \text{for } N = 1 \\ 2 \sin^2 \phi_c & \text{for } N = 2 \\ N / 2 & \text{for } N > 2 \end{cases} \\
 \sum_{j=0}^{N-1} \cos^2(j\phi_p + \phi_c) &= \sum_{j=0}^{N-1} \frac{1 + \cos(2j\phi_p + 2\phi_c)}{2} = \begin{cases} \cos^2 \phi_c & \text{for } N = 1 \\ 2 \cos^2 \phi_c & \text{for } N = 2 \\ N / 2 & \text{for } N > 2 \end{cases}
 \end{aligned}$$

C.1.2 Average matrix for cutters having more than two teeth

Using the summation lemmas, the average directional matrices become as follows for cutters having more than $N > 2$ teeth.

$$\begin{aligned}
 \bar{\mathbf{P}}|_{N>2} = & \frac{NK_r}{4\pi} \begin{bmatrix} (\phi_{ex} - \phi_{st}) & 0 & 0 & 0 \\ 0 & (\phi_{ex} - \phi_{st}) & 0 & 0 \\ 0 & 0 & (\phi_{ex} - \phi_{st}) - \frac{\sin 2\phi_{ex} - \sin 2\phi_{st}}{2} & -\frac{\cos 2\phi_{ex} - \cos 2\phi_{st}}{2} \\ 0 & 0 & -\frac{\cos 2\phi_{ex} - \cos 2\phi_{st}}{2} & (\phi_{ex} - \phi_{st}) + \frac{\sin 2\phi_{ex} - \sin 2\phi_{st}}{2} \end{bmatrix} \\
 & + \frac{NK_t}{4\pi} \begin{bmatrix} 0 & -(\phi_{ex} - \phi_{st}) & 0 & 0 \\ (\phi_{ex} - \phi_{st}) & 0 & 0 & 0 \\ 0 & 0 & -\frac{\cos 2\phi_{ex} - \cos 2\phi_{st}}{2} & (\phi_{ex} - \phi_{st}) + \frac{\sin 2\phi_{ex} - \sin 2\phi_{st}}{2} \\ 0 & 0 & -(\phi_{ex} - \phi_{st}) + \frac{\sin 2\phi_{ex} - \sin 2\phi_{st}}{2} & \frac{\cos 2\phi_{ex} - \cos 2\phi_{st}}{2} \end{bmatrix} \\
 & + \frac{NC_r \Omega}{4\pi V_c} \begin{bmatrix} 0 & -(\phi_{ex} - \phi_{st})/2 & 0 & 0 \\ (\phi_{ex} - \phi_{st})/2 & 0 & 0 & 0 \\ 0 & 0 & 0 & 0 \\ 0 & 0 & 0 & 0 \end{bmatrix} \\
 & + \frac{C_t \Omega}{4\pi V_c} \begin{bmatrix} -(\phi_{ex} - \phi_{st})/2 & 0 & 0 & 0 \\ 0 & -(\phi_{ex} - \phi_{st})/2 & 0 & 0 \\ 0 & 0 & 0 & 0 \\ 0 & 0 & 0 & 0 \end{bmatrix}
 \end{aligned} \tag{C-19}$$

$$\begin{aligned}
 \bar{\mathbf{Q}}|_{N>2} = & \frac{NK_r}{4\pi} \begin{bmatrix} \cos \phi_p \cdot (\phi_{ex} - \phi_{st}) & \sin \phi_p \cdot (\phi_{ex} - \phi_{st}) & 0 & 0 \\ -\sin \phi_p \cdot (\phi_{ex} - \phi_{st}) & \cos \phi_p \cdot (\phi_{ex} - \phi_{st}) & 0 & 0 \\ 0 & 0 & (\phi_{ex} - \phi_{st}) - \frac{\sin 2\phi_{ex} - \sin 2\phi_{st}}{2} & -\frac{\cos 2\phi_{ex} - \cos 2\phi_{st}}{2} \\ 0 & 0 & -\frac{\cos 2\phi_{ex} - \cos 2\phi_{st}}{2} & (\phi_{ex} - \phi_{st}) + \frac{\sin 2\phi_{ex} - \sin 2\phi_{st}}{2} \end{bmatrix} \\
 & + \frac{NK_t}{4\pi} \begin{bmatrix} \sin \phi_p \cdot (\phi_{ex} - \phi_{st}) & \cos \phi_p \cdot (\phi_{ex} - \phi_{st}) & 0 & 0 \\ \cos \phi_p \cdot (\phi_{ex} - \phi_{st}) & \sin \phi_p \cdot (\phi_{ex} - \phi_{st}) & 0 & 0 \\ 0 & 0 & -\frac{\cos 2\phi_{ex} - \cos 2\phi_{st}}{2} & (\phi_{ex} - \phi_{st}) + \frac{\sin 2\phi_{ex} - \sin 2\phi_{st}}{2} \\ 0 & 0 & -(\phi_{ex} - \phi_{st}) + \frac{\sin 2\phi_{ex} - \sin 2\phi_{st}}{2} & \frac{\cos 2\phi_{ex} - \cos 2\phi_{st}}{2} \end{bmatrix}
 \end{aligned} \tag{C-20}$$

$$\begin{aligned}
 \bar{\mathbf{J}}|_{N>2} = & \frac{NC_r}{4\pi V_c} \begin{bmatrix} (\phi_{ex} - \phi_{st}) & 0 & 0 & 0 \\ 0 & (\phi_{ex} - \phi_{st}) & 0 & 0 \\ 0 & 0 & (\phi_{ex} - \phi_{st}) - \frac{\sin 2\phi_{ex} - \sin 2\phi_{st}}{2} & -\frac{\cos 2\phi_{ex} - \cos 2\phi_{st}}{2} \\ 0 & 0 & -\frac{\cos 2\phi_{ex} - \cos 2\phi_{st}}{2} & (\phi_{ex} - \phi_{st}) + \frac{\sin 2\phi_{ex} - \sin 2\phi_{st}}{2} \end{bmatrix} \\
 & + \frac{NC_t}{4\pi V_c} \begin{bmatrix} 0 & -(\phi_{ex} - \phi_{st}) & 0 & 0 \\ (\phi_{ex} - \phi_{st}) & 0 & 0 & 0 \\ 0 & 0 & -\frac{\cos 2\phi_{ex} - \cos 2\phi_{st}}{2} & (\phi_{ex} - \phi_{st}) + \frac{\sin 2\phi_{ex} - \sin 2\phi_{st}}{2} \\ 0 & 0 & -(\phi_{ex} - \phi_{st}) + \frac{\sin 2\phi_{ex} - \sin 2\phi_{st}}{2} & \frac{\cos 2\phi_{ex} - \cos 2\phi_{st}}{2} \end{bmatrix}
 \end{aligned} \tag{C-21}$$

C.1.3 Average matrix for a tool with two teeth (N=2)

$$\begin{aligned}
 \bar{\mathbf{P}}|_{N=2} = & \frac{K_r}{2\pi} \begin{bmatrix} 2\cos^2(\phi_c) \cdot (\phi_{ex} - \phi_{st}) & -\sin 2\phi_c \cdot (\phi_{ex} - \phi_{st}) & 0 & 0 \\ -\sin 2\phi_c \cdot (\phi_{ex} - \phi_{st}) & 2\sin^2 \phi_c \cdot (\phi_{ex} - \phi_{st}) & 0 & 0 \\ 0 & 0 & (\phi_{ex} - \phi_{st}) - \frac{\sin 2\phi_{ex} - \sin 2\phi_{st}}{2} & -\frac{\cos 2\phi_{ex} - \cos 2\phi_{st}}{2} \\ 0 & 0 & -\frac{\cos 2\phi_{ex} - \cos 2\phi_{st}}{2} & (\phi_{ex} - \phi_{st}) + \frac{\sin 2\phi_{ex} - \sin 2\phi_{st}}{2} \end{bmatrix} \\
 + & \frac{K_t}{2\pi} \begin{bmatrix} \sin 2\phi_c \cdot (\phi_{ex} - \phi_{st}) & -2\sin^2 \phi_c \cdot (\phi_{ex} - \phi_{st}) & 0 & 0 \\ 2\cos^2 \phi_c \cdot (\phi_{ex} - \phi_{st}) & -\sin 2\phi_c \cdot (\phi_{ex} - \phi_{st}) & 0 & 0 \\ 0 & 0 & -\frac{\cos 2\phi_{ex} - \cos 2\phi_{st}}{2} & (\phi_{ex} - \phi_{st}) + \frac{\sin 2\phi_{ex} - \sin 2\phi_{st}}{2} \\ 0 & 0 & -(\phi_{ex} - \phi_{st}) + \frac{\sin 2\phi_{ex} - \sin 2\phi_{st}}{2} & \frac{\cos 2\phi_{ex} - \cos 2\phi_{st}}{2} \end{bmatrix} \\
 + & \frac{C_r \Omega}{2\pi V_c} \begin{bmatrix} -\sin(\phi_c) \cdot (\phi_{ex} - \phi_{st}) & -\cos^2(\phi_c) \cdot (\phi_{ex} - \phi_{st}) & 0 & 0 \\ \sin^2(\phi_c) \cdot (\phi_{ex} - \phi_{st}) & \sin(2\phi_c) \cdot (\phi_{ex} - \phi_{st}) & 0 & 0 \\ 0 & 0 & 0 & 0 \\ 0 & 0 & 0 & 0 \end{bmatrix} \\
 + & \frac{C_t \Omega}{2\pi V_c} \begin{bmatrix} -\sin^2(\phi_c) \cdot (\phi_{ex} - \phi_{st}) & -\sin(2\phi_c) \cdot (\phi_{ex} - \phi_{st}) & 0 & 0 \\ -\sin(2\phi_c) \cdot (\phi_{ex} - \phi_{st}) & -\cos^2(\phi_c) \cdot (\phi_{ex} - \phi_{st}) & 0 & 0 \\ 0 & 0 & 0 & 0 \\ 0 & 0 & 0 & 0 \end{bmatrix}
 \end{aligned} \tag{C-22}$$

$$\begin{aligned}
 \bar{\mathbf{Q}}|_{N=2} = & \frac{K_r}{2\pi} \begin{bmatrix} \cos \phi_p \cdot (\phi_{ex} - \phi_{st}) & \sin \phi_p \cdot (\phi_{ex} - \phi_{st}) & 0 & 0 \\ -\sin \phi_p \cdot (\phi_{ex} - \phi_{st}) & \cos \phi_p \cdot (\phi_{ex} - \phi_{st}) & 0 & 0 \\ 0 & 0 & (\phi_{ex} - \phi_{st}) - \frac{\sin 2\phi_{ex} - \sin 2\phi_{st}}{2} & -\frac{\cos 2\phi_{ex} - \cos 2\phi_{st}}{2} \\ 0 & 0 & -\frac{\cos 2\phi_{ex} - \cos 2\phi_{st}}{2} & (\phi_{ex} - \phi_{st}) + \frac{\sin 2\phi_{ex} - \sin 2\phi_{st}}{2} \end{bmatrix} \\
 + & \frac{K_t}{2\pi} \begin{bmatrix} \sin \phi_p \cdot (\phi_{ex} - \phi_{st}) & \cos \phi_p \cdot (\phi_{ex} - \phi_{st}) & 0 & 0 \\ \cos \phi_p \cdot (\phi_{ex} - \phi_{st}) & \sin \phi_p \cdot (\phi_{ex} - \phi_{st}) & 0 & 0 \\ 0 & 0 & -\frac{\cos 2\phi_{ex} - \cos 2\phi_{st}}{2} & (\phi_{ex} - \phi_{st}) + \frac{\sin 2\phi_{ex} - \sin 2\phi_{st}}{2} \\ 0 & 0 & -(\phi_{ex} - \phi_{st}) + \frac{\sin 2\phi_{ex} - \sin 2\phi_{st}}{2} & \frac{\cos 2\phi_{ex} - \cos 2\phi_{st}}{2} \end{bmatrix}
 \end{aligned} \tag{C-23}$$

$$\begin{aligned}
 \bar{\mathbf{J}}|_{N=2} = & \frac{C_r}{2\pi V_c} \begin{bmatrix} 2\cos^2(\phi_c) \cdot (\phi_{ex} - \phi_{st}) & -\sin(2\phi_c) \cdot (\phi_{ex} - \phi_{st}) & 0 & 0 \\ -\sin(2\phi_c) \cdot (\phi_{ex} - \phi_{st}) & 2\sin^2(\phi_c) \cdot (\phi_{ex} - \phi_{st}) & 0 & 0 \\ 0 & 0 & (\phi_{ex} - \phi_{st}) - \frac{\sin 2\phi_{ex} - \sin 2\phi_{st}}{2} & -\frac{\cos 2\phi_{ex} - \cos 2\phi_{st}}{2} \\ 0 & 0 & -\frac{\cos 2\phi_{ex} - \cos 2\phi_{st}}{2} & (\phi_{ex} - \phi_{st}) + \frac{\sin 2\phi_{ex} - \sin 2\phi_{st}}{2} \end{bmatrix} \\
 + & \frac{C_t}{2\pi V_c} \begin{bmatrix} \sin(2\phi_c) \cdot (\phi_{ex} - \phi_{st}) & 0 & -2\sin^2(\phi_c) \cdot (\phi_{ex} - \phi_{st}) & 0 \\ 2\cos^2(\phi_c) \cdot (\phi_{ex} - \phi_{st}) & -\sin(2\phi_c) \cdot (\phi_{ex} - \phi_{st}) & 0 & 0 \\ 0 & 0 & -\frac{\cos 2\phi_{ex} - \cos 2\phi_{st}}{2} & (\phi_{ex} - \phi_{st}) + \frac{\sin 2\phi_{ex} - \sin 2\phi_{st}}{2} \\ 0 & 0 & -(\phi_{ex} - \phi_{st}) + \frac{\sin 2\phi_{ex} - \sin 2\phi_{st}}{2} & \frac{\cos 2\phi_{ex} - \cos 2\phi_{st}}{2} \end{bmatrix}
 \end{aligned} \tag{C-24}$$

C.1.4 Average matrix for a single tooth tool (N=1)

Since summation is not necessary for a single tooth tool and given that $\bar{\mathbf{P}} = \bar{\mathbf{P}}_{j=0}$, by using

$\phi_p = 2\pi$, the following would result:

C.2 Comparison with Classical Stability Prediction Method

Altintas and Budak [3] present an analytical stability limit prediction method for systems with dynamics described in inertial coordinate system without considering process damping. Ignoring process damping term ($\bar{\mathbf{J}}$) in Eq. (5-27) leads to the following characteristic equation:

$$\det \left[\mathbf{I}_{4 \times 4} + a \left(\bar{\mathbf{P}} - e^{-s\tau} \bar{\mathbf{Q}} \right) \Phi(s, \Omega) \right] = 0 \quad (\text{C-28})$$

and for a system with rigid tool/spindle,

$$\Phi = \begin{bmatrix} 0 & 0 & 0 & 0 \\ 0 & 0 & 0 & 0 \\ 0 & 0 & \phi_{xx} & \phi_{xy} \\ 0 & 0 & \phi_{xy} & \phi_{yy} \end{bmatrix} \text{ or } \Phi = \begin{bmatrix} \mathbf{0}_{2 \times 2} & \mathbf{0}_{2 \times 2} \\ \mathbf{0}_{2 \times 2} & \Phi_{ww} \end{bmatrix}, \Phi_{ww} = \begin{bmatrix} \phi_{xx} & \phi_{xy} \\ \phi_{xy} & \phi_{yy} \end{bmatrix} \quad (\text{C-29})$$

Let the elements of the 4x4 matrix of the product of $a \left(\bar{\mathbf{P}} - e^{-s\tau} \bar{\mathbf{Q}} \right)$ be represented as

α, β, \dots :

$$a \left(\bar{\mathbf{P}} - e^{-s\tau} \bar{\mathbf{Q}} \right) = \begin{bmatrix} \alpha & \beta & \chi & \delta \\ \varepsilon & \phi & \gamma & \eta \\ \iota & \varphi & \kappa & \lambda \\ \mu & \nu & \xi & \theta \end{bmatrix} \quad (\text{C-30})$$

The characteristic equation is calculated as:

$$\begin{aligned}
 & \det \left[\mathbf{I}_{4 \times 4} + a \left(\bar{\mathbf{P}} - e^{-s\tau} \bar{\mathbf{Q}} \right) \Phi(s, \Omega) \right] \\
 &= \det \left[\begin{array}{ccc|cc} 1 & & & \alpha & \beta \\ & 1 & & \varepsilon & \phi \\ & & 1 & \iota & \varphi \\ & & & \mu & \nu \\ & & & \kappa & \lambda \\ & & & \xi & \theta \end{array} \right] + \begin{array}{cc|cc} \chi & \delta & 0 & 0 \\ \gamma & \eta & 0 & 0 \\ \phi_{xx} & \phi_{xy} & 0 & 0 \\ \phi_{xy} & \phi_{yy} & 0 & 0 \end{array} \\
 &= \det \left[\begin{array}{ccc|cc} 1 & & & 0 & 0 \\ & 1 & & 0 & 0 \\ & & 1 & \chi\phi_{xx} + \delta\phi_{yx} & \chi\phi_{xy} + \delta\phi_{yy} \\ & & & \gamma\phi_{xx} + \eta\phi_{yx} & \gamma\phi_{xy} + \eta\phi_{yy} \\ & & & \kappa\phi_{xx} + \lambda\phi_{xy} & \kappa\phi_{xy} + \lambda\phi_{yy} \\ & & & \xi\phi_{xx} + \theta\phi_{yx} & \xi\phi_{xy} + \theta\phi_{yy} \end{array} \right] \quad (C-31) \\
 &= \det \left[\begin{array}{cc|cc} 1 & 0 & \kappa & \lambda \\ 0 & 1 & \xi & \theta \end{array} \right] + \begin{array}{cc} \phi_{xx} & \phi_{xy} \\ \phi_{xy} & \phi_{yy} \end{array}
 \end{aligned}$$

Therefore, only the 2x2 sub-matrix on the bottom right of process gain matrices, shown as $\bar{\mathbf{P}}_{ww}$, $\bar{\mathbf{Q}}_{ww}$, affects the stability equation:

$$\bar{\mathbf{P}} = \begin{bmatrix} \bar{\mathbf{P}}_{tt} & \bar{\mathbf{P}}_{tw} \\ \bar{\mathbf{P}}_{wt} & \bar{\mathbf{P}}_{ww} \end{bmatrix}, \bar{\mathbf{Q}} = \begin{bmatrix} \bar{\mathbf{Q}}_{tt} & \bar{\mathbf{Q}}_{tw} \\ \bar{\mathbf{Q}}_{wt} & \bar{\mathbf{Q}}_{ww} \end{bmatrix} \quad (C-32)$$

Referring to (C-19) and (C-20), this leads to a characteristic equation in the form of:

$$\det \left[\mathbf{I}_{2 \times 2} + a \left(\bar{\mathbf{P}}_{ww} - e^{-s\tau} \bar{\mathbf{Q}}_{ww} \right) \Phi_{ww} \right] = 0 \quad (C-33)$$

from equations (C-19) and (C-20)

$$\begin{aligned}
 \bar{\mathbf{P}}_{ww} = \bar{\mathbf{Q}}_{ww} = & \frac{NK_r}{4\pi} \left[\begin{array}{cc} (\phi_{ex} - \phi_{st}) - \frac{\sin 2\phi_{ex} - \sin 2\phi_{st}}{2} & -\frac{\cos 2\phi_{ex} - \cos 2\phi_{st}}{2} \\ -\frac{\cos 2\phi_{ex} - \cos 2\phi_{st}}{2} & (\phi_{ex} - \phi_{st}) + \frac{\sin 2\phi_{ex} - \sin 2\phi_{st}}{2} \end{array} \right] \\
 & + \frac{NK_t}{4\pi} \left[\begin{array}{cc} -\frac{\cos 2\phi_{ex} - \cos 2\phi_{st}}{2} & (\phi_{ex} - \phi_{st}) + \frac{\sin 2\phi_{ex} - \sin 2\phi_{st}}{2} \\ -(\phi_{ex} - \phi_{st}) + \frac{\sin 2\phi_{ex} - \sin 2\phi_{st}}{2} & \frac{\cos 2\phi_{ex} - \cos 2\phi_{st}}{2} \end{array} \right] \quad (C-34)
 \end{aligned}$$

Therefore, the characteristic equation (C-28) becomes:

$$\det \left[\mathbf{I}_{2 \times 2} + a \left(1 - e^{-s\tau} \right) \bar{\mathbf{P}}_{ww} \Phi_{ww} \right] = 0 \quad (\text{C-35})$$

Altintas and Budak [3] derived following characteristic equation for milling:

$$\det \left[\mathbf{I}_{2 \times 2} - \frac{1}{2} K_t a \left(1 - e^{-s\tau} \right) [A_0] \Phi_{ww} \right] = 0 \quad (\text{C-36})$$

where,

$$\begin{aligned} \frac{K_t}{2} A_0 = \frac{K_t}{2} \frac{N}{2\pi} \times \\ \left[\begin{array}{cc} \frac{\cos 2\phi_{ex} - \cos 2\phi_{st}}{2} - K_{rr} \left((\phi_{ex} - \phi_{st}) - \frac{\sin 2\phi_{ex} - \sin 2\phi_{st}}{2} \right) & -\frac{\sin 2\phi_{ex} - \sin 2\phi_{st}}{2} - (\phi_{ex} - \phi_{st}) + K_{rr} (\cos 2\phi_{ex} - \cos 2\phi_{st}) \\ -\frac{\sin 2\phi_{ex} - \sin 2\phi_{st}}{2} + (\phi_{ex} - \phi_{st}) + K_{rr} (\cos 2\phi_{ex} - \cos 2\phi_{st}) & -\frac{\cos 2\phi_{ex} - \cos 2\phi_{st}}{2} - K_{rr} \left((\phi_{ex} - \phi_{st}) + \frac{\sin 2\phi_{ex} - \sin 2\phi_{st}}{2} \right) \end{array} \right] \end{aligned} \quad (\text{C-37})$$

($K_{rr} = K_r / K_t$ is the dimensionless radial cutting coefficient); Therefore,

$$\begin{aligned} \frac{K_t}{2} A_0 = \frac{K_t N}{4\pi} \left[\begin{array}{cc} \frac{\cos 2\phi_{ex} - \cos 2\phi_{st}}{2} & -\frac{\sin 2\phi_{ex} - \sin 2\phi_{st}}{2} - (\phi_{ex} - \phi_{st}) \\ -\frac{\sin 2\phi_{ex} - \sin 2\phi_{st}}{2} + (\phi_{ex} - \phi_{st}) & -\frac{\cos 2\phi_{ex} - \cos 2\phi_{st}}{2} \end{array} \right] \\ + \frac{\overbrace{K_r}^r}{K_t K_{rr} N} \left[\begin{array}{cc} -(\phi_{ex} - \phi_{st}) + \frac{\sin 2\phi_{ex} - \sin 2\phi_{st}}{2} & \frac{\cos 2\phi_{ex} - \cos 2\phi_{st}}{2} \\ \frac{\cos 2\phi_{ex} - \cos 2\phi_{st}}{2} & -(\phi_{ex} - \phi_{st}) - \frac{\sin 2\phi_{ex} - \sin 2\phi_{st}}{2} \end{array} \right] \\ = -\bar{\mathbf{P}}_{ww} \end{aligned} \quad (\text{C-38})$$

In other words, the characteristic equation in [3] could be written as:

$$\begin{aligned} \det \left[\mathbf{I}_{2 \times 2} - a \left(1 - e^{-s\tau} \right) \left(-\bar{\mathbf{P}}_{ww} \right) \Phi_{ww} \right] = \\ \det \left[\mathbf{I}_{2 \times 2} + a \left(1 - e^{-s\tau} \right) \bar{\mathbf{P}}_{ww} \Phi_{ww} \right] = 0 \end{aligned} \quad (\text{C-39})$$

which is the same as the Eq.(C-35).